RADIO WAVE IMAGING USING ULTRA-WIDE BAND SPECTRUM ANTENNAS FOR NEAR-FIELD APPLICATIONS

I. M. DANJUMA

PhD

2020

RADIO WAVE IMAGING USING ULTRA-WIDE BAND SPECTRUM ANTENNAS FOR NEAR-FIELD APPLICATIONS

Design, Development and Measurements of Ultra-Wideband Antenna for Microwave Near-Field Imaging Applications by applying Optimisation Algorithms.

Isah Musa DANJUMA

Submitted for the Degree of
Doctor of Philosophy

Faculty of Engineering and Informatics
University of Bradford

2020

Abstract

Isah Musa Danjuma

Radio wave imaging using Ultra-Wide Band Spectrum Antennas for Near-Field Applications

Design, Development, and Measurements of Ultra-Wideband Antenna for Microwave Near-Field Imaging Applications by applying Optimisation Algorithms.

Keywords

Ultra-Wideband (UWB) Antenna, Microwave Imaging (MSI), Finite Difference Time-Domain (FDTD), Taper Slot Antenna (TSA), Radar Cross Section (RCS), Ground Penetrating Radar (GPR), Synthetic Aperture Radar (SAR), Federal Communication Commission (FCC), International Telecommunications Union Radio Sector (ITU-R), Computational Electromagnetic Technique (CET), Radio Frequency (RF).

The emergence of Ultra-wideband (UWB) technology application has yielded tremendous and vital impacts in the field of microwave wireless communications. These applications include military radar imaging, security screening, and tumour detection, especially for early detection of breast cancer. These indicators have stimulated and inspired many researchers to make the best use of this promising technology.

UWB technology challenges such as antenna design, the problem of imaging reconstruction techniques, challenges of severe signal attenuation and dispersion in high loss material. Others are lengthy computational time demand and large computer memory requirements are prevalent constraints that need to be tackled especially in a large scale and complex computational electromagnetic analysis. In this regard, it is necessary to find out recently developed optimisation techniques that can provide solutions to these problems.

In this thesis, designing, optimisation, development, measurement, and analysis of UWB antennas for near-field microwave imaging applications are considered. This technology emulates the same concept of surface penetrating radar operating in various forms of the UWB spectrum. The initial design of UWB monopole antennas, including T-slots, rectangular slots, and hexagonal slots on a circular radiating patch, was explicitly implemented for medical imaging applications to cover the UWB frequency ranging from 3.1 GHz to 10.6 GHz.

Based on this concept, a new bow-tie and Vivaldi UWB antennas were designed for a through-the-wall imaging application. The new antennas were designed to cover a spectrum on a lower frequency ranging from 1 GHz - 4 GHz to ease the high wall losses that will be encountered when using a higher frequency range and to guarantee deeper penetration of the electromagnetic wave. Finally, both simulated and calculated results of the designed, optimised antennas indicate excellent agreement with improved performance in terms of return loss, gain, radiation pattern, and fidelity over the entire UWB frequency. These breakthroughs provided reduced computational time and computer memory requirement for useful, efficient, reliable, and compact sensors for imaging applications, including security and breast cancer detection, thereby saving more lives.

Dedication

This work is dedicated to my late parents.

Acknowledgement

Table of Contents

List of Acronyms

2D	Two Dimensional
3D	Three Dimensional
ADC	Analogue to Digital Converter
Balun	Balanced / Unbalanced
CST	Computer Simulation Technology
EC	European Commission
EM	Electromagnetic
FCC	Federal Communications Commission
FDTD	Finite Difference Time Domain
FDFD	Finite Difference Frequency Domain
FEM	Finite Element Method
FM	Frequency Modulation
GA	Genetic Algorithm
GPR	Ground Penetrating Radar
IED	Improvised Explosives Device
ITU-R	International Telecommunication Union Radio Sector
LOS	Line of Sight
MSI	Microwave Imaging
NFI	Near-Field Imaging
PSO	Particle Swarm Optimisation
RCS	Radar Cross Section
RF	Radio Frequency
SADEA	Surrogate model Assisted Differential Evolution Algorithm
SAR	Synthetic Aperture Radar
SNR	Signal-to- Noise Ratio
TSA	Tapered Slot Antenna
TWI	Through-Wall Imaging
TSAR	Tissue Sensing Adaptive Radar
UWB	Ultra-Wideband
VNA	Vector Network Analyser
VSWR	Voltage Standing Wave Ratio

List of Figures

List of Tables

Chapter 1

Introduction

1.1   Background

The microwave imaging in the near-field has been attracting much interest in the field of medical, military, and other law enforcement agencies due to its effectiveness, capability, accuracy, and successive improvements in categorising target of interests, in contrast to other similar tools [1]. According to references [2-5], Ultra-wideband (UWB) system are the most appropriate technologies for imaging applications in the near field on the condition that a useful frequency range of the required waveform is achieved. Furthermore, the UWB signals are characterised by the wider bandwidth feature, which guarantees better range resolution when good impedance and suitable radiation patterns are performed over the desired frequency range. The UWB system operates in a very large bandwidth by utilising the signal in short pulse duration.

In Reference [6], the first report and order of the Federal Communications Commissions (FCC) in the United States (US), stated that a UWB signal covers the frequency band from 3.1 GHz -10.6 GHz at a limited transmit power of -41.3 dBm/MHz in the US. In Europe, the European Community (EU) allows the use of only part of the spectrum in the order of 3.1 GHz – 4.8 GHz and 6.0 GHz – 8.5 GHz, respectively [7]. The ability of UWB signals to yields better resolution and short-range capability is associated with the short pulse duration of the transmitted signal. This application to radar technology resulted in bandwidth increment, which would, in turn, enable the radar system to obtain more information from the target signals. Typically, an UWB signals is in one ns pulse duration, which is equivalent to a 30 cm wavelength in free space and a down-range resolution of 15 cm. The

down-range resolution of the radar system is a function of the wavelength of the pulse [8]. In a traditional narrowband radar system, the pulse duration is in one μs, which is equivalent to 300 m of wavelength in free space and the down-range resolution of 150 m. The reduction in pulse duration of the UWB signals leads to an improvement in down-range resolution. When the wavelength of pulse in conventional radar is larger than the size of the target of interest, the returned signal will provide little information about the nature of the target. The combination of the essential features of the UWB signals such as larger bandwidth, low power requirements, ultra-short pulse width, and carrier-less signals makes it a better candidate for the microwave imaging applications and these would improve high data transmission speed, reduction in both multipath and probability of interception and detection and most significantly the precise ranging and localisation.

Systems utilising UWB technology are categorised into three main fields, including:

➢ The vehicular radar system,

➢ Wireless communication system and

➢ Imaging application system.

The imaging application system is further classified into a medical imaging system through-wall radar imaging and ground-penetrating radar imaging. These imaging applications are used in both the military and civilian organisations. Applications such as through- the -wall radar imaging (TWRI) [9-12], detection of a concealed weapon, and explosive [13-15] devices are mostly used by the military. In the civilian sector, applications including assets and resources location [16], indoor robotic navigation [17], and intelligent transport system [18] are used. Both the military and civilian are using medical imaging applications in the health area, such as in the tracking of cardiac and respiratory motions [19, 20] and the early detection and treatment of breast cancer [2, 21-23].

1.2   Aims and Objectives

The thesis aims and objectives are centred on the design, development, and measurements of the UWB antenna for microwave near-field imaging applications by applying optimisation algorithms for improved antenna performance. The design and physical implementation of the various antenna was carried out using these optimisation techniques and compared to a standard method for the imaging applications. The main aims and objectives of this thesis include:

1. Performing a broad study on the existing ultra-wideband antenna for microwave imaging applications for an improve antenna performance.

2. Conducting an investigative study on the optimisation algorithms to obtain the optimal solution at the desired spectrum of interest.

3. Conducting complete design and physical implementation of various UWB antennas using CST microwave studio for microwave imaging applications.

4. Performing an experimental measurement and compared it with simulation result validation.

5. Development of an experimental breast phantom was carried out.

6. Application of an imaging algorithm to the UWB microwave imaging system for further signal processing and analysis.

The major contributions of this work are:

1.   Six new UWB antennas for microwave imaging applications have been proposed, designed, simulated using optimisation algorithms. Four of those antennas are measured for body-centric applications and the other two for through the wall imaging applications. Parametric and numerical studies have been performed to investigate the effects of the human body on four

of the proposed antennas. The necessary guidelines for the designed antennas were also provided.

2. This work has also demonstrated the use of optimisation techniques in reducing the size of the antennas considerably and obtain the required bandwidth. Additionally, the guidelines needed for the optimisation tasks were also highlighted.

3. A compact printed circular monopole antenna (PCMA) with T slots for UWB microwave imaging applications, specifically for breast cancer detection, has been proposed. The profile of the proposed antenna features T-Slots etching over a driven circular patch. The results presented in this study show that the proposed PCMA with T-slot offers high immunity to the human body. The simulated and measured results were in good agreement.

4. Two miniaturise antennas, including bow-tie and Vivaldi antennas, were also studied for microwave through the wall and breast cancer imaging applications, respectively. The operation principles and optimisation techniques used for the miniaturisation have been explained for both designs.

5. Two compact printed monopoles for the UWB spectrum for microwave imaging have been proposed. All the two antennas were designed to cover the whole UWB spectrum, as defined by the FCC of the U.S.A. The simulated and measured results agree for both antennas. Both antennas are used for arrays owing to their compact sizes.

1.3 Organisation of the Thesis

The rest of this thesis is structured as follows:

Chapter 2: The chapter presents an extensive review of antenna for microwave imaging technology and applications. In this chapter, antenna history was highlighted featuring different types, sizes, and types of materials used for their fabrication. Discussion of antenna adjacent to dielectric material was also highlighted with some of the antenna fundamentals and system performance. Additionally, the reviews of ultra-wideband radar for microwave imaging applications, most notably on the status of the existing microwave imaging system in the area of medical, GPR, and through the wall imaging, were considered. Furthermore, the categories of antenna design used for the implementation of the design and the research group responsible for such developments were also highlighted.

Chapter 3: This chapter describes the UWB techniques for the measurement of attenuation and dispersion through mediums. Additionally, computational numerical analysis techniques used for the modelling and interaction of the electromagnetic waves and the homogeneous wall properties are also highlighted. Furthermore, optimisation techniques used in obtaining the optimal solution of the desired spectrum were enumerated.

Chapter 4: This chapter presents and discusses practical designs, development, and measurements of the ultra-wideband antenna, particularly for microwave near-field imaging applications. The initially designed antenna was the bowtie antenna for wall imaging applications. This antenna exhibits high immunity and stable radiation pattern proximity to the wall materials. The second antenna is the coaxial fed rectangular patch antenna designed to resonate at 2.65 GHz for body-centric applications. The third antenna is the printed Vivaldi antenna for breast cancer imaging applications. The antenna exhibits ultra-wideband characteristics, stable

directional radiation pattern, and capability to obtain resonant at a lower frequency. A brief description and design equation are included for each antenna.

Chapter 5: This chapter presents and discusses the monopoles antenna for microwave imaging applications. These antennas exhibit ultra-wide bandwidth, and their ease of design and fabrication from simulation to practical experiments make them more suitable for microwave imaging applications. In this chapter, designed and physical fabrication of various monopoles antenna was carried out, including printed rectangular monopole antenna with T-slot, rectangular slot, and Hexagonal slot monopoles antennas for microwave imaging applications.

Chapter 6: This chapter discusses microwave imaging using arrays of antenna elements. The first analysis was aimed at the design of a compact ultra-wideband hexagonal monopole antenna for microwave imaging applications. In this analysis, different array configurations, including four, six, eight, and twelve antenna arrays were considered. The array has been arranged such that each antenna element is halfway from the adjacent element according to 360/n where n represents the number of the antenna elements. The second array discussion dwells on microwave imaging using arrays of Vivaldi antenna for breast cancer imaging applications.

Chapter 7: This chapter provides the conclusion of this study. It also offers future works and suggestions aimed towards enhancing more research about near-field microwave imaging applications.

Chapter 2

Literature Review

2.1   Introduction

Antennas are devices capable of transmitting or receiving electromagnetic waves [24]. An antenna also acts as a transitional element between the transmission line (guiding device) and the free space [24]. The history of an antenna is related to the electromagnetic theory of waves by James Clerk Maxwell in 1864 [25]. The theories of electricity and magnetism are accurately unified, and their relationship was represented through a set of powerful equations best knowns as the Maxwell equation published in 1873 [26]. In 1886, the first wireless electromagnetic system was established by Heinrich Hertz based on the extension of Maxwell's equations [25]. Guglielmo Marconi used Heinrich Hertz's assumption to send the first transatlantic transmission from Cornwall, England to St. John's, new found land in 1901 [25].

In his experiment, Marconi used a transmitting antenna consisting of 50 vertical wires which were connected to ground through a spark transmitter and supported horizontally by a guyed wire. In contrast, the receiving antenna at St. John's is supported by a kite, and this was the beginning of the antenna era [27]. During Marconi's start-up to the 1940s, antenna system technology was mainly concentrated on wire radiating elements with a spectrum ranging from 300 MHz – 3 GHz. However, during World War II, modern antenna technology was inaugurated, and new elements, including waveguide apertures, horns, and reflectors, emerged. The new era of antennas also witnessed the invention of microwave elements such as klystron and magnetron with a spectrum of 1 GHz and above. An antenna can serve as a transmitter by radiating electromagnetic

wave energy from the source to space known as a transmitter antenna or from the space to the receiver, known as a receiver antenna. Figure 2.1 illustrates an antenna as a transitional element, and Figure 2.2 shows the essential operation of transmitting and receiving antennas.
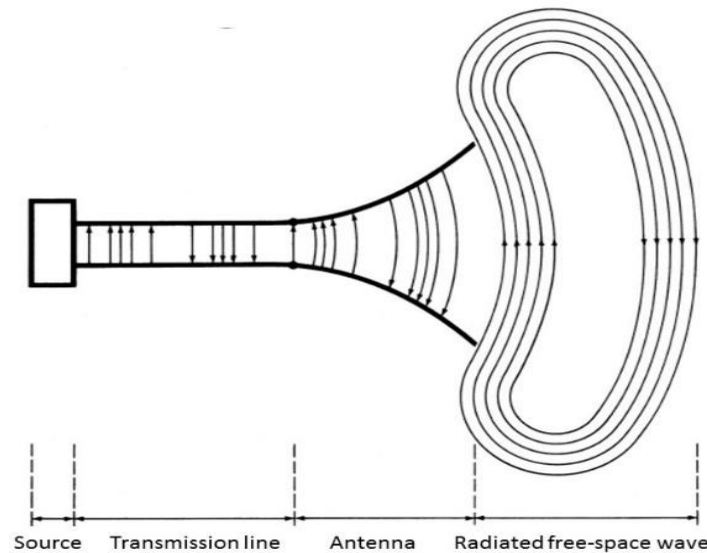
Figure 2.1: Antenna as a transitional element [24].

In the past, most antenna elements were of the wire type, including dipoles, long wires, fans, rhombuses, and helices, which are mostly used as single elements or in arrays. However, during and after World War II, antennas metamorphosed into various shapes and structures such as horns, slots, open-ended wave-guide, reflectors, and lenses used for communication, remote sensing, and deep space and radar applications and generally operate in the microwave region.
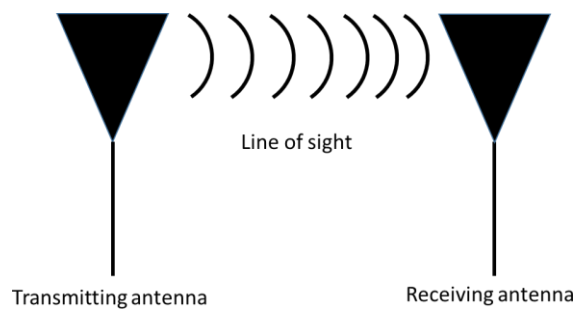
Figure 2.2: Basic operation of transmitting and receiving antennas.

2.2   Antenna Radiation adjacent to a dielectric material

The antenna radiation occurs due to the time-varying current or acceleration and deceleration of charges within the antenna element. If there is no movement of charges within such an element, no radiation will take place since there is no flow of currents. Radiation will also not occur if the charges are moving with uniform velocity along a straight conductor. However, radiation will arise if the charges are moving with equal velocity along a curved wire or antenna. Furthermore, if the charge is oscillating with time, then the radiation will also occur even along a straight wire.

The application of a sinusoidal input voltage V_{in} across a transmission line resulted in the creation of an electric field, which is also sinusoidal, and these lead to the formation of an electric line of forces. The free electrons attached to the transmission lines are now displaced by the electric line of forces, which caused the movement of charges resulting from the flow of currents, which in turn leads to the creation of a magnetic field.

Due to the time-varying magnetic field and electric fields, electromagnetic waves (EM) are created, and these waves travel through the transmission lines into the antenna. As these waves travel from the transmission lines to the antenna, an incident power P_{in} is transmitted into the antenna, where some of the power P_r is reflected at the terminal accompanied with terminal losses, also known as a reflection because of mismatch between the transmission lines and the antenna and others are transmitted into the antenna structure. Inside the antenna structure, some of this power gives out some losses termed as conduction and dielectric losses. The amount of losses at the terminals of the antenna and within the structure defines the antenna efficiency parameter. As the waves approach

free spaces into the lossy materials, some of these waves are radiated into the free spaces while others are radiated into the lossy material, as indicated in Figure 2.3.
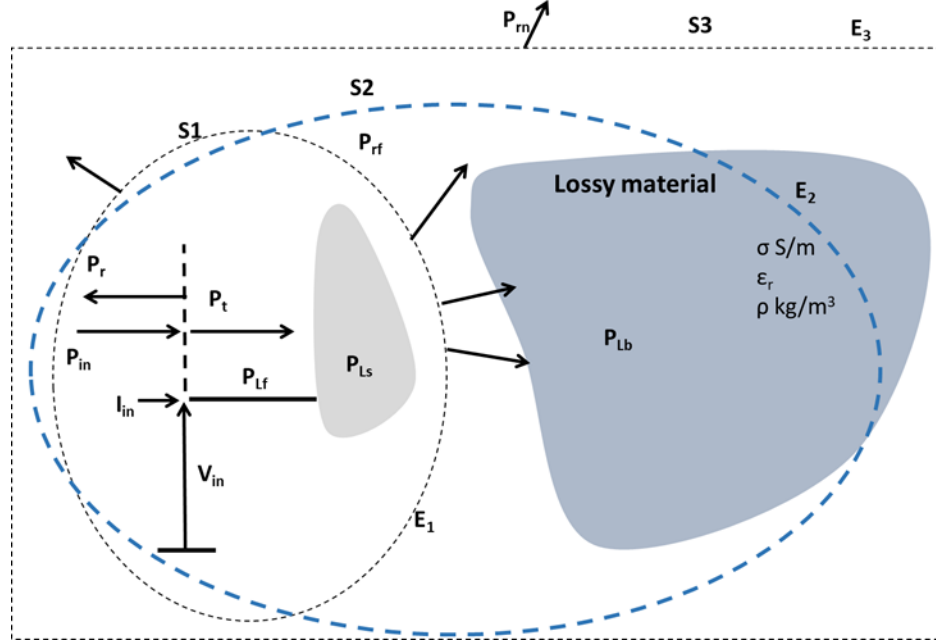
Figure 2.3: Antenna adjacent to a dielectric material.

The passing of EM waves through the lossy material medium is subject to amplitude and phase distortion. These distortions are due to the attenuative and dispersive materials of the propagating medium. The Lossy materials propagating medium are more challenging when interacting with the EM waves, because of their high transmission loss leading to reflection and absorption. These problems become more severe in an imaging application where the transmit or receive antennas are collocated on the same side of the lossy material. The electrical properties of the lossy material medium are characterised by permittivity ε_r conductivity σ and density p, as indicated in Figure 2.3. The propagation characteristics of the EM waves travelling through the medium are primarily determined by the type of the electrical properties comprising the medium.

2.3   Fundamentals of Antenna

Antennas exist in various shapes and sizes to satisfy different types of applications. Wide ranges of antennas have been developed in the past for different applications. Antennas such as dipole, monopole, helix, yagi-uda, and loop are a typical example of wire antennas, as shown in Figure 2.4. Wire antennas are characterised to have lightweight, low cost, and accessible design implementation. However, the small gain is one of their set back [24].

Aperture antennas are other examples of antennas with high gains and mostly used for microwave and millimetre-wave applications. Examples of aperture antennas are rectangular or circular horn antennas, lenses, reflector, and open-ended wave-guide antennas. Figure 2.5 shows the different types of Aperture antenna.

(a) Dipole   (b) Circular (square) loop
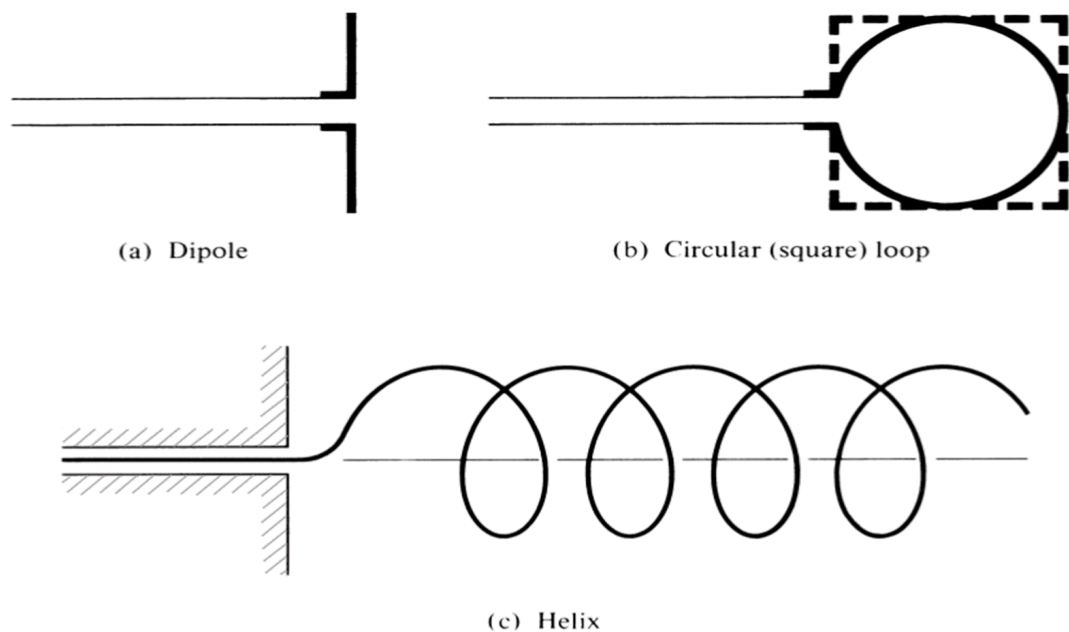
(c) Helix

Figure 2.4: Examples of wire antennas (a) dipole, (b) loop and (c) helix [24].

(a) Pyramidal horn

(b) Conical horn

(c) Rectangular waveguide
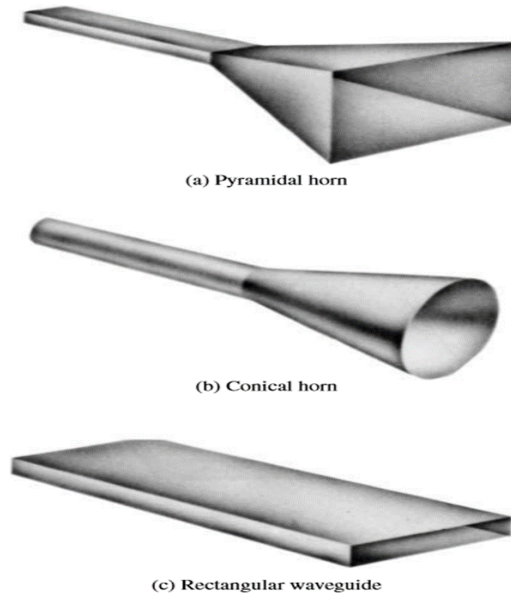
Figure 2.5: Examples of Aperture antennas (a) pyramidal, (b) conical, and (c) rectangular aperture antennas [24].

A Patch antenna exists in different shapes, including triangular, circular, elliptical, and rectangular shape microstrip patch antenna, as indicated in Figure 2.6. Patch antennas perform well when configured with a thick dielectric substrate having low dielectric constants. Patch antennas have advantages, including lightweight, low cost of fabrication, planar configuration, and their capability to operate in the various spectrum. However, these types of antennas have disadvantages such as surface wave excitation, narrow bandwidth, and low gain.
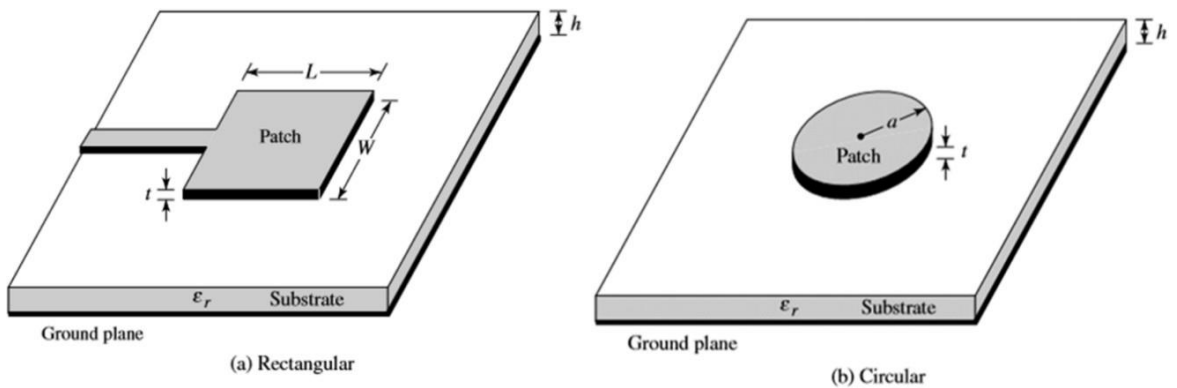
Figure 2.6: Rectangular and Circular Microstrip Patch antennas [24].

Printed antennas are classes of antennas that are mostly used at microwave and millimetre-wave frequency with high gains. Examples of these antennas are printed slots and printed dipoles antennas. There are different types of antennas, which have not been discussed that have various forms and shapes to achieve the desired characteristics for the application, including wireless and microwave applications that will be analysed in subsequent chapters.

2.4 Near and Far-Field Antenna Propagation

The antenna propagation field pattern is dependent on the distance varied from the antenna, as illustrated in Figure 2.7, and these field patterns are related to two types of energy, namely, radiating and reactive energy. Therefore, the radiation area of an antenna is classified into three regions, including reactive near-field, radiating near-field, and far-field region.

2.4.1 Reactive near-field region

The reactive near-field region is the area immediately within the antenna vicinity. None of the energy is dissipated in this region as energy are only stored. The distance from the antenna in this region is determined by:

$$R_1 = 0.62 \sqrt{D^3 / \lambda} \tag{2.1}$$

Where the distance from the antenna origin is R_1, D is the largest dimension of the antenna length, and the wavelength is λ.

2.4.2 Radiating near-field region

Radiating near-field region is the region also referred to Fresnel region and lies between the reactive near-field and the far-field region of the antenna. In this region, the reactive field is insignificant when compared to those in the reactive

near-field and as such radiating field lead in this region. The angular field distribution is dependent on the distance from the antenna in this region and represented by:

$$R_2 = 2\,D^2/\lambda$$

(2.2)

Where R_2 represents the distance from the antenna surface.

2.4.3 Far-field region

The far-field region is the region, also known as the Fraunhofer region, which goes beyond $R_2 = 2\,D^2/\square$. In this region, there are no reactive fields as only radiating fields exist, and angular field distribution is independent of the distance from the antenna.
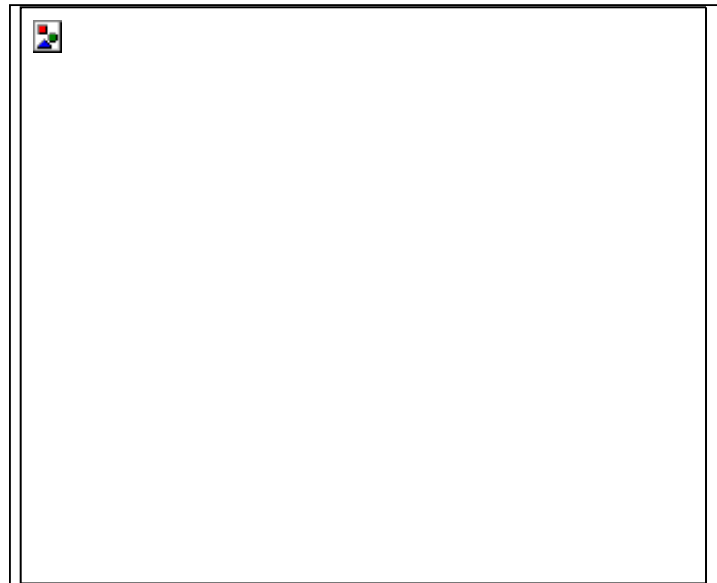
Figure 2.7: Antenna propagation Field regions [24].

2.5 Antenna System Performance Parameters

Antenna parameters referred to those mechanisms needed in the description of the antenna performance to function effectively and efficiently. It is, therefore,

essential to know the basic elements of an antenna system to design them to meet specific application requirements and configurations. The performance related to the antenna are measured from the following parameters:

2.5.1 Radiation Pattern

Antenna radiation pattern is a parameter, which takes into account the antenna far-field radiation properties plot as a function of space coordinates, which are dependent on both elevation θ angle and azimuthal angle ϕ. These plots are represented graphically or mathematically. Antenna radiation pattern is classified into three types: isotropic, Omni-directional, and directional radiation patterns.

➤ Isotropic Pattern: A pattern is said to be isotopic if the radiation pattern is the same in all directions. An antenna with an isotropic radiation pattern radiates power equally in all directions. This type of antenna is not possible to implement in real-time, and as such, the antenna is only used for comparative analysis with real antennas. Considering the total power radiated by the isotropic antenna is P, and this power is spread over a sphere of radius r, then the power density will be:

$$S = \frac{P}{area} = \frac{P}{4\pi r^2} \tag{2.3}$$

Moreover, the radiation intensity for this antenna will be:

$$U_i = r^2 S = \frac{P}{4\pi} \tag{2.4}$$

➤ Omni-directional Pattern: A pattern is said to be Omni-directional if the radiation pattern is isotropic along a single plane. An antenna with an Omni-directional radiation pattern radiates the same power along a particular plane. Typical examples of these types of antennas are the monopole or dipole antennas. These types of antennas are generally characterised with

low gains [24]. Omni-directional antennas often used as radio communications antennas and in mobile devices that use radio signals, including walkies –talkies, FM radios, mobile phones, wireless computer networks, PS, and base stations that communicate with mobile communications.

➢ Directional Pattern: A pattern is said to directional if the radiation pattern is not symmetry along the planes. An antenna with a directional radiation pattern radiates more power in some direction and less power in the other direction. These antennas are mostly used for long-range communications. Effective transmission and reception of this type of antenna are highly achieved by aligning the direction of the transmitter and receiver towards each other. Parabolic dish antennas are typical examples of this type of antenna. The parabolic antenna shape controls the reflected signals towards the receiver. As a directional antenna, the parabolic antenna needs to be pointed towards the direction of the satellite. These antennas are typically used to receive satellite television [24].

Lobes are easily used to illustrate the radiation pattern of a general directional antenna. These lobes are classified as main, minor, and side lobes. The lobe, with the direction of concentrated radiation, is known as the main lobe. Other lobes apart from the main lobes are referred to as minor lobes. The angle difference within the main lobe is known as the half-power beamwidth, also known as 3 dB points. The minor lobes can be further classified into side lobes and back lobe. The back lobe is the minor lobe opposite to the main lobe, while side lobes are minor lobes adjacent to the main lobes, which are separated by nulls, as shown in Figure 2.8.
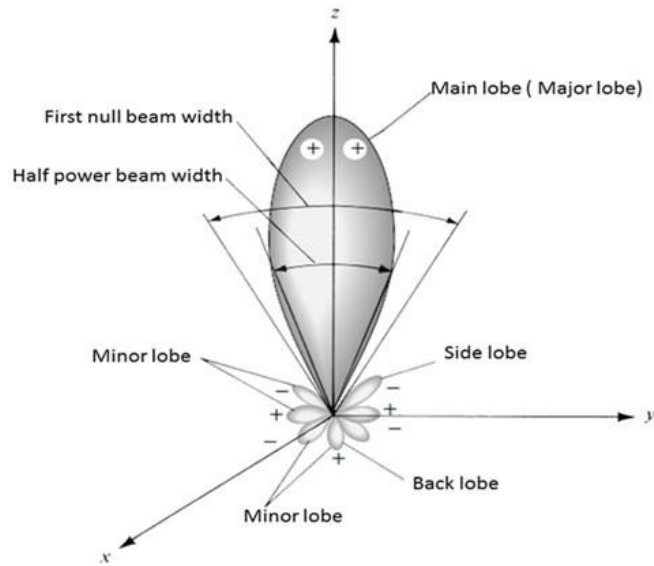
Figure 2.8: Directional antenna radiation pattern [24].

2.5.2 *Directivity*

Directivity is defined as the parameter of an antenna, which indicates an antenna's radiation pattern direction. Mathematically illustrated as the ratio of radiation intensity in a specific direction from the antenna, to the average radiation intensity over all directions. Similarly, the directivity of a non-isotropic antenna is the same as the ratio of its radiation intensity in a particular direction over that of an isotropic antenna, as expressed in the following equation:

$$D = \frac{U}{U_i} = \frac{4\pi U}{P_{rad}} \qquad (2.5)$$

Where, U is the radiation intensity, U_i represents radiation intensity for an isotropic antenna and P_{rad} is the total radiated power. However, if the direction is not given, therefore, the direction of maximum radiation intensity is assumed, and the maximum directivity will be:

$$D_{max} = \frac{U_{max}}{U_i} = \frac{4\pi U_{max}}{P_{rad}} \qquad (2.6)$$

2.5.3 Radiation Power Density

Radiation power density is a parameter that measures the power radiated by an antenna in a particular direction. The relationship between power density and field intensities is shown in (2.7) [24].

$$P_r(r, \theta, \phi) = \frac{1}{2} |E \times H| = \frac{1}{2\eta} |E(r, \theta, \phi)|^2 \tag{2.7}$$

Where E represents the electric field intensity, H refers to the magnetic field intensity, and η is the intrinsic impedance of the transmission medium.

2.5.4 Radiation Intensity

The radiation intensity is a far-field parameter of an antenna, which describes the power radiated from such an antenna per unit solid angle average. The radiation intensity is mathematically derived by multiplying the radiation density by the square of the distance, as indicated in equation 2.8.

$$U = r^2 P_r \tag{2.8}$$

In the above equation, r is the distance to the antenna, while Prad, is the total power radiated by an antenna usually obtained by integrating the radiation intensity over the entire solid angle of 4π, as given in the equation below:

$$P_{rad} = \oint_\Omega U d\Omega = \int_0^{2\pi}\int_0^\pi U \sin\theta \, d\theta \, d\phi \tag{2.9}$$

Where $d\Omega$ represents the solid angle.

2.5.5 Gain

Antenna gain is a parameter that is closely related to directivity, which accounts for both antenna directional ability and efficiency. Therefore, antenna gain is equal to its directivity if the antenna is 100% efficient; as such, the antenna will be considered as an isotropic radiator. Mathematically, antenna gain is the ratio of radiation intensity in a particular direction, to the radiation intensity that would be derived from an isotropic radiator if the power accepted by the antenna were isotropic as described in equation 2.10 [24].

$$Gain = 4\pi \frac{Radiation\ Intensity}{Total\ Input\ Power} = 4\pi \frac{U_{(\theta,\phi)}}{P_{in}}$$

(2.10)

The antenna gain relationship with efficiency and directivity is given by equation 2.11 below:

$$G_{(\theta,\phi)} = e_{cd}D_{(\theta,\phi)}$$

(2.11)

where e_{cd} is the antenna radiation efficiency

2.5.6 Efficiency

The antenna efficiency is a parameter, which measures the number of losses present both at the terminals and within the structure of the antenna elements. These losses are commonly caused by two factors given by [25] as:

- Reflections losses caused by the mismatch between the antenna and the transmitter.

- Conduction and dielectric losses (I^2R) are within the antenna structure [24]. Figure 2.9 indicates the antenna terminals and structural losses.
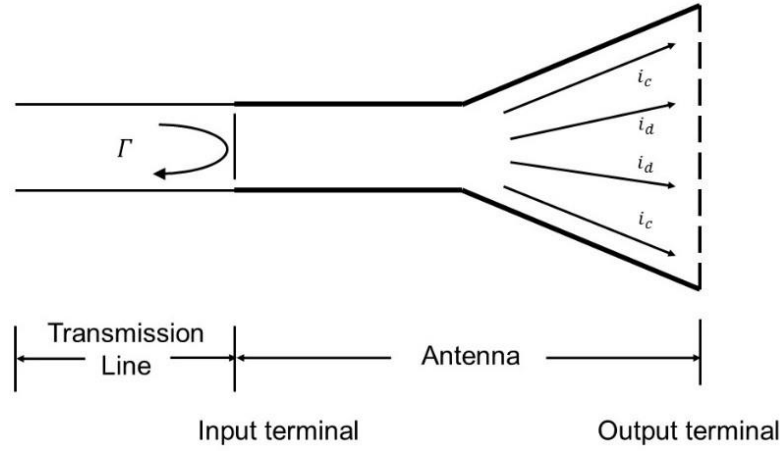
Figure 2.9: Antenna terminals and structural losses [25].

The combination of these losses is termed as total antenna efficiency e_t, which is calculated by using equation 2.12:

$$e_t = e_r e_c e_d \tag{2.12}$$

Where e_r is the mismatch or reflection efficiency given by [25] as:

$e_r = (1 - |\Gamma|^2)$, Γ stands for the voltage reflection coefficient at the antenna input terminals.

Conduction efficiency is represented by e_c, while e_d describes the dielectric efficiency. These two parameters are difficult to be separated and are lumped together to form the antenna radiation efficiency given by [25] as:

$$e_{cd} = e_c e_d = \frac{R_r}{R_r + R_L} \tag{2.13}$$

From equation 2.13, the antenna radiation efficiency e_{cd} is defined as the ratio of the delivered power to the radiation resistance R_r, to the delivered power to both the radiation resistance and loss resistance R_L.

2.5.7 *Polarisation*

The polarisation of an antenna is a parameter that describes the orientation of the electric field vector of the electromagnetic wave as a function of its time-varying direction and relative magnitude to the earth's surface. The most common examples of polarisations include linear, circular, or elliptical. The electric field vector is fixed front and back along a line in the linear polarised wave. In circular polarisation, the electric field vector revolves along a circular path with constant length. Circular polarised wave rotates either clockwise, also known as Right-hand circular polarised (RHCP), or turns in the counter-clockwise direction known as Left Hand Circular Polarised (LHCP). When the electric field vector points represent an ellipse, the polarisation is described as elliptically polarised. Both circular and linear polarised antenna are exceptional cases of the elliptically polarised wave, and they are achieved when the ellipse becomes a circle or a straight line [25].

2.6 Ultra-wideband Antenna Radar Systems Applications

The term ultra-wide, band (UWB) antennas are sensors designed for the transmission and reception of UWB signals. This technology uses short pulses duration to transmit high-bandwidth information covering the frequency band from 3.1GHz to 10.6 GHz. These are achieved with a low power level of - 41.3 dBm/MHz as contained in the First Report and Order of February 2002 by the Federal Communications Commission (FCC), and these lead to the following UWB signals terminology [28].

2.6.1 UWB System Definition

UWB system definition is solely dependent on the radar concept terminology.

- UWB signals are signals with large absolute bandwidth (*BW*) equal or larger than 500 MHz or fractional bandwidth (BW$_r$) equal or greater than 20% of the used centre frequency (f_c).

- Bandwidth (*BW*) is the range of frequency on each side of the centre frequency constrained by -10 dB Power Point as illustrated in Figure 2.10, where f_H and f_L are higher and lower frequencies, respectively, as indicated in equation 2.14.

$$BW = f_H - f_L.$$
(2.14)
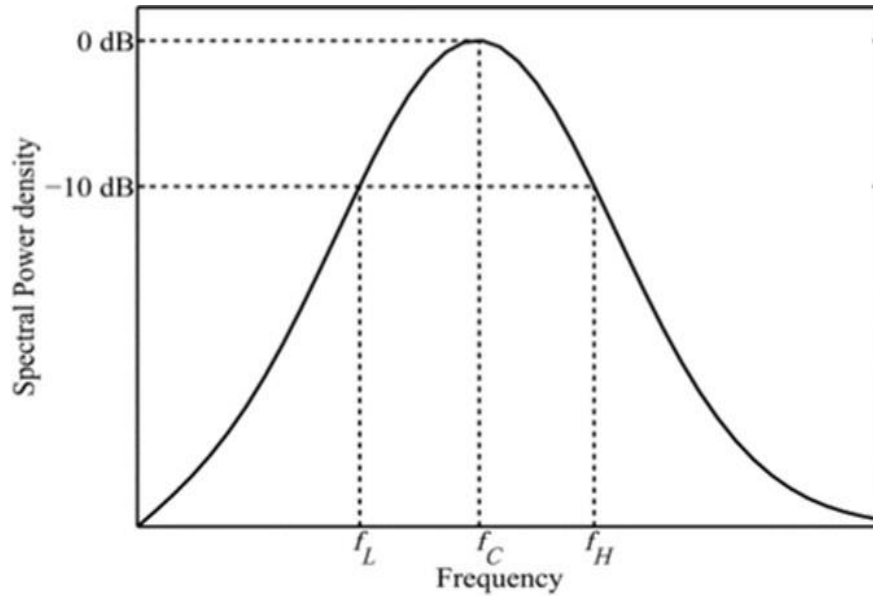
Figure 2.10: Spectral Power Density in dB versus Frequency in Hz [29].

- Centre frequency (f_c) is the average of higher and lower frequency, respectively, as shown in equation 2.15.

$$f_c = \frac{1}{2}(f_H + f_L). \tag{2.15}$$

- Fractional Bandwidth (B_f) of an antenna is defined as a measure of how wide-band the antenna is and usually quoted as a percentage. Therefore, the higher the percentage, the wider the bandwidth.

$$B_f = \frac{BW}{f_c} = \frac{f_H - f_L}{\frac{1}{2}(f_H + f_L)} = \frac{2(f_H - f_L)}{(f_H + f_L)} \times 100\% \tag{2.16}$$

- Resolution refers to the ability of a radar system to distinguish between a stationary or moving target in the same vicinity to each other as different objects [30].

- Downrange resolution ΔR refers to the ability of a radar system to detect and distinguish targets along the vertical direction. Downrange resolution is directly proportional to the speed wave v (m/s) and inversely proportional to the bandwidth wave B (Hz), as illustrated in equation 2.17. Thus, an increase in bandwidth will equal a decrease in a down-range resolution, which is usually expressed in meters (m) [30].

$$\Delta R = \frac{v}{2B} \tag{2.17}$$

- Cross range resolution ΔCR refers to the ability of a radar system to detect and distinguish a target along the horizontal direction. Cross range resolution is related to the antenna beamwidth and usually determined by the antenna effective aperture size, as indicated in equation 2.18 [30].

$$\Delta CR = \theta R \tag{2.18}$$

Mathematically, Cross range resolution is the product of wavelength and range divided by the antenna effective aperture size as given by equation 2.19 [30].

$$\Delta CR = \frac{\lambda R}{2 DSAR} \tag{2.19}$$

- Radar sensitivity refers to the measure of the radar's ability to detect the presence or absence of a target [30].

- Dynamic Range refers to the ratio of the strongest signal to the weakest signal that the radar can handle simultaneously, usually expressed in decibel [30].

- Radar Cross Section refers to the ability of the radar system to intercepts the signal reflected from the targets of interest towards the radar's direction [31].

- Effective Aperture is the measure of how efficiently the physical antenna area is being utilised [31].

2.6.2 *UWB Radar Systems Classifications*

UWB radar system generates and transmits signals of a short pulse duration of nanoseconds through the transmitting antenna to the target of interest. These signal travel in a free-space with a speed of light to meet the target of interest. At the target surface, the signals will be scattered in all directions, some of which would be reflected towards the receiving antenna. By considering the speed of light, the signal travels through the medium; the UWB radar system would use round trip propagation time to calculate the distance or range of the reflected target or imaging object.

Based on this range, UWB radar can be classified into two classes, namely; short and long-range radar systems. The latter is mostly used for surveillance purposes, such as over-the-horizon radar and synthetic aperture radar. Conversely, short-range radar is mostly used for commercial and industrial applications which are due to the capability of detection in the range of centimetres or meters, and at relatively high resolutions, as well as affordable testing and assembly cost [32]. The classification of UWB radar systems is indicated in Figure 2.11.
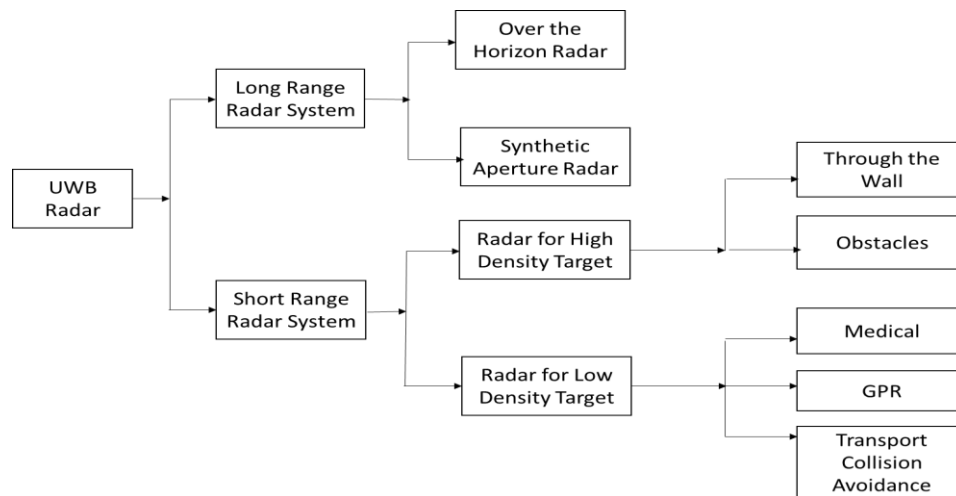
Figure 2.11: Classification of radar system [32].

2.7   Features of Ultra-wideband Signal

UWB signals are associated with three main features, including larger bandwidths, ultra-short pulse width, and carrier less signal. Various advantages and disadvantages of UWB signals arises from these three main features:

2.7.1   Larger Bandwidth

UWB signal, as defined by FCC, is known as any radio signal having a substantial bandwidth. These main features enable the UWB signal to have the advantage of high imaging resolution and high data rate transmission.

    a.   The higher bandwidth of a UWB radar contributed immensely to the high imaging resolution of the UWB radar system [33]. UWB imaging system

is designed to detect and see the object of interest in a structure that can be classified as through-the-wall imaging, wall imaging, biomedical imaging and ground-penetrating radar, The UWB frequency range of 3.1GHz to 10.6 GHz enables the system to have high imaging resolution and deep penetration capability.

b. High data rate transmission can be easily achieved with UWB signals with lower centre frequency. Therefore, the UWB signal has the capability of higher penetration of obstacles such as the wall, which is suitable for military applications of through-the-wall imaging and weapon detection. Conversely, the narrow-band signal required the use of higher carrier frequency to carry out wider bandwidth, and this resulted in the experience of higher propagation losses of the signal [33].

2.7.2 *Ultra-short Pulse Width*

Higher range measurement accuracy and range resolution are possible with UWB signals due to the transmission of ultra-short pulsed waveforms. UWB signals can transmit a low power radio signals in ultra-short pulses in the range of picoseconds or even nanoseconds range across all frequencies ranges. This feature allows UWB signals to be used for precise localisation and has a strong immunity to interference.

a. Precise Localization and accuracy of a target are well achieved by UWB signals, which offer an improved resolution of the signal. Studies have shown that high range measurement accuracy can be achieved with the transmission of Ultra-short pulses waveform. Considering the transmission of the ultra-short pulses of the pulsed waveform of UWB signals, high precise localisation can be obtained. This feature is used

for the indoor environment reconstruction based on the introduction of UWB localisation [34].

b. Interference components of UWB signals can be resolved directly with the transmission of ultra-short pulses. Interference occurs when wireless communication system experience echoes at specific frequencies from secondary signals that bounce back from obstacles after the original signal are received [34]. Due to the transmission of short pulses by UWB signals, pulses belonging to different multipath reflections tend not to overlap in time. Consequently, these pulses tend not to interfere with each other as compared to continuous wave signals whose multipath components always overlap and resulted in substantial interference.

2.7.3 *Carrier-less Signal*

UWB signals are also referred to as carrier-free technology because it can directly modulate the desired signal that spans several GHz of bandwidth without the use of any carrier RF to move the signal. In UWB signals, data is transmitted in the form of digital pulses of EM energy. On the contrary, the conventional narrow and wideband system uses RF carrier to send the signal in the frequency-domain from baseband to the actual carrier frequency. This feature enables UWB signals to have simple hardware configuration and low power operation.

      a. UWB system requires simple hardware to transmit signals in the form of digital pulses with minimal RF or microwave electronics. In contrast, traditional carrier-based technology modulates and demodulate complex analogue waveforms to carry out the transmission of signals, which usually requires very complex hardware configuration [35].

Low power operation of UWB devices consumes less power that is due to the transmission of short pulses regularly as compared to the transmission of modulated waveform continuously in the conventional narrow-band methods. Additionally, UWB devices do not require the conversion of RF to IF, local oscillators, mixers, and other filters for transmission; hence, this lead to low power consumption [35].

2.8 Advantages and Disadvantages of UWB signals

From a radar perspective, short-pulse UWB techniques exhibit at least seven distinct advantages over more conventional radar approaches. These advantages include [36]:

a. Higher range measurement accuracy and range resolution due to the transmission of short-pulsed waveforms.

b. Enhanced target recognition due to the detection of additional information from a target's separate elements.

c. It has a strong immunity to passive interference such as rain, fog, clutter, aerosols.

d. Increased immunity to co-located radar transmissions due to decreased pulse-on-pulse probabilities.

e. Increased detection probability for certain classes of targets due to the elimination of the lobbying structure of the targets' secondary patterns, i.e., there is no interference between signals scattered by a separate target element.

f. Increased radar operational security because of the vast spectral spreading.

g. Ability to detect very slow-moving or stationary targets.

UWB radar systems are faced with challenges, including antenna design, the problem of imaging reconstruction techniques to cope with complicated scenarios, and the problem of severe signal attenuation in high loss materials [36].

a. Antenna design constitutes one of the most significant challenges in the design of a UWB radar system. New challenges of the UWB antenna design includes radiation instability and the problem of impedance matching, the compact appearance of the antenna size and low manufacturing cost for consumer electronic applications [36]. For

efficient radiation of a UWB signal, the behaviour and performance of the UWB antenna should be consistent. Inconsistency in these types of performance and practice resulted in the antenna characteristics of the linear phase, low return loss, constant directivity, and group delay [36].

b. The challenge of imaging reconstruction techniques in the detection of the complicated medium to deal with complicated scenarios is one of the most significant challenges. Also, the down-range and cross-range resolution of a UWB imaging system can significantly influence the adopted image reconstruction algorithm. Therefore, appropriate beam-forming methods are very vital for achieving higher imaging resolution. When a severe multipath effect exists, a traditional imaging method finds it challenging to differentiate multiple targets [37].

UWB pulse radar suffers from high signal attenuation in high loss materials such as walls made of concrete with high water content or wet soil, human tissue, and other high water-content materials, and these poised a significant challenge to the system [38]. Conversely, UWB pulse radars operating at higher UWB perform efficiently and effectively with line-of-sight or "see-through "low-loss materials detection, such as wood and glass. However, When the UWB radar system interacts with opaque medium, they suffer reflection and absorption.

2.9 Overview of UWB Microwave Imaging

Microwave imaging has gained tremendous attention ranging from military to civilian applications due to its fast illumination capability response of electromagnetic wave propagation. This wide range of applications is due to its versatility and suitability, which are used in the military for through-the-wall imaging [9, 39, 40], detecting weapon and IED [41, 42]. The use of Ground-penetrating radar (GPR) is another application of microwave imaging used for the investigation

of any concealed weapons such as metals and land mines buried beneath the earth's surface [43-45]. In [46], underground pipelines defects are also detected with the use of GPR. In biological and medical applications, microwave imaging has been the focus of significant research such as in breast cancer [2, 4, 47], heart diseases [19, 20, 48], brain [49, 50] imaging where microwave frequency is applied to radiate the tissue content of the human body.

UWB signals have the capability of penetrating through a great variety of opaque materials, such as biological tissues including breast, brain, bones, other mediums such as clothes, bags, ground and through different types of walls such as concrete, porcelain, wood, paper, glass, nylon, and Plexiglas. The main aim is to be able to detect, identify, classify, and track the whereabouts of humans, moving or stationary objects. These attributes are highly desirable for a range of organisations, including military, police, first responders, and fire and rescue personnel. Hence the need to examine the status of these promising technologies.

2.9.1 Current Status of Medical Imaging

Medical Imaging is a method for exploring and creating images of interior structures or human body tissue for medical investigation. This process reveals internal structures configuration not visible to our naked eyes for analysis and treatment. Ultrasound devices, X-ray scanning technology using computed tomography (CT), and radiology system using Magnetic Resonance Imaging (MRI) serve as current medical imaging technology in place [51]. In all the health-related imaging submissions, breast imaging is attracting more interest because of breast cancer that serves as a common disease affecting women worldwide, triggering

many deaths yearly. Breast cancer microwave imaging is categorised into three groups, including passive, hybrid, and active.

In the passive method, the method classifies and differentiate the healthy tissue from the malignant ones by the use of microwave radiometry to increase the temperature [23]. The measured temperature is used in mapping the complete image of the breast examined for additional analysis. The hybrid approach, on the other hand, involves the use of microwave and ultrasonic systems to find the existence and location of the tumour. Increased in tumours' conductivity as compared to the healthy tissue, will lead to further absorption of microwave energy by the tumour, and ultrasonic transducers heat these. The resultant effect will lead to the creation and detection of pressure, which would, in turn, change into the image of the tumour [23]. In an active method of microwave imaging of breast cancer, a complete imaging structure is constructed by monitoring and reformation of the reflected signal. The dissimilarity in the permittivity and conductivity of the regular and irregular tissue would be significantly detected. As such, the active method of microwave breast cancer imaging is the most widely accepted [23].

The tomography and radar-based approaches are the primary types of active methods. In the radar-based approach, a short-pulsed signal is transmitted into the target of interest from a single UWB antenna in a monostatic mode to generate a backscatter signal for further signal analysis. This process would be repeated at different locations around the breast. When there is the presence of a tumour, more energy would be reflected, and this would affect the response time for the tumour location to be predicted. The travel time for the signal would be recorded and computed at various locations. As such, the images, indicating the presence and

location of the highly scattered target of interest, would be created [52-54]. The use of an image reformation algorithm is not needed in this method.

Alternatively, the tomography method uses the bistatic model to send the signals into the tissues while incorporating several antennas to be placed around the breast tissue to obtain the reflected target of interest. In these methods, the maps of the electrical properties are formed [55-58]. A quite number of researchers has investigated UWB imaging for breast cancer with some prominent ones reviewed as follows:

The first clinical prototype on an active near-field microwave imaging of breast cancer was reported in [59] at Dartmouth College. Antenna arrays comprise of 16 monopoles antennas were arranged in a circular configuration of a spectrum ranging from 0.3 GHz-1 GHz as indicated in Figure 2.12. The examination was carried out, whereby the woman to be scanned had to lie with her stomach making her breast stretched upward to the tank containing a mixture of glycerine and saline. The woman's nipples to be scanned has to be aligned towards the chest wall of Figure 2.13. The first study was conducted on 23 women with the aid of a water-coupled interface surrounding the pendant breast of the women to be examined. No abnormalities were reported on mammograms, and the examination revealed a straightforward method of microwave imaging.

In the second investigation, 150 women were studied, including women of normal and abnormal mammograms. The target of interest in one of the breasts is defined with the available information derived from other imaging modalities and compared to that of the target of interest. In the imaging scenario, the transmitting sensor

radiates the signals into the breast tissue, and the backscattered signals were received from the receiving antennas. The signal conversion was realized by changing the transmitted signal with a reference signal to generate a short-frequency response usually sampled by an Analog to Digital converter to produce amplitudes and phase of the extracted signal [60].
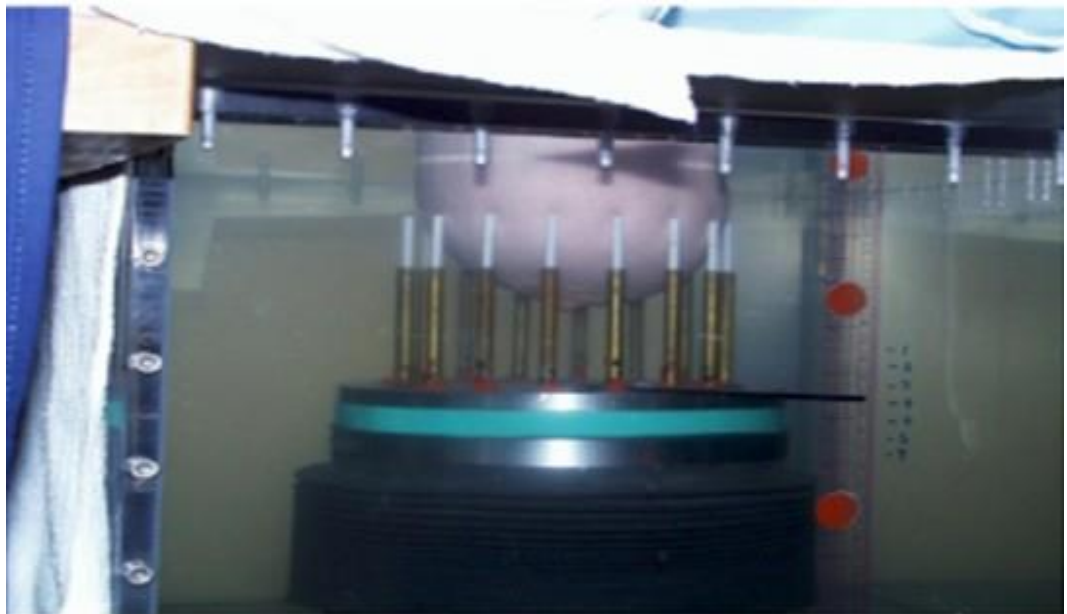
Figure 2.12: An illumination tank with the antenna arrays [59].

Figure 2.13: Dartmouth College electronic circuit's components of the breast imaging system [59].

Another investigation was conducted and reported at the University of Bristol, Bristol, UK. In this analysis, a prototype of a human testing imaging system for radar-based breast configuration was carried out. The setup comprises 31 (prototype 1) [53] and (prototype 2) [61] antennas, which are distributed over a hemispherical surface. The imaging technique involves the use of the examination table on which the woman to be scanned would lie down on her stomach, paving the way for her breast to enter the hole of the table. The breast would be in contact with the hemispherical array, and measurement would be carried out by exciting the antenna to radiate the signals into the breast for the reflected signals to be received by the receiving antennas. The operating frequency covers a spectrum of 4GHz-8 GHz [61]. The scanning process was carried out in only 10s duration using delay and sum beamforming to create the images by concentrating the reflections in the target of interest. Some of the challenges encountered from the experimental studies comprise the imaging of the breast tissue composition and the ability to

make consistent contact between the patient and the sensor. The laboratory set up of the imaging system is indicated in Figure 2.14.
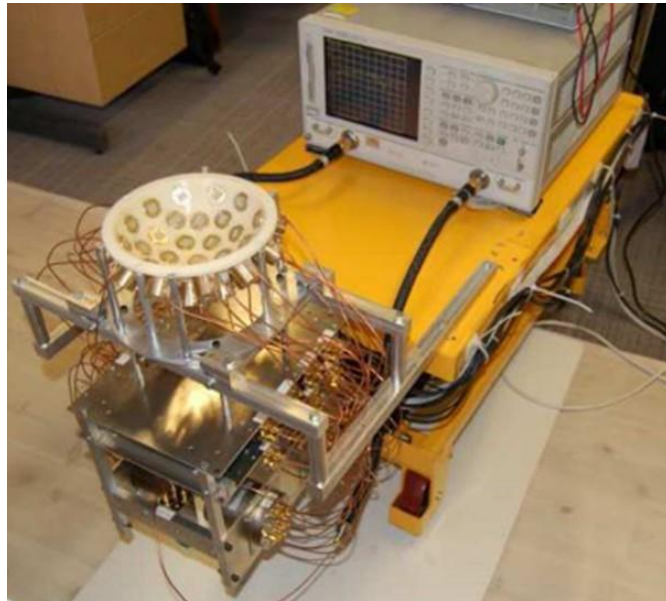
Figure 2.14: The imaging system laboratory set up [53].

The mono-static radar-based configuration was presented at the University of Wisconsin [62, 63] comprising a pyramidal horn antenna with UWB characteristics, as indicated in Figure 2.15 (a). In this configuration, the system makes use of the antenna array to scan the single horn antenna to the respective position of the antenna arrangement placed around the breast phantom. Signals are radiated through the transmitting antennas to the breast, and the reflected signals were established through the receiving antennas. An Agilent E8364A network analyser was used to develop and characterise the received signal. All time-domain measured waveforms were generated using the network analyser, as indicated in Figure 2.15 (b) and (c), respectively. The Spectrum of 1 GHz to 11 GHz is used to cover the measurement of 201 frequency samples based on Finite Difference Time Domain.

(a)   (b)   (c)
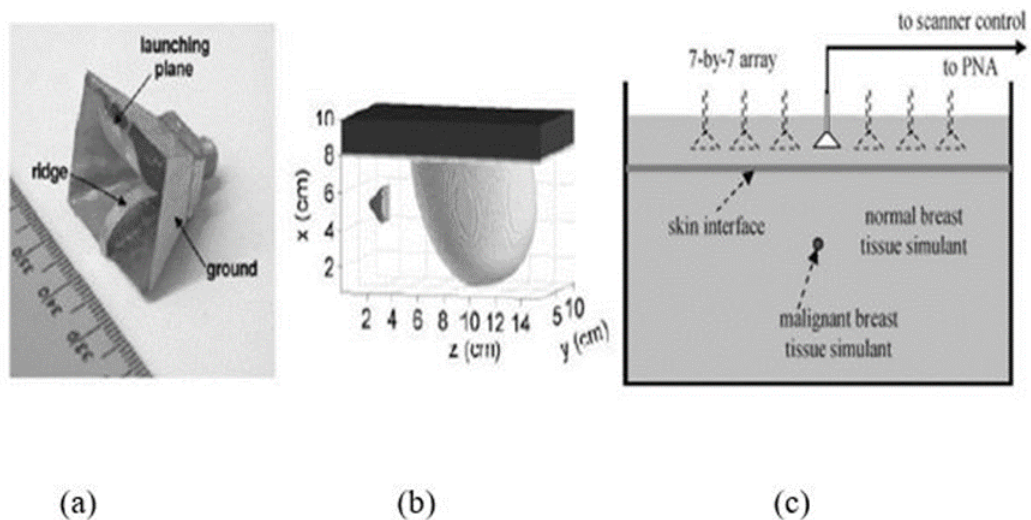
Figure 2.15: (a) Horn antenna, (b) 3-D FDTD prototype containing the breast model, and (c) view of the experimental set –up [63].

Figure 2.16: TSAR prototype system [64].

In [64], a group from the University of Calgary developed and implemented a breast imaging prototype of a radar-based monostatic setting. The system known as Tissue Sensing Adaptive Radar (TSAR) comprises of the patient interface, a sensor connected closer to the arm of the cylindrical tank motor, others are microwave computing gear, custom software including cables as shown in Figure 2.16. The system is identical to that developed by Dartmouth College and the University of Bristol. This configuration involves the patient's breast being extended through the hole of the inspection bench. Beneath the bench, there is a tank containing an immersion liquid, usually connected to the arm. Movement in both vertical and horizontal direction are achieved with the arms transfer of the sensor in the affected direction making circular rotation effectively and efficiently, as shown in Figure 2.17a and 2.17b, respectively [64].
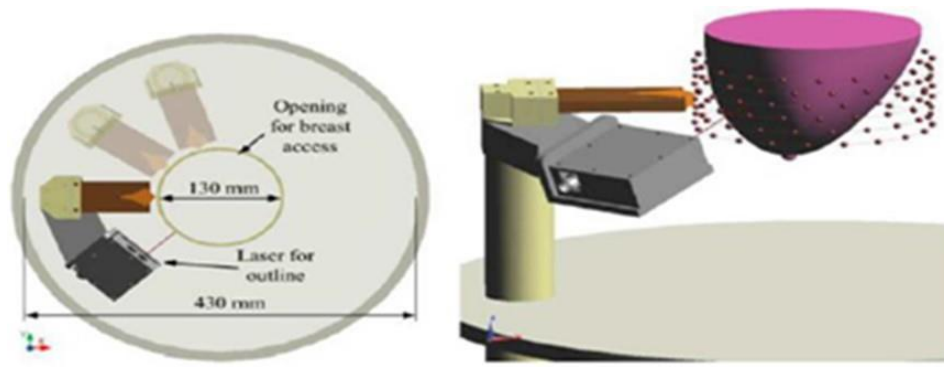
Figure 2.17: (a) Top-down assessment of the laser sensor and (b) configuration of the sensor and the breast on the rotating tank.

The sensor entails a UWB antenna with lasers presented as a confocal imaging device for breast cancer detection, particularly for tumour finding in 3-Dimensions. The main aim is to determine the contrast in the permittivities and conductivities of the normal and the malignant tissues enclosing the breast. This is achieved by using the imaging system to illuminate the target with UWB signals to a different location by the antenna, and the backscattered signals are received for analysis. Additionally, the strongly reflected signal is detected, localised in 3-Dimension with numerical analysis comprising of synthetic cylindrical and planar antenna array, as revealed in Figure 2.18 (a) and (b), respectively [21].
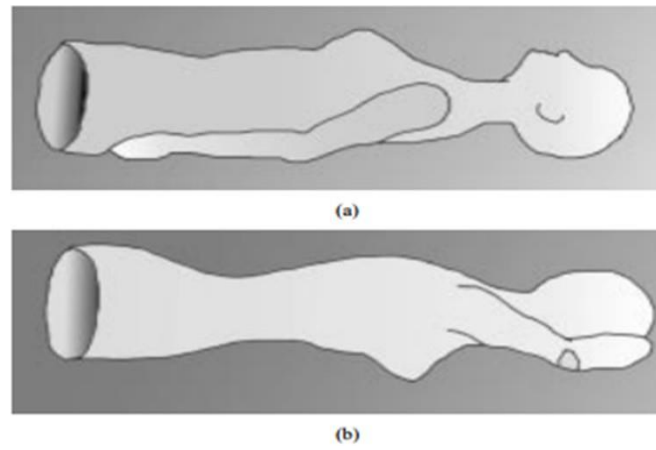
Figure 2.18: Patient positioning for (a) planar and (b) cylindrical methods [21].

In another novel experimentation, the research group from the University of Bradford developed and presented a sensor for imaging in the near-field. The fabricated sensor was achieved for monostatic radar-based breast imaging. A simple phantom comprises of container plastic structures having small dielectric materials simulating fatty tissues and containing more dielectric constants objects mimicking tumour is used in the spectrum of 4 GHz and 8 GHz with the aid of a microstrip antenna having UWB features [23]. In our experimental setup, an electrical property of a homogenous block characterised by the conductivity of $\sigma = 0.4$ S/m with a relative permittivity of $\varepsilon_r = 9$ of a cubical box of 150 mm size equivalent model is used as the interior breast model. Figure 2.19 indicates the tissue model with that of the antenna geometry. The resultant reflection coefficient of the antenna when in contact with the tissue and in free space was observed. The result revealed that the impedance matching of the antenna from 3.5 GHz frequencies up to 6.8 GHz was significantly affected by the existence of the tissue.
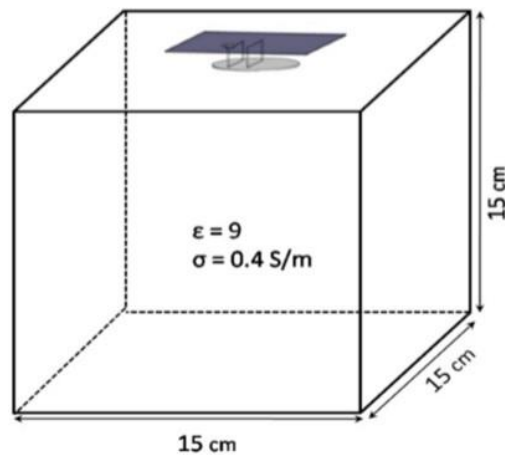
Figure 2.19: A tissue model with the Antenna [23].

Two prototypes of the antenna were fabricated having 0.25 mm copper properties one antennae with varactor diode while the other one without the varactor as shown in Figure 2.20. The Varactor diode is of model GaAs Hyper-rapid MGV 125-08H22 from Aero flex having a capacitance characteristics tuneable from 0.1-10.5pF over a 1-12 V reverse bias voltage range. The input of the antenna port terminal was integrated with a bias tee circuit. The analyser used for the dimensions was made of the HP 8510C model. The result from the experimental set up of Figure 2-21, revealed that the return loss at the input terminal of the antenna without the varactor indicates a complete practical agreement with that of the simulation analysis, as shown in Figure 2-22.
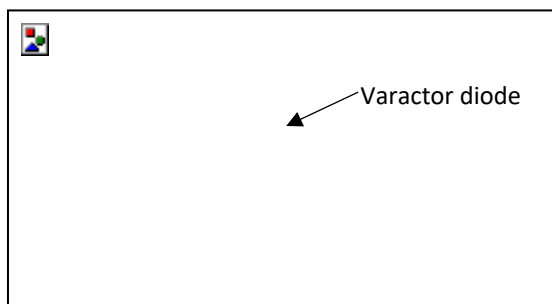
(a) with varactor

(b) without varactor

Figure 2.20: Physical antenna prototype [23].
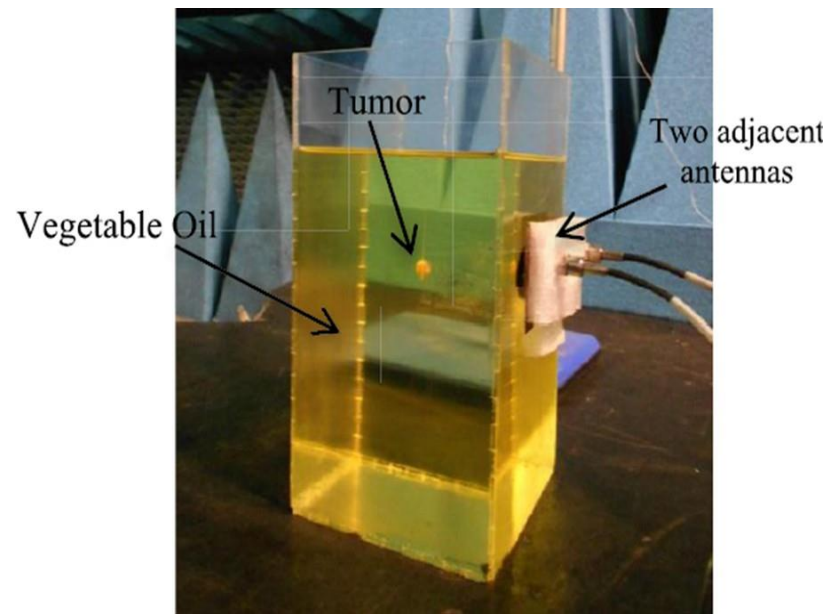
Figure 2.21: Indicating the experimental set up [23].
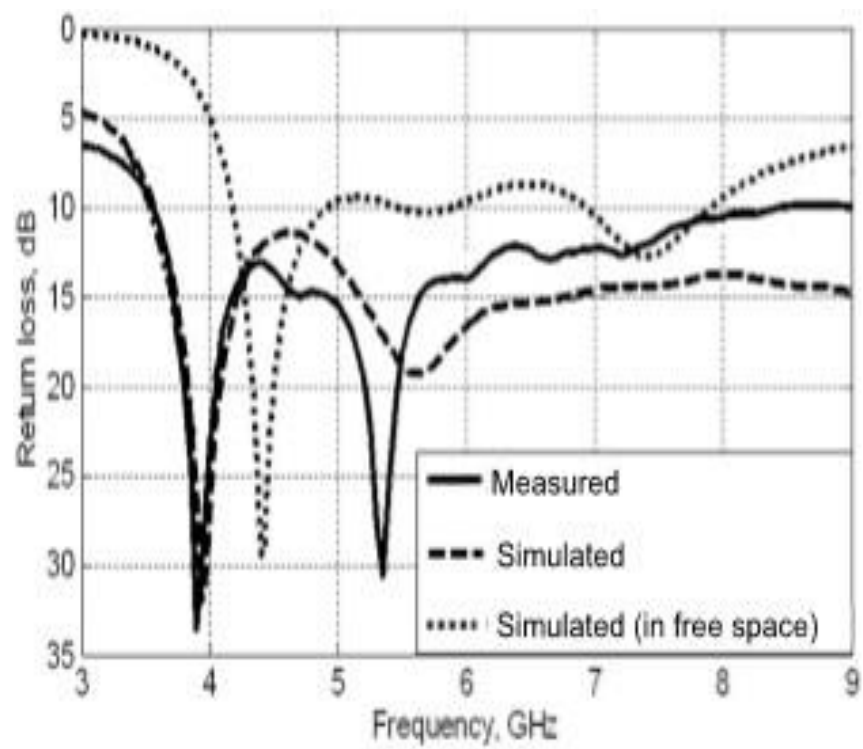
Figure 2.22: S$_{11}$ of the antenna with simulated and measured results [23].

2.9.2 *Current Status of Ground Penetrating Radar*

Ground Penetrating Radar (GPR) is also known as ground probing radar, surface penetrating radar, subsurface radar, geo radar, or impulse radar. This technique of imaging offers an innovative technology of inspecting rock and underground soil conditions. It is a well established geophysical technique that detects electrical discontinuities in the shallow surface less than 50 m. This is realised by generation, transmission, propagation, reflection, and reception of discrete pulses of high-frequency electromagnetic energy. Although the GPR technique was developed and put in practical use in the 70s and commercially available in the 1980s, and geologists began to exploits these promising techniques around the years of the 1990s [65, 66].

High-resolution imaging with a depth of 0 -10 m and even up to 50m in some geological environment is readily achievable [67-70]. GPR, as a promising technology, is currently applied in various inspection purposes, such as in the discovery of hidden pipes beneath the earth's surface, inspection of road layers in road construction and location, and mapping of steel in concrete structures [71-74]. The ground material properties have a significant effect on the GPR system when used in the practical scenarios, and the effects will vary the fundamental antenna properties, including its input impedance and radiation characteristics owing to its proximity to the ground. This results in a detection time of fewer than 100 ns or even a few nanoseconds in shallow targets. To avoid this anomaly, an antenna for this kind of imaging needs to be able to transmit and receive the signal with little or no distortion to evade concealing of the target of interest [75, 76]. It can be seen that antenna design is the primary bedrock of this promising technology. Various sensors were designed previously for GPR innovations in different research groups, including bow-tie dipole, horn antenna, spiral antenna,

and Vivaldi antenna. Some of these designed GPR and antenna systems are reviewed below.

A research group from the University of Tennessee and Georgia institute of technology presented a land mine detection system using GPR technology based on the resistively loaded vee dipole antenna to detect a buried anti-personnel land mine. The study was conducted by radiating a short pulse of the signal to two different soil materials, one with a replica of land mine buried. The analysis was carried out with a one-dimensional (1-D) analysis on both the experimented ground. This method is utilised in choosing the radiated signal having the same dimension with a segregated Gaussian pulse of the spectrum at 4 GHz. The dielectric properties of the Vee dipole are linearly tapered when fed at the open ends of the antenna. A three-dimensional (3-D) finite-difference time-domain (FDTD) model is developed and used to simulate the GPR land mine detection problem. Using this model, a resistively loaded Vee dipole is selected and evaluated. The result significantly improved the antenna performance in effectively classifying and characterising the land mines [41, 77-79]. The antenna was improved to have low loss and better VSWR by preserving the antenna arms and thus; changing its resistive configuration [80].

Another research group from the centre for Northeast Asian Studies of the Tohoku University developed a handheld dual radar sensing device for the discovery of hidden land mines named as Advanced Landmine Imaging System (ALIS) [81-83]. The sensor head is made of a metal detector, a GPR and a tracking system for recording the GPR and metal detector signal with their corresponding locations which are for training activities in Croatia as indicated in Figure 2.23.

Figure 2.23: Sensor head of ALIS system [83].

Another group from the centre for chemistry and the dynamics of geosphere research in Germany and International Institute for Geo-Information Science and Earth Observation, ITC, Netherlands also implemented research on the discovery water table in the area of Sardon and Salamanca, Spain. In the study, GPR was used in the semi-arid Sardon area of Salamanca, in Spain in order to analyse the distribution of the water table depth with a high spatial resolution to serve as input in the parameterisation of a hydrological model [84, 85]. A bowtie antenna with a centre frequency of 200 MHz connected with a GPS and a survey wheel for precise positioning was used for this process. Readings were conducted succeeding a sequence of splits passing uprightly the bed of the Sardon streams which were usually dry in September 2009. Measurement was carried out on the deeper side of the water table in numerous experimented wells to understands and confirm the GPR information, as shown in Figure 2.24. The time-domain reflectometry device determined the estimate of the shallow soil electrical properties. The experimental analysis has shown that the water table was having a depth of about 2 to 3 meters.

Figure 2.24: The GPR system towed for the detection process. [84].

The Delft University of Technology and International Research Centre for Telecommunications and Radar system presented and implemented various kinds of GPR radar for different applications. A UWB array-based radar for landmine detection was presented [86]. The system was implemented on a multi-sensor device for mine-sweeping operations. The focal point of the radar system is in the sectional approach, antenna system design and signal orientation of the transmit antenna input impedance. The concentration of the radar ability is based on the near-field beamforming across the direction and migration path. These sectional approaches consist of mini radar systems with own mini radar having its complete GPR electronics accessories including a pulse generator, multi-channel receiver and analogue-to-digital converters utilised in carrying out landmine detection and arrangement autonomously of other modules. Each mini-radar serves independently from each other with a firing time synchronised in such a way that they do not produce any interference among the elements. The radar system consists of arrays elements with the transmitting antenna elevated 70 cm above the ground surfaces and the receiving antennas 50 cm beneath the transmitting antenna as indicated in Figure 2.25. The complete antenna system was mounted on the multi-sensor trolley system for land mine detection, as indicated in Figure 2.26. and 2.27 respectively [87].
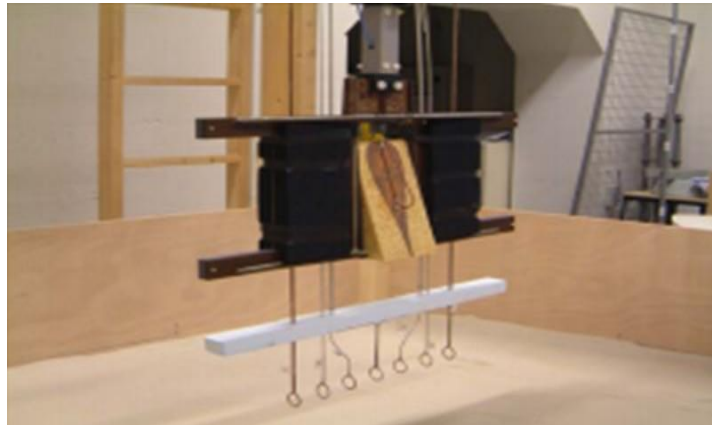
Figure 2.25: The antenna array system [87].

Figure 2.26: Antenna set of the radar system mounted on the platform [87].

Figure 2.27: Multi-sensor test for land mine detection [87].

2.9.3   Current Status of Through -the- Wall Imaging

Imaging for Through-the-wall investigations has received considerable responsiveness for sensing and imaging of moving and stationary objects through opaque obstacles that are not visible with our naked eyes such as walls. The demands are due to its urgent needs in counter-terrorism, urban warfare, security agencies, victims of earthquake survivor, confined human position, calamity rescue operations and concealed weapon discovery. UWB through the wall imaging applications have been investigated over the years by research institutes, companies and laboratories which work on the UWB through the wall imaging system [88-92].

A research group from the University of Tennessee presented and developed a sampling oscilloscope based UWB see-through wall imaging system for drywall imaging applications with high resolution. A total of 16 antipodal Vivaldi elements were initially designed for the sub-arrays [93]. The sub-array has a spectrum range of 8 GHz to 12 GHz and 3-dB beam-width along with the radiation pattern. Although the system has a high gain of 13 dB -14 dB, the operating frequency is a thing of concern due to the high wall losses that are usually encountered when imaging with high-frequency ranges. In [94], the 16 subarrays were modelled to generate a complete Vivaldi Array, as indicated in Figure 2.28, including the SP 16T switch. The configured SAR-based system consists of a UWB Vivaldi array, RF devices and hardware and software arrangement, as shown in Figure 2.29. The first system that was operated on 8 GHz – 12 GHz was scaled down to the spectrum of 2 GHz – 4 GHz more appropriate for the see-through- the wall analysis.

<div align="center">(a)   (b)</div>
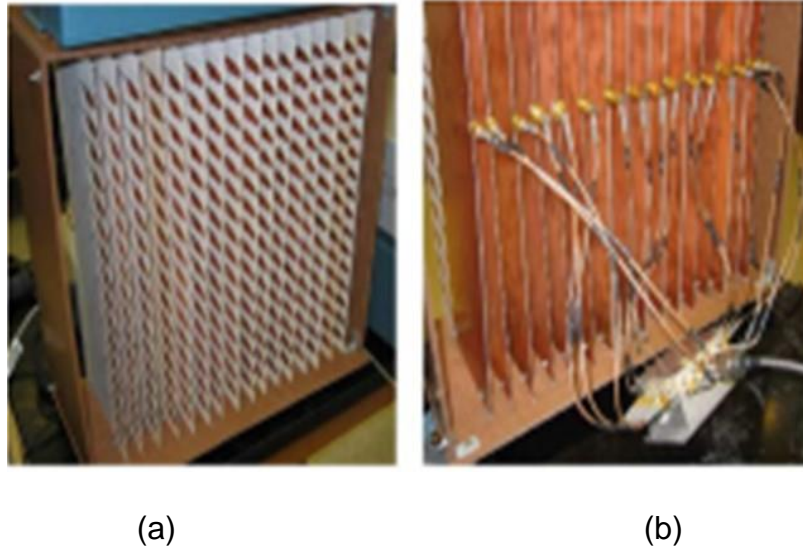
Figure 2.28: (a) Full array and (b) SP 16T switch [94].

Figure 2.29: See-through the wall imaging set-up [94].

Another research group from the Universität Duisburg-Essen Germany proposed and executed a fully Polarimetric 2D-bi-static UWB imaging device for examining a target with a fragile scattering axis. The misappropriation of polarisation scale provides supplementary data as related to mono-polarised detecting procedures. This variety in the polarisation is used to increase the efficacy of target characterisation based on the data received in the reflected signal. This development leads to the derivation of further targets characteristics, including details of surface structure and its corresponding orientation. An investigational

authentication based on complex test objects was achieved with an M-sequence Radar scheme having modern dual-orthogonal polarised antennas [95].

The group went further in upgrading and adopting a fully polyrhythmic 3D bi-static UWB radar-imaging structure for the assessment of the target of interest using weak scattering axis. To achieve higher resolution, a radar with an operating band covering a spectrum ranging from 4.5 GHz -13.5 GHz with a new quadrature modulator was adopted with a centre frequency that operates at 9 GHz. The new, improved imaging comprises of a couple of directive Teflon containing a pair of tapered slot line Vivaldi antenna operating on one substrate with a spectrum covering from 4.5 GHz-13.5 GHz as shown in Figure 2.30. The configuration utilised spaces and achieves a higher gain of 15 dBi with a beamwidth of 25° when compared with an array of two distinct antennas. Although this improvement satisfies the short-range resolution of the imaging system, there is the need for an additional improvement to cater for the focusing characteristics. These generate energy that is spatially distributed when a target of interest for examination was not discovered within the lobe having the maximum radiation in the antenna array.
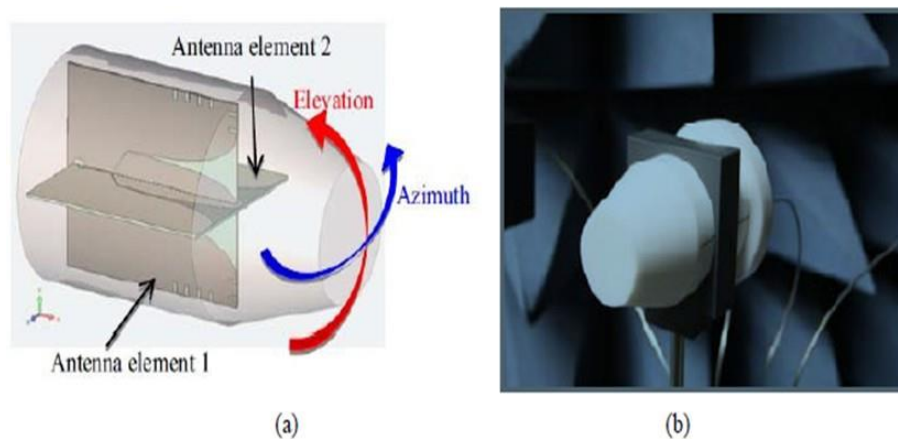
Figure 2.30: Dual-polarimetric antennas used in the imaging system at the Universität Duisburg-Essen. (a) The model, (b) the assembled configuration [95].

The use of UWB 3-Dimensional system was presented and implemented by Manor Research Ltd. The imaging system is designed to image and detect targets concealed in a suitcase and be able to detect the movement of people from a specified distance. The configuration uses the bi-static radar system configuration [96, 97]. In the configuration, four antenna arrays elements were used with each pair used as two independent units arranged in co-polar horizontal and vertical polarisation with each array units having 25 elements, as indicated in Figure 2.31. The system could be used for multiple applications, but its only set back is its size that is a thing of concern.
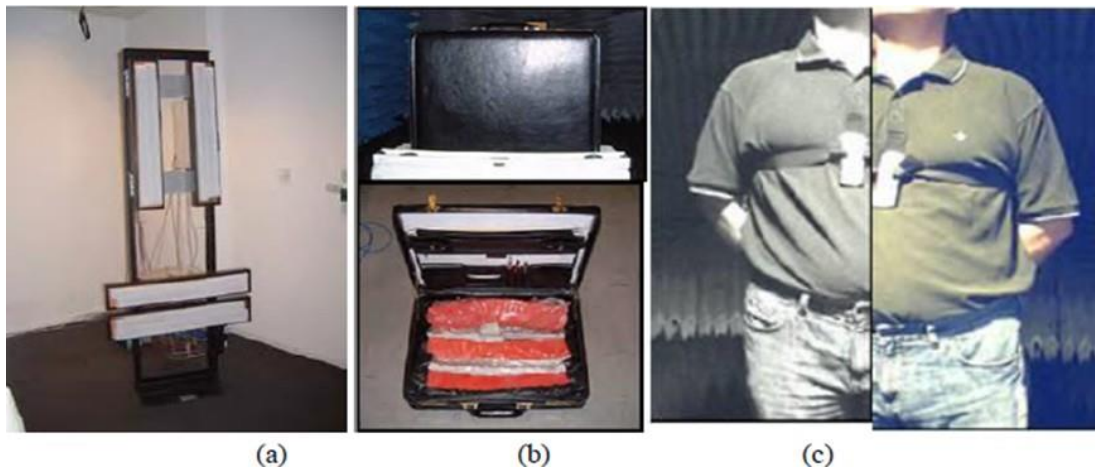
Figure 2.31: 3-D Imaging System designed by Manor (a) Complete System Configuration (b) Imaging Suitcase (c) Imaging human being [97].

Furthermore, a research group from the Queen Mary, University of London developed and presented a 2-D imaging system for the discovery of shielded metallic weapons in bags/suitcase by using UWB imaging system [98]. A pair of UWB sensors such as circular-edge antipodal Vivaldi antenna and the corrugated balanced antipodal Vivaldi antenna (BAVA) are used and studied in time and frequency domain respectively.

The operating frequency is in the range of 3.1 GHz to 10.6 GHz having stable radiation patterns. In the analysis of these antennas, the gain of the corrugated BAVA with smaller dimension has been improved to 7dBi through the operating frequency range, as indicated in Figure 2.32. Additionally, less signal distortion was generated in the time domain. Therefore, their study of the imaging system utilised the corrugated BAVA as the main sensor of the array. In the arrangement of the rotating antenna array, there is a single principal transmitting antenna and four receiving antennas. The receiving antennas rotate around the central transmitting antenna, and these are placed side-by-side to each other.

The two-dimensional beamforming method has been established centred on the DAS algorithm. This UWB imaging system can identify and rebuild the image of the single and double metallic targets concealed enclosed in the bag. The least single target with a size of 4 cm × 4 cm × 1 cm has been formed indicating images having a maximum distance of 30 cm away from the system. The imaging system can attain 6 cm in cross-range resolution and 15 cm in down-range resolution. However, the imaging needs to be improved in order to achieve more cross-range resolution of the imaging system. These can be achieved by increasing the receiving antennas in the antenna array element. Furthermore, the DAS imaging algorithm used in the image reconstruction algorithm suffered from clutter rejection and lack of detecting multiple scatterers, particularly in the highly-dense target. Hence, the system needs to be improved on the signal processing algorithm by adopting more advanced imaging algorithms such as modified weighted delay and sum (MWDAS) and Filtered Delay and Sum (FDAS) that can detect even non-metallic target in a more challenging propagation environment with various obstructions.
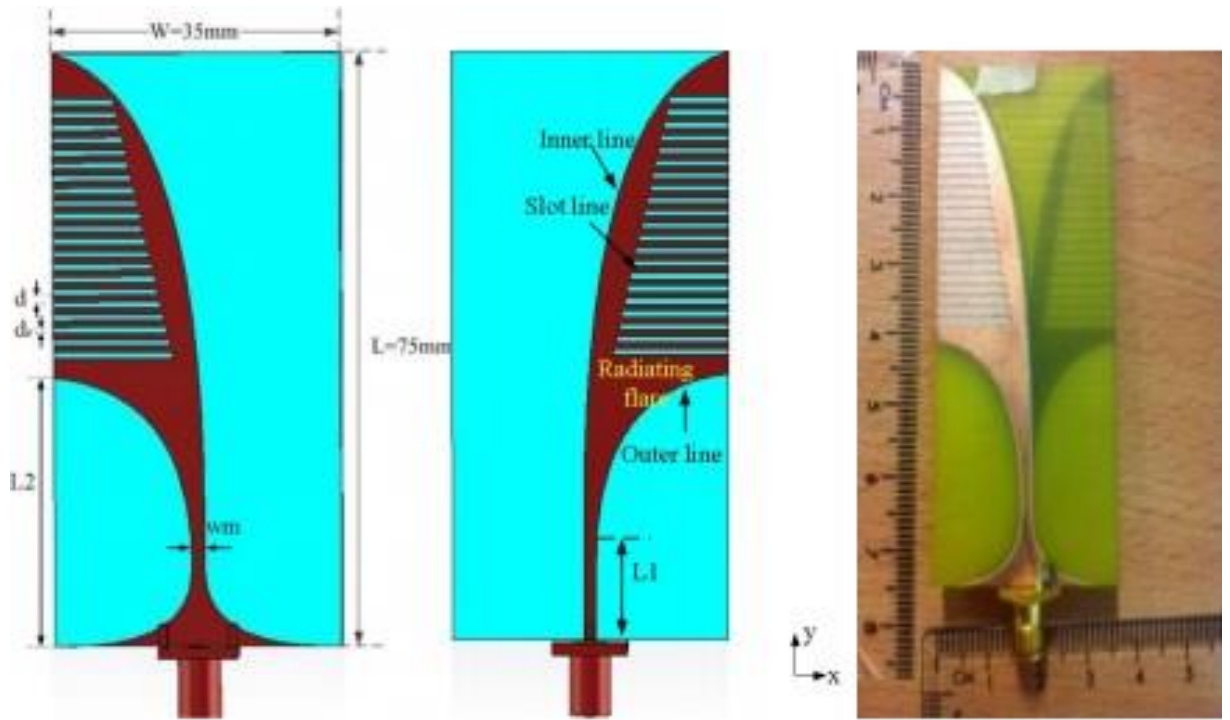
Figure 2.32: The structure of the designed corrugated BAVA with (a) top layer (b) bottom layer and (c) the fabricated antenna [98].

The University of Bradford implemented an experiment on through the wall imaging by using a bow-tie dipole antenna adjacent to the dielectric material. In our analysis, the antenna shape was parametrised and optimised to reduce the return loss within the spectrum ranging from 1.6 GHz to 3.5 GHz and also to reduce the interference experienced at high-frequency range with the wall materials [99].

The modelling and analysis of the antenna are carried out using the hybrid Finite Difference Time Domain (FDTD) /Method of Moments Computational Electromagnetic Technique (CET). The method is widely used for analysing complex electromagnetic problems to simulate the interaction between the Electro-Magnetic (EM) field and the inhomogeneous anisotropy dielectric material such as the wall cavity. The hybrid method is thus developed to allow an effective and efficient way of analysing such CET combination that either method could be used

independently to achieve the desired results. Results are simulated using CST

software package, which gives promising outcomes as shown in Figures 2.34.
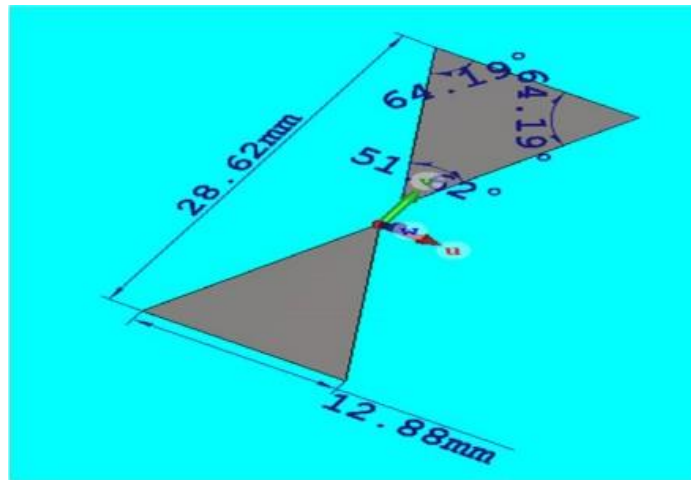
Figure 2.33: Bowtie antenna design geometry [99].
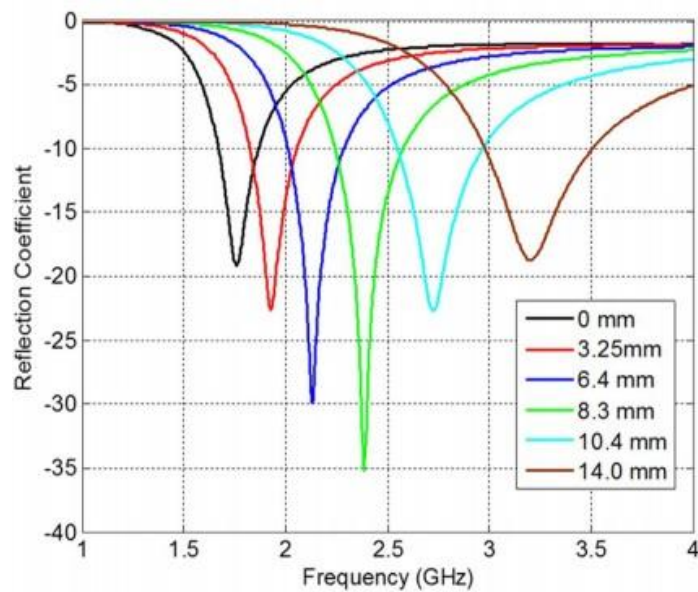
Figure 2.34: Return loss of the designed antenna [99].

2.10 Principles of Microwaves Imaging

Microwaves imaging has been used extensively to image different dielectric

substances ranging from concrete, living tissues, bricks, woods, ceramics, paper,

glass, soil, and fog. This technology adopts the principle of Ground Penetrating Radar, which is based on the transmission, and reflection of electromagnetic waves. Radar system causes the transmitter to radiate a periodic train of very-short electromagnetic pulse, which is used for various propagation. Variation in the electrical properties of the subsurface medium causes part of the transmitted signal to be reflected. The receiver, which is later processed, and display as depicted in the block diagram below, accept this reflected signal:
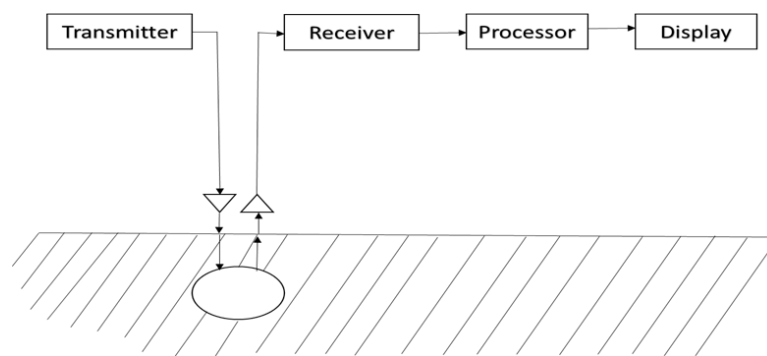
Figure 2.35: Block diagram of a Ground Penetrating Radar.

2.11 Operation Methodology of a Typical Ground Penetrating Radar

Ground Penetrating Radar (GPR) is a type of radar system that consists of four main parts, as illustrated in Figure. 2.35. Including transmitting and receiving antenna, processor or control unit and the computer or display. The transmitter emits a short pulse of electromagnetic waves with the duration of few nanoseconds into the target of interest, some parts of the waves were reflected when in contact with media of different dielectric properties such as permittivity and conductivity and other waves are partly transmitted into the deeper layer of the ground. The reflected signal is recorded in the receiving antenna located either in the same box with the transmitting antenna (mono-static) or in a separate antenna box as the transmitter (bi-static). The data acquired will be fed into the processing unit for

sampling, filtering, transforming into time domain from the frequency-domain before the image is appropriately mapped for analysis and displayed. Accuracy of the travelling time is achieved by having an equal travelling distance of both transmitter and receiver from the ground [100].

The different medium consists of different electrical properties; as such, the travel time for the propagated wave will also be different. GPR operates on a frequency ranging from 10 MHz for deep geological and glacial applications to 2 GHz for shallow and non-destructive testing and structure evaluation with high image resolution to a depth of typically 0 m – 10 m. However, the depth of 40 m is also possible in some geological environments [101]. The main set back of a GPR system is the interference of a ground electrical property with the input impedance and radiation characteristics of the antenna due to its proximity to the ground level. Usually, the detection time is less than 100ns. For shallow targets, a few nano-seconds is sometimes realised. Thus, the designed antenna should transmit a signal with little distortion in order to limit the concealment of the target echoes and coupling of the electromagnetic energy into the ground [75].To achieve efficient and effective operation, a typical GPR should satisfy the following condition [102]:

- Sufficient signal to noise ratio.
- Sufficient signal to clutter ratio.
- Sufficient depth resolution of the target.
- Sufficient spatial resolution of the target.

The above conditions can be optimally achieved when factors such as the clutter, path loss and system dynamic range are considered efficiently and effectively. The range of the GPR system consists of losses such as material loss, spreading loss, scattering loss and total path loss [102, 103]. Furthermore, to achieve sufficient

depth and spatial resolution of the targets, it is desired to have antenna elements that can operate over a wide range of frequency and radiate short duration pulses in order to achieve better resolution and imaging quality [104].

2.12   Conclusion

This chapter highlights the history, fundamentals and system performance of the antenna being the primary sensor for microwave imaging applications. It also gives the background, features including the advantages and disadvantages of UWB technology. Additionally, overviews of relevant works already reported in the field of microwave imaging which is of relevance to this work are reviewed. This is followed by the principles of microwaves imaging applications and operation methodology of ground penetrating radar through which the concept of microwave imaging was adopted.

Chapter 3

Ultra-wideband Techniques for the Measurements of Attenuation and Dispersion through various Medium

3.1   Introduction

In a narrowband wireless system, signal distortion is caused due to multipath components. Conversely, UWB wireless system signal distortions are produced owing to the dispersive characteristics of the medium arising from the multipath components, propagation path and bandwidth limitations of the transmitting and receiving antennas. The choice of the appropriate numerical computations depends mainly on several factors including computer specifications, radiating objects with their corresponding scattering parameters, the type of measurement domain such as time or frequency-domain and the absorbing boundary conditions.

UWB radar imaging technique consists of two measurement techniques, namely; time-domain and frequency-domain measurement system. The choice of these measurement techniques is mainly dependent on the type of radar applications. The electrical properties of the medium play a very significant role in the determination of the measurement techniques used for the mathematical modelling adopted in any electromagnetic coupling problems. For instance, in medical imaging, the geometry modelling consists of several features, including anisotropy/inhomogeneous and easier objects penetration that proves difficult in the formulation.

3.1.1 _Time-Domain Ultra-wide Band Measurement Techniques_

The time-domain UWB imaging technique consists of a pair of UWB transmitting and receiving antennas, a pulse generator, a triggering signal generator and a digital sampling oscilloscope, as shown in Figure 3. 1. In this technique, a periodic train of very-short-duration Gaussian type pulses distanced by sufficiently long time intervals is used for the UWB measurements of the signal propagation through the walls [38]. The pulse generator is connected to the transmitting antenna via a UWB low-loss cable. A UWB transmitting antenna with a large bandwidth is used to achieve minimum signal distortions to radiates these pulses. Connected at the feed points of the transmitting antenna, is a low noise power amplifier required for higher amounts of radiated power. At the receiving end, the UWB receiving antenna captures the signals. The receive antenna is connected to the digital sampling oscilloscope with the aid of UWB cable, and the sampling oscilloscope detects these signals. A low noise amplifier is connected at the output of the received antenna to increase the received signal power.

Figure 3.1: Schematic Set-up for time-domain measurements techniques.

An issue of utmost importance in this type of measurement system is the synchronisation of transmitting and receiving the signal. The synchronisation is achieved by establishing a low jitter triggering signals between the pulse generator and the digital sampling oscilloscope. The sampling oscilloscope requires this signal and achieve by using a step generator driver to supply the trigger signal and the pre-trigger signals. As such, the time delay produced by the triggering cables and the propagation path of the pulses can be calculated and compensated by adjusting the time delay between the pre-trigger signal and trigger signal.

Calibration of the system aid in eliminating the effects of non-ideal characteristics of the measuring instruments from the measured data. Furthermore, the signal received is affected by noise and interference from different sources. The noise can be either narrow-band or UWB noise. The narrow-band noise is sinusoidal and is usually due to electromagnetic interference in the nearby narrowband system, which can be eliminated through bandpass filtering. The UWB appears in the form of random short pulses which can be eliminated or reduced through multiple signal averaging. Calibration guarantees the stability of the systems and removes any interference available. Due to its enormous potential, the time domain system is a well-established system of designing and construction. It can be cost-effective, very portable for system applications and offers direct testing results.

3.1.2 *Frequency-Domain Ultra-wide Band Measurement Techniques*

The frequency-domain UWB imaging technique for the measurement of

attenuation and dispersion of signal propagating through the medium is carried

out using Vector Network Analyser (VNA) [105]. The harmonic sweep generator performed sweep frequency measurement at different frequency ranges. The main advantage of this technique over time domain is the more extensive dynamic range for the measurement of the transfer function of the signal. This method examined the frequency, amplitude and phase of the measuring signal. In this technique, port 1 of the S-parameter test set is connected to the transmitter while port 2 is connected to the receiver, as shown in Figure 3.2.
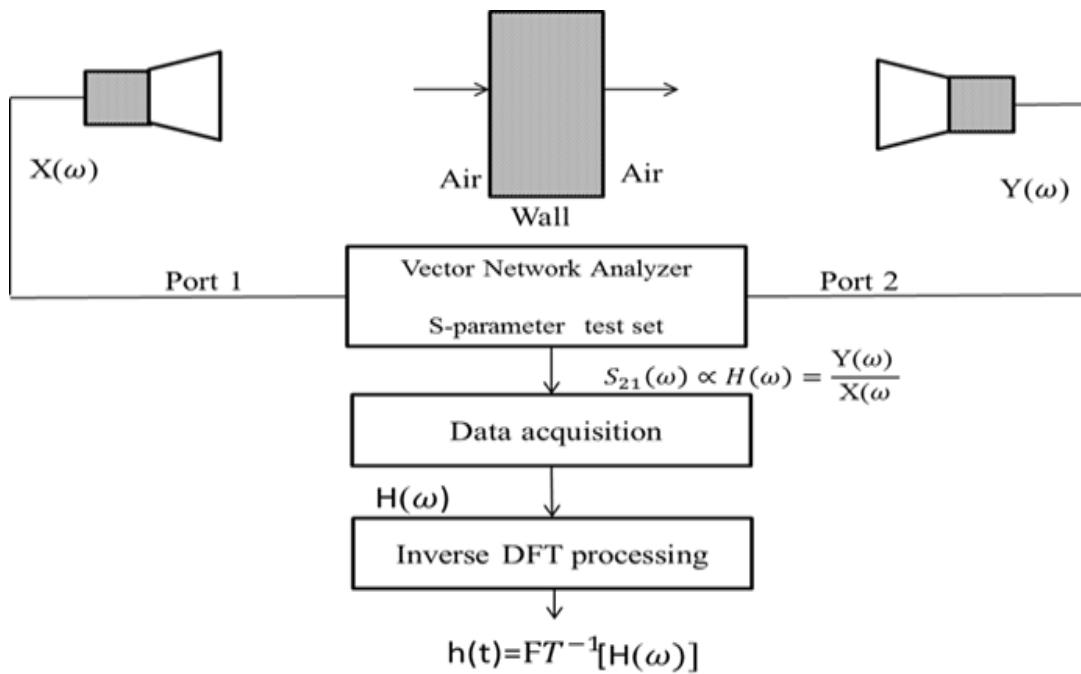
Figure 3.2: Schematic Set-up for frequency-domain-measurements techniques.

.

3.2   UWB Radar Numerical Computational Methods

Numerical computational techniques have been explored for microwave signal propagation within various medium structures, including medical tissues and wall structures. These analytical and numerical methods are based on Maxwell's time-dependent curl equations which have been widely used in solving complex electromagnetic scattering problems. Usually, these approaches of computational electromagnetic computational techniques were primarily used in areas including near and far-field regions [37], microwaves circuit analysis and design [106], electromagnetic compatibility [107, 108], the transmission mode of meta-material and optical scattering solution analysis [109, 110]. Other areas are medical diagnosis and communication systems [108].

Differential and integral numerical computational electromagnetic techniques are shown in Figure 3.3. These methods are Finite Difference Time Domain (FDTD), Finite Difference Frequency Domain (FDFD), Transmission Line Matrix (TLM), and Finite Element Method (FEM), others are Method of Moment (MoM) and Fast Multipole Method (FMM) as briefly discussed in the next section:
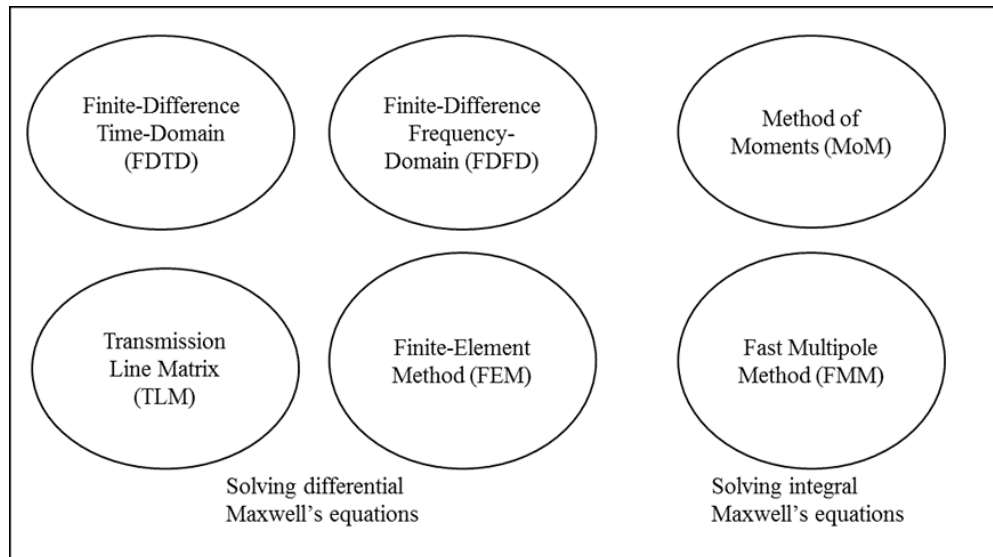
Figure 3.3: Numerical Analysis Techniques for Solving Maxwell's equations.

3.2.1 *Finite Difference Time Domain (FDTD)*

FDTD method is a numerical analysis technique used for solving Maxwell's equation. This technique modifies Maxwell's equation into central-difference equation by discretising them into space and time derivatives [111]. This method is generally considered due to the following advantages, including its simplicity, versatility, fidelity, effectiveness, robustness and also very suitable for solving transient analysis problem. Furthermore, the FDTD technique allows the assignment of material property at all points within the computational domain and also enables the modelling of a variety of dielectric and magnetic material [112]. The main disadvantage of this method is that only consistent grids can be employed [113]. As such, the geometry structure is restricted to stair case-shaped boundary, which requires high computer memory requirement and time duration for the CPU most especially when dealing with curvature geometries. Furthermore, the presence of error due to numerical dispersion also contributes to its set back [114].

3.2.2   Finite Difference Frequency Domain (FDFD)

FDFD method is another form of a numerical electromagnetic computational method similar to FDTD but based on frequency-domain. FDFD carry out the computation of Maxwell's equation in its time-harmonic form using a finite-difference approximation of the derivative operators. Although both methods share the same approximation constraints, their capability is different in that FDFD is more flexible in defining complex structures and can save more data than FDTD [115]. However, this is subject to extensive computation for solving large scale problems [116].

3.2.3   Transmission Line Matrix (TLM)

TLM method is another numerical analysis technique in space and time approximation for the computation of Maxwell's equation. The method is based on the Huygens' method of wave propagation and scattering [117]. In this technique, the equivalence analogy between the voltages and current of the transmission lines and EM field propagation is achieved as a result of the mapping of the transmission line equation and Maxwell's equation [118]. TLM also allows the computation of complex 3-D EM structures with great flexibility because it incorporates EM fields, material media and their interaction with boundaries. However, their flexibility is based at the expense of additional memory requirement.

3.2.4   Finite Element Method (FEM)

FEM is also a numerical analysis technique which is used in dividing the large domain into subdomain or region known as a finite element. In this method, the integral part of the finite element will be approximated by summing up the value

of each of the finite element [119]. By assuming a boundary condition, the value of each of the finite element will be calculated iteratively to achieve the total approximation of the system [120]. One of the significant advantages of FEM technique is its flexibility in analysing problems with complicated domain and assigning each domain with a different resolution. However, the technique is not suitable for modelling many EM interference problem [121].

3.2.5 *Method of Moments (MoM)*

The MoM is a numerical analysis technique aimed at solving the integral form of Maxwell equation by minimising them into the system of linear equation [122]. In this method, the structure is discretised into planar and curvilinear triangular elements [123]. A matrix representation of the structure will then be established based on the number of segments achieved. The distribution of the problem structure can then be calculated with different input parameters such as near-field, far-field and impedance. MoM is highly effective when perfectly conducting wires scattered are the type of problem encountered.

The technique is also exploited in such a way to size various applications such as in solving problems of the integral equations as those found in [124-132]. Additionally, the method is very suitable for solving scattering problems and antenna designs, but the size of the objects should not be more significant than a few wavelengths. The spectrum response may be deemed as the attractive element, which the Method of Moments can deal with, particularly in the frequency-domain. This will lead to exact input impedance variations over a broad range of the spectrum. The antenna input impedance is commonly known as the ratio of the voltage to the current at its input port. It may be accomplished from

the numerical technique solution through the integral equation; this is broadly referred to as the Integral Equation Method of Moments [133].

3.2.6 *Fast Multipole Method (FMM)*

Fast Multipole Method (FMM) is a numerical analysis technique which was initially proposed to solve the classical boundary value problem [134]. However, the method is now extended to solve both acoustic and EM scattering problems [135]. FMM offers a solution to both reduced memory storage and computational complexity which can be used in the application of modelling techniques such as Method of Moment and other problems which are before impossible to address.

3.3 UWB Antenna Design Optimisation Techniques

An antenna is a primary sensor for microwave imaging, automobile, satellites and wireless communications system design. Design optimisation has now replaced the outdated trial and error concept and generally adopted as the standard design process for microwave antenna simulation. The optimisation is usually needed in all engineering disciplines to enable engineers to get the best specifications out of their devices [136]. Small variations in the system dimension can have a multiplier effect on the overall system efficiency. In a system with multiple variables, interactions between them can be very tedious and hence finding their optimum value can be near to impractical. Hence the need for an efficient optimisation method for the simulation. There are currently local and global optimisation methods for the simulation of computational electromagnetic techniques [136]. These optimisation techniques are used in commercial electromagnetic (EM) simulation software package including Computer Simulation Technology (CST) Microwave Studio, Ansoft High-Frequency Simulation Structure (HFSS), Advanced Design System-Momentum (ADS),

MATLAB antenna toolbox and Altair- FEIdberechnung für Körper mit beliebiger Oberfläche (FEKO), translated as "field calculations involving bodies of arbitrary shape".

3.3.1 *Local Optimisation Method*

Local Optimisation Methods are those types of optimisation methods which require an excellent starting method or the initial values are used as a reasonable estimate of the optimum value [137]. These are not often available for antenna design. Hence, using this kind of optimisation method would not guarantee a satisfactory solution to the problem. Local Optimisation methods include Quasi-Newton (QN), Sequential Quadratic Programming (SQP), and the Trust-Region Network (TN) methods.

3.3.2 *GLobal Optimisation Method*

Global Optimisation Method is those optimisation techniques which searches the entire optimisation spaces. These methods are best suited for large or complex parameter space as well as for a situation where there is no clear starting point [138]. However, it requires much time for the optimisation task. Examples of global optimisation methods are Surrogate Model Assisted Differential Evolution Algorithm optimiser (SADEA), Particle Swarm Optimisation (PSO), Genetic Algorithm (GA), and Covariance Matrix Adaptation Evolutionary Strategy (CMA-ES). Due to their effective and efficient performance for antenna optimisation, three global optimisation techniques are compared in this work. The classifications of these optimisation techniques are illustrated in Figure 3.4.
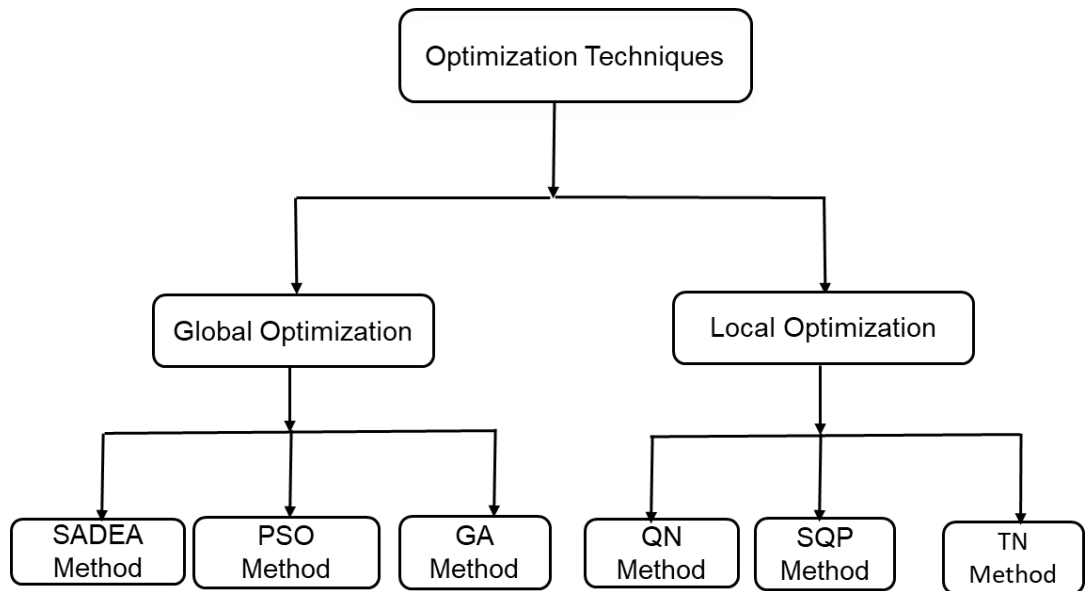
Figure 3.4: Classifications of optimisation techniques.

An overview of the Global Optimisation Techniques will be highlighted starting with SADEA Algorithm.

3.3.2.1 *Surrogate Model Assisted Differential Evolution Algorithm (SADEA)*

SADEA Method is an evolutionary computational method used in optimising a problem by employing surrogate models to replace the computationally expensive function evaluations (e.g., high-fidelity EM simulations). The Algorithm uses Differential evolution (DE) which is chosen as the search machine while the Gaussian Process (GP) is selected as the method for surrogate modelling. The surrogate model structure is used to forecast the function values cost which requires much less effort than directly embedding the computationally expensive function evaluator (e.g., EM simulator) within the optimiser, as such the computational cost would be significantly reduced [134]. Figure 3.5 indicates the flow diagram of a SADEA Optimiser.
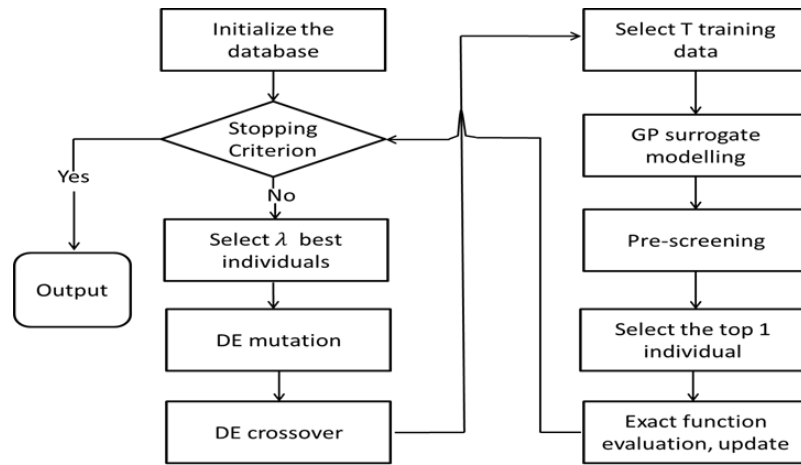
Figure 3.5: Flow diagram of SADEA Optimiser.

3.3.2.2 *Particle Swarm Optimisation (PSO)*

PSO is another global computational evolutionary optimisation method based on the movement and intelligence of swarm [139]. This algorithm treats points in parameter space as moving particles. In this optimisation method, the position of the particles changes not only to the best-known position but also to the best position of the entire swarm at each given iteration. The method is also used in solving optimisation problems with many parameters. Figure 3.6 is the flow chart of the PSO.
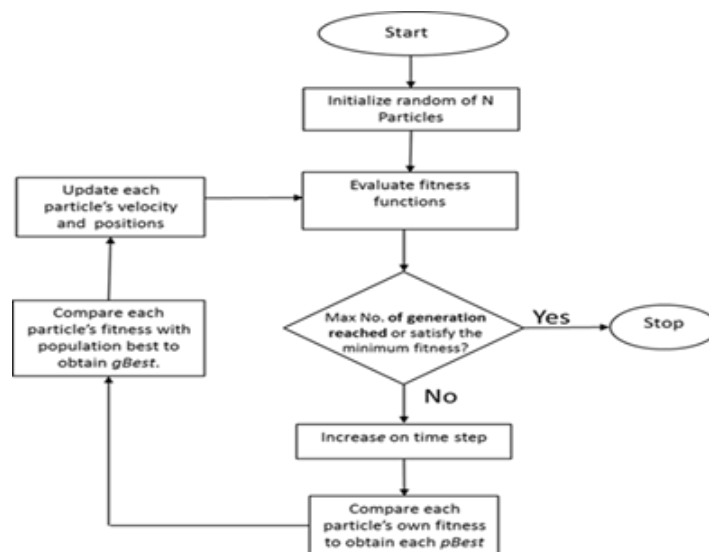
Figure 3.6: Flow diagram of PSO Optimiser.

3.3.2.3   *Genetic Algorithm (GA)*

Genetic Algorithms are computational optimisation method used for the optimisation of a problem space based on the principle of natural selection and evolution [140]. The heuristic technique, utilise the natural evolution to generate points in parameter space regularly and then refines them through multiple generations with random parameter mutation [141-143]. The generation is usually achieved using the various natural evolution techniques, such as inheritance, mutation, selection and cross over. The algorithms are suitable for complex problems domain and models with many parameters. Figure 3.7 is the flow chart of the GA.
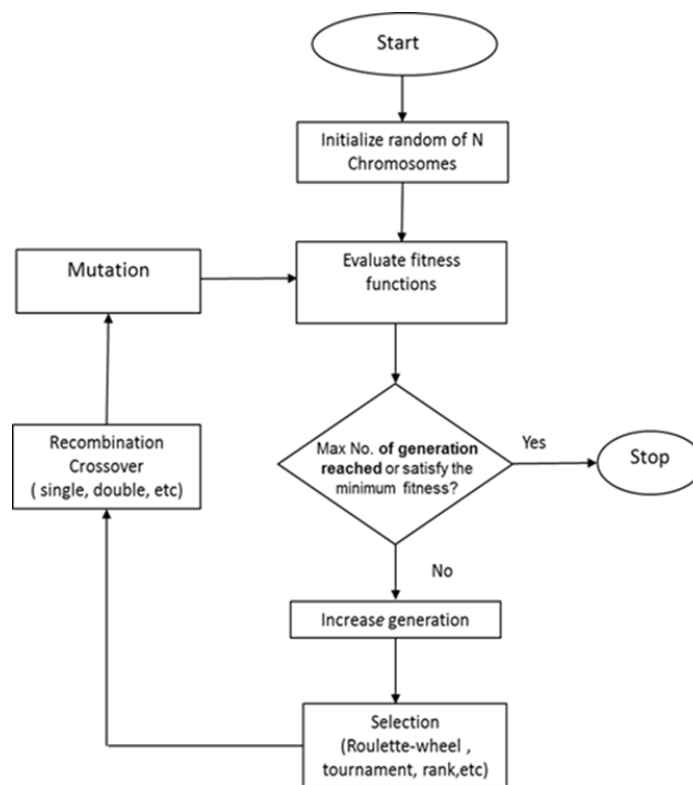
Figure 3.7: Flow chart of the Genetic Algorithm.

The above local and global optimisation techniques are used in the commercial software packages as categorised in Table 3.1.

Table 3.1: Categorisation of Optimisation techniques using the software.

Optimisation Methods	CST	HFSS	MATLAB	FEKO	ADE
SADEA					✓
PSO	✓		✓	✓	
GA	✓		✓	✓	
QN		✓	✓		
SQP			✓		
TN	✓				

In this work, the three global optimisation techniques were used for the optimisation comparison purposes of a compact ultra-wideband (UWB) printed circular monopole antenna (PCMA) for microwave imaging applications, specifically for breast cancer detection. The profile of the proposed antenna features T-Slots etching over a driven circular patch. To achieve the desired UWB impedance bandwidth both in free-space and in proximity to human tissues, the geometrical profiles of the T- slot monopole antenna is optimised using the three global optimisers for comparison purposes. The values in Table 3.2 shows the optimised bandwidth enhancement results for the three global optimisation methods on the PCMA. More details of the optimisation design analysis are indicated in Chapter 5.

Table 3.2: Comparison of three global optimisation techniques on PCMA analysis.

Method	Best BW	Worst BW	Average BW	Standard BW
SADEA	3.1-10.6 GHz	-	3.1-10.6 GHz	3.1-10.6 GHz
PSO	4.5 - 8.6 GHz	4.4 - 6.8 GHz	4.45 – 7.7 GHz	3.1-10.6 GHz
GA	4.4 - 7.6 GHz	4.3 - 5.6 GHz	4.35 - 6.6 GHz	3.1-10.6 GHz

From the above table, it can be seen that SADEA optimiser provides improved performance as compared to other global optimisers used for the analysis. Other features of SADEA algorithms over other global optimisers are as follows:

- Support efficient design exploration: Surrogate Model-Assisted Differential Evolution for Antenna Synthesis (SADEA), is designed to address efficient single objective antenna design exploration [144] ;

- Support multiobjective design exploration: Multiobjective optimisation method, Multi-objective Evolutionary Algorithm Based on Decomposition-Differential Evolution Operators (MOEA/D-DE) [145].

- Support antenna design engineers without sufficient expertise in optimisation: The usability concerns for the targeted users are studied and included in the tool, including automatic algorithmic parameter setting, efficient handling of geometrical constraints, interactive stopping criteria and graphics user interface (GUI) connecting CST Microwave Studio [12].

- It also Supports co-work with existing EM simulators and optimisers: The software is very compatible with existing tools in EM simulation software packages [144].

3.4   Conclusion

This chapter presents the UWB techniques for the Measurements of Attenuation and Dispersion through various Medium. It also provides the various UWB numerical computational electromagnetic techniques for microwave signal propagation within various medium structures. Additionally, the various optimisation techniques used in this work were highlighted, and comparison was made to make the right choice in order to obtain the optimal solution at the desired spectrum of interest. This chapter also identifies the improved features of SADEA over PSO and GA optimisation techniques which have fundamental impacts on the performance of UWB microwave imaging application system.

Chapter 4

Practical Antenna Design

4.1   Introduction

Increasing demand for wireless technology innovation has necessitated the needs for different kinds of antennas such as bow-tie, slot, patch antennas, Vivaldi and monopoles antennas particularly for microwave imaging applications [47, 58, 99, 146]. Antenna features such as compact size, low profile, lightweight, wideband, and multiple functional antenna designs are becoming more attractive in many microwave applications. In this section, different antenna structures are investigated in order to fulfil these requirements. Antennas for microwave imaging required simple fabrication, low cost, wide impedance bandwidth, and transmitting and receiving wideband signals without significant distortions [147, 148].

4.2   Bow-tie antennas microwave imaging applications

Bow-tie antenna depicts one of the simplest dipole antennas, which provides UWB performance despite its simplicity. The antenna is typically used in a frequency ranging from UHF to mm-wave that is used in many applications including arrays. Bow-tie antenna is easy to construct and can be very robust and significant, particularly at a very low frequency. The antenna is commonly supported by a dielectric substrate or manufactured using suspended metal cut-out. When a substrate is used, it is usually desirable to adopt a thin and low substrate for an improve antenna performance [149].

In this section, the design, optimisation and analysis of a Bowtie Dipole adjacent to Dielectric Material for through the wall microwave imaging application using hybrid electromagnetic computational analysis techniques were presented. Additionally, the experimental characterisation of the antenna in proximity to the wall material, including other performance indicators of the antenna was also analysed.

The proposed antenna was designed to optimise wide-band performance using SADEA algorithm in the UWB spectrum. The antenna also exhibits high immunity and stable radiation pattern in proximity to the wall materials. Following this section will cover the antenna geometry and design process.

4.2.1 *Antenna Geometry*

The geometry of the proposed isosceles triangle Bowtie antenna has the following total dimensions of L_s x W_s = 28.62 mm^2 x 12.88 mm^2 on an FR-4 substrate with ($e_{r\ =}$ 4.3, tan δ= 0.01 and thickness of 1.6 mm²). A 50 Ω coaxial transmission line is used to feed the antenna.

4.2.2 *Design Guidelines*

Figures 4.1 and 4.2 shows the primary and design parametrised geometry of the isosceles triangle Bowtie antenna with a total length of 0.2385 λ and width of 0.1073 λ. The dielectric dimensions are 1.66 λ of lengths, widths of 1.25 λ and thickness of 0.833 λ all wavelength are measured as a function of the centre frequency with $e_{r\ =}\ 5$ of and $\delta = 0.1$ which corresponds to the electrical properties of a typical concrete inserted into the hybrid domain of the total far-field region. The separation gap between the antenna and the dielectric was varied at 10 mm,

20 mm and 30 mm respectively. Figure 4.3 is the hybrid MoM/FDTD model used for the research. Figure 4.4 depicts the parametrised return loss at the input port for different value of k ranging from 0 mm-14 mm. It can be seen that a bandwidth of around 300 MHz could be obtained for the few arm lengths before the optimisation.

The optimisation was carried out using SADEA algorithm [145]. Figure 4.5 shows the improved bandwidth of 618 MHz. More details were shown in Table 1. Using the Huygens principle [150] which states that each point on a wave acts as a secondary source of the outgoing waves, the Huygens surface encloses the dielectric material and models using several cubical cells of 58 x 42 x 74 (with a cell size equivalent to 0.025 λ. (The flare angle was set at 30^0, 45^0 and 60^0 respectively which are used to optimise the bow tie arm length for the three gaps chosen away from the dielectric.
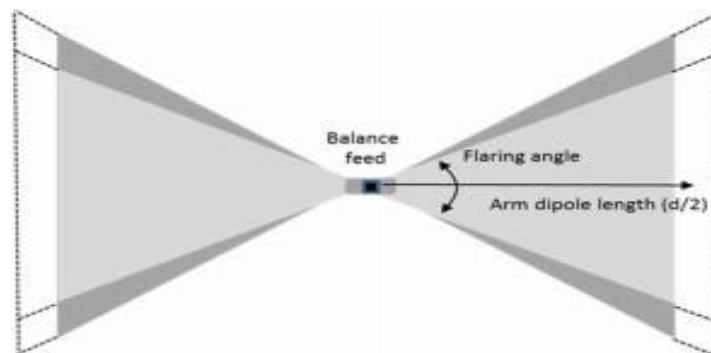
Figure 4.1: Basic geometry of the Bow-tie antenna [24].
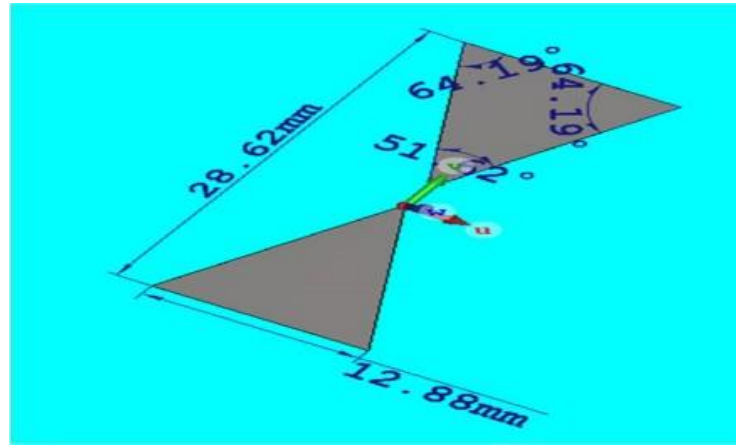
Figure 4.2: Design geometry of the Bow-tie antenna.

The hybrid formulation was achieved using MoM and FDTD, as illustrated in Figure 4.3. A few numbers of 3 to 4 iterations were considered to achieve the convergence within the hybrid method, as it is was assumed from earlier work by [151] to achieve reasonable solutions. The optimisation processes were applied for these iterations using the flow chart of Figure 4.10 of the hybrid method of MoM and FDTD. The antenna was modelled using CST, and it was a half-wavelength dipole directed along the z-axis. The conducting plate used had height $= 0.2385 \, \lambda$ and width $= 0.1073 \, \lambda$ at the centre frequency covering 1 GHz to 4 GHz, modelled by MoM/FDTD precisely as for the verification example of the time-domain MoM/FDTD technique used in [152]. The simulations results are indicated in Figure 4.4 to Figure 4.9. FDTD modelling is beneficial when using a conducting plate as compared to a wire dipole as a scatterer object since there is no need for radius measurement to be modelled. There is the need to make some variations in the separation distance D_c between the antenna and the plate in order to make the input impedance of the bow tie dipole as the target of comparison. The details of the full parameters used for this modelling is given in Tables 4.1.
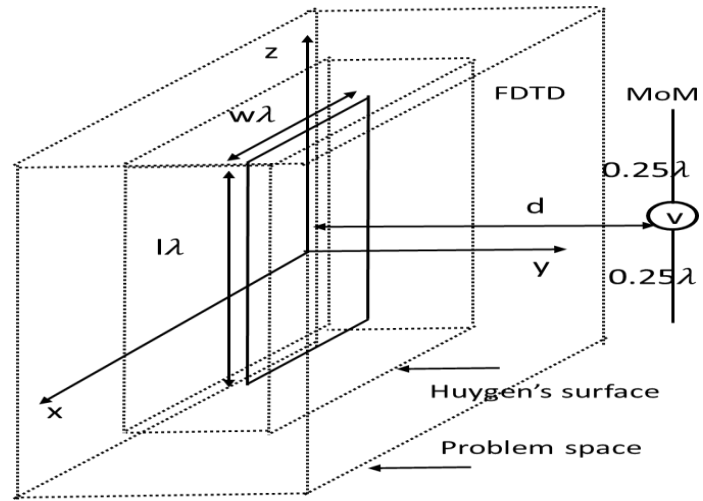
Figure 4.3: The antenna model within the hybrid method.
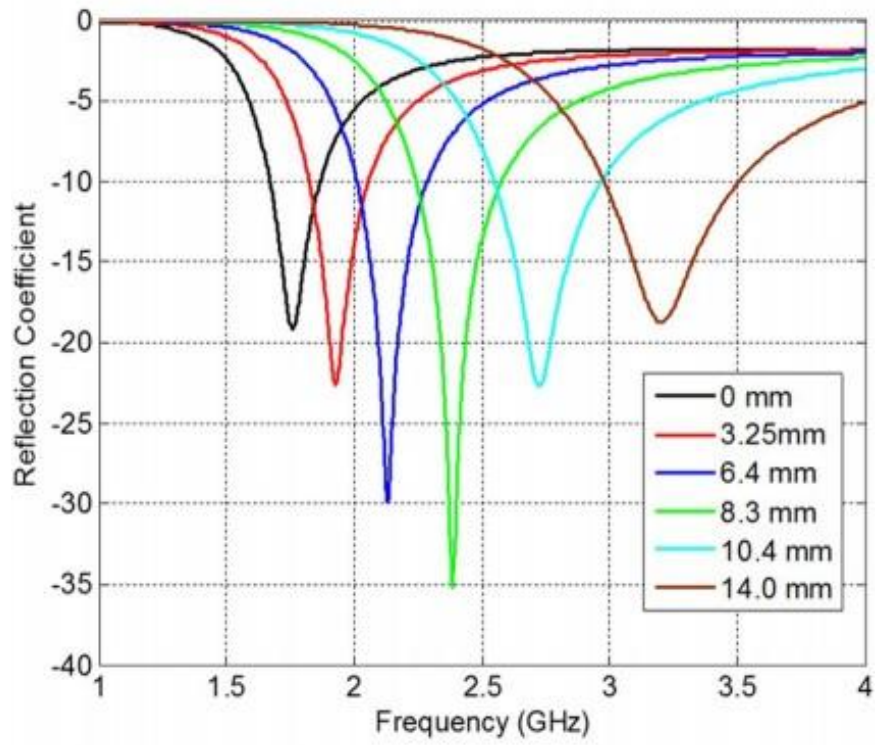
Figure 4.4: Parametrised return loss at a different value of K.
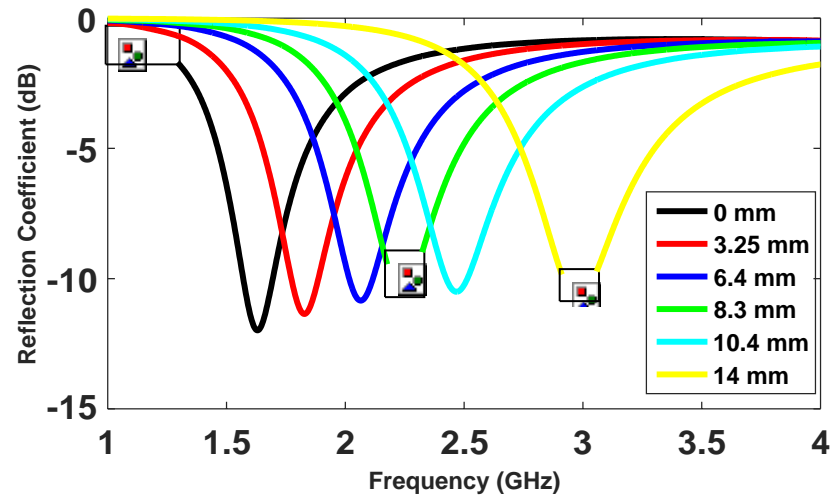
Figure 4.5: Return loss with an improve bandwidth at a different value of K.
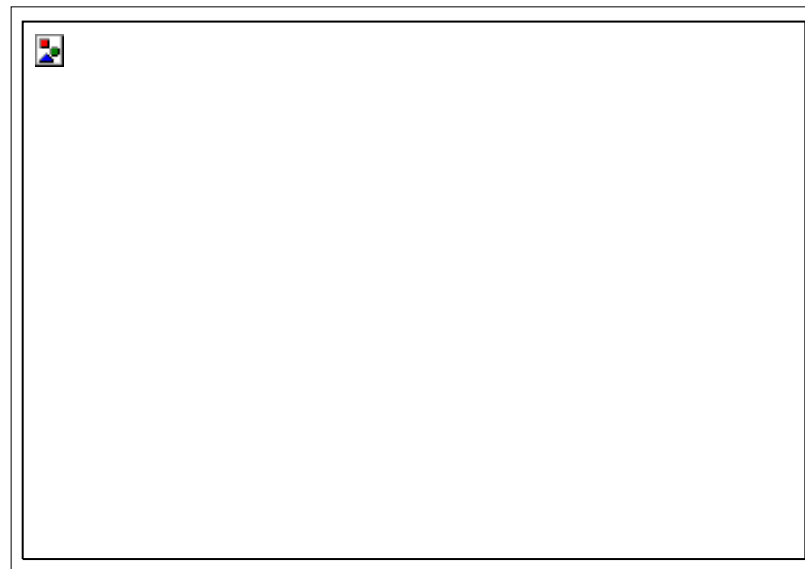
Figure 4.6: Bow-tie antenna radiation pattern at 2.5 GHz for E and H Field.
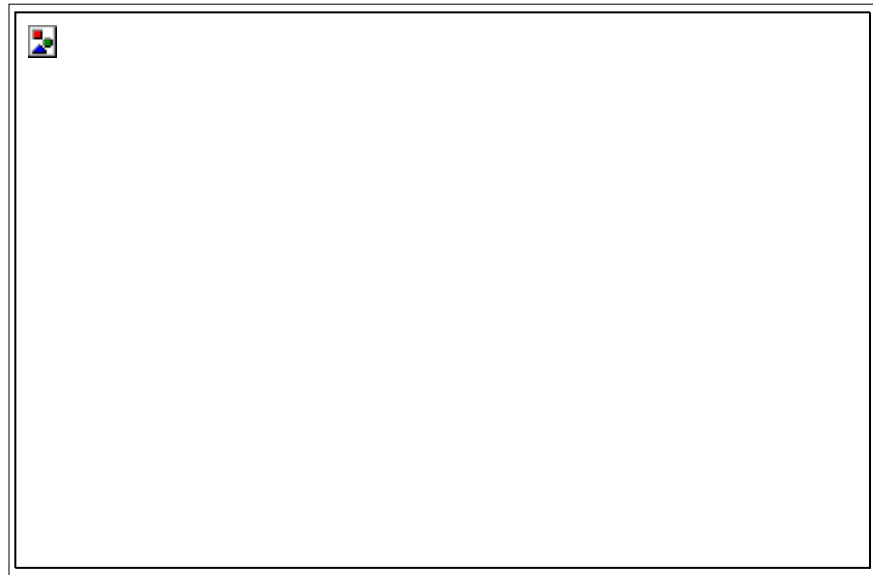
Figure 4.7: Bow-tie antenna radiation pattern at 5 GHz for E and H Field.
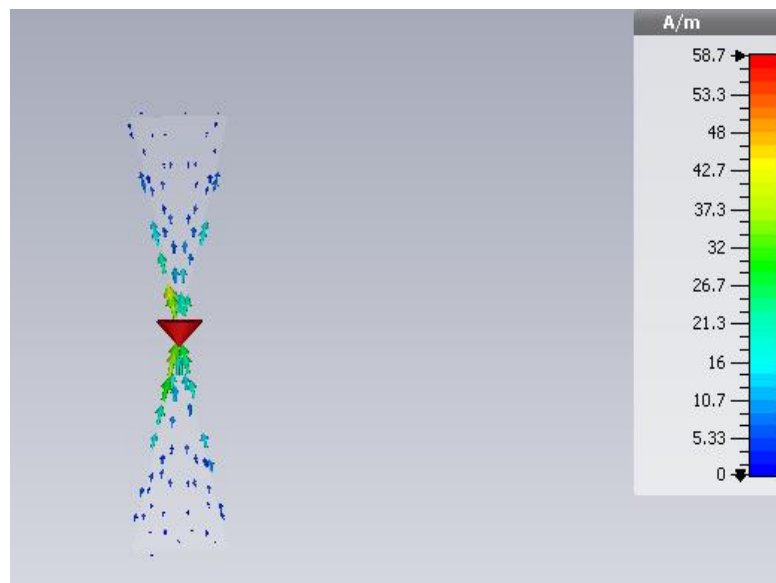
Figure 4.8: The current distribution of the designed Bow-Tie antenna.
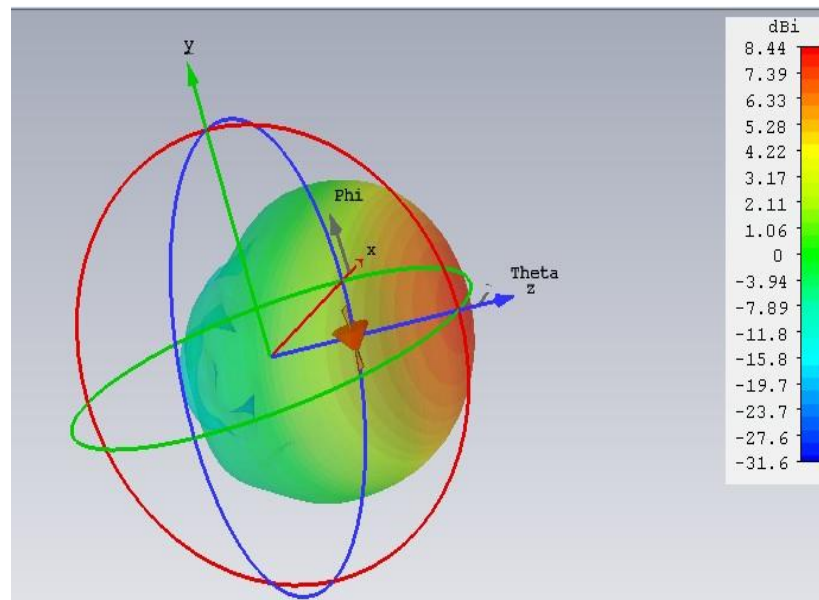
Figure 4.9: 3D far-field radiation pattern of the Bow-Tie antenna.
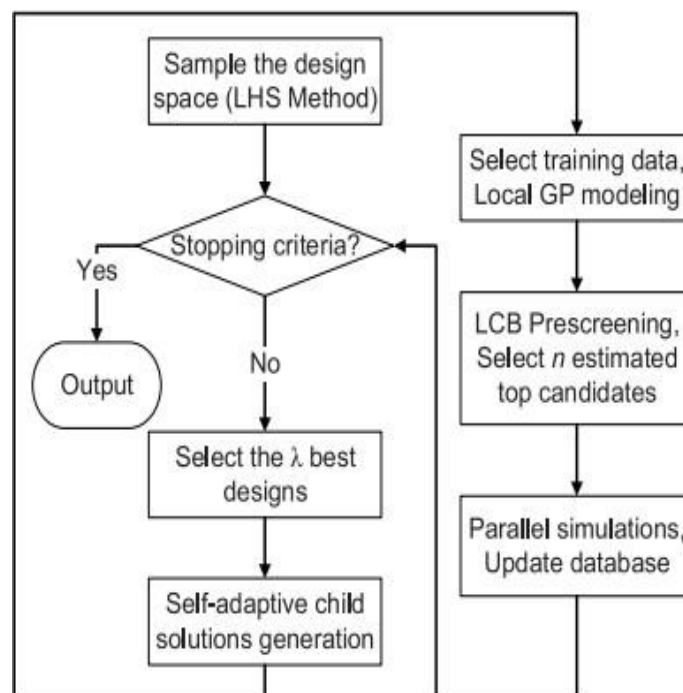
Figure 4.10: Optimisation process using a hybrid method of MoM and FDTD.

Table 4.1: Input modelling of MoM and FDTD parameter.

Formulation	Total/scatter field
Operating Frequencies	1.5,2.5 and 3.5GHz
px, py, pz	58,42,74
mx, my, mz	78,62,94
Total number of FDTD cells	77x63x95 =460845
$nlayer$	8
Δ	0.003
Δt	4ps
Time cycles	25
ax, ay, az	17,17,23
$xmin, xmax$	$nlayer + 6, mx - nlayer - 6$
$ymin, ymax$	$nlayer + 6, my - nlayer - 6$
$zmin, zmax$	$nlayer + 6, mz - nlayer - 6$
Huygens surface size s_0 in mm	176x128x224
MoM: Parameters: Bow tie antenna	
Flare angle: Case 1: 15^0 to 30^0 and to 60.	
Separation distance between the dipole and the dielectric: 10mm,20mm and 30mm.	
Length (d/2) -15mm to 30mm	
The SADEA Algorithm is characterised by the following parameters: Pop Size=40, scale factor=0.8, population diversity =450, no of variables =3 and no of iterations 500.	

4.3   Microstrip Patch Antenna

A microstrip patch antenna is a low profile antenna made of a radiating element of arbitrary shape place on a dielectric substrate. Due to their lightweight, inexpensive nature, and electronics like structure, they can be easily integrated with circuit board technology and usually used in the microwave frequency range [153].

A patch antenna can take a variety of shapes such as rectangular, triangular, circular and elliptical. The rectangular patch antenna is one of the most commonly used microstrip antennas with its basic structure, as shown in Figure 4.11.
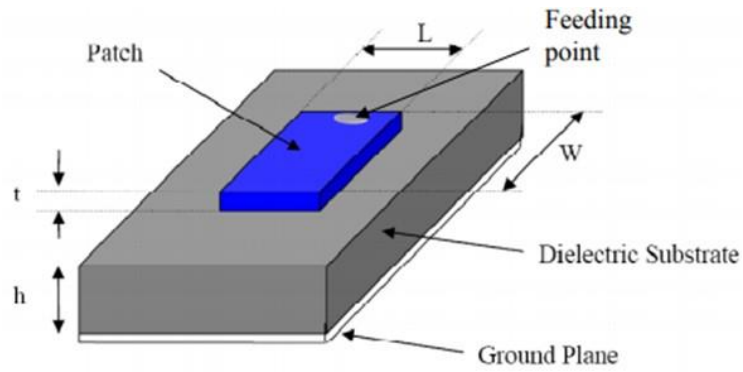
Figure 4.11: Basic structure of a patch antenna [154].

Various forms of feeding techniques including microstrip line, coaxial feed, aperture coupled feed and proximity couple feed is used for the simulation of patch antenna for effective and efficient antenna operations [154, 155]. Mismatched and discontinuities between the antenna elements resulted in high losses which need to be taken into consideration in selecting the best feeding technique. The simplest form of patch antennas feeding technique is the coaxial-feed shown in Figure 4.12, which does not suffer from feed network losses and simple to fabricate [27]. Coaxial feeding element is made of an inner conductor usually surrounded by a dielectric material. The inner conductor is connected to the radiating element while the outer component covered by an insulating material.
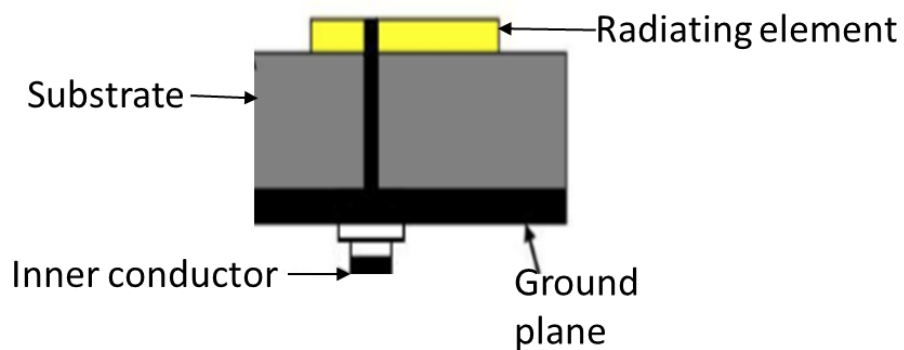
Figure 4.12: Coaxial cable fed patch antenna [154].

Various feeding methods for simulating patch antennas are categorised in

Table 4.2 below [155, 156].

Table 4.2: Categorisation of patch antenna feeding techniques.

Characteristics	Coaxial cable Feed	Microstrip Line Feed	Aperture Couple Feed	Proximity Couple Feed
Impedance Matching	Easy	Easy	Easy	Easy
Spurious Feed radiation	More	More	Less	Minimum
Ease of fabrication	Easy	Easy	Alignment required	Alignment required
Bandwidth relative to impedance matching	2-5%	2-5%	2-5%	13%

In the design of the patch antenna, the resonant length usually controls the resonant frequency, and the patch width determines the bandwidth and the impedance level of the antenna properties. The larger the patch width dimensions, the smaller the input impedance of the antenna simulated on thin substrates normally less than 0.03 λ_0 as considered in [157]. The resonant length should be less than a $\lambda d/2$ owing to the fringing effect. Furthermore, to control the physical size of a patch antenna, the substrate material relative permittivity ε_r and thickness of the PCB need to be taken into consideration [155]. So the general equation for the rectangular patch length (L) is depicted in equation 4.1 below [153, 158] is:

$$L = 0.49\lambda_d = 0.49\frac{\lambda_0}{\sqrt{\varepsilon_r}} \tag{4.1}$$

However, when considering the fringing effect of both edges of the patch antenna, Equation 4.2 is taken into account [154]: where L is the resonant length, λ_d is the wavelength in PC the board, λ_0 is the wavelength in free space, and ε_r is the dielectric constant of the PC board.

$$L = 0.5\frac{\lambda}{\sqrt{\varepsilon_r}} - 2\triangle L \tag{4.2}$$

Where ΔL is the fringing length that can be derived using equation (4.3) and ε_{eff}

is the effective substrate dielectric constant:

$$\triangle L = 0.412\frac{(\varepsilon_{eff} + 0.3)(\frac{W}{t} + 0.264)}{(\varepsilon_{eff} - 0.258)(\frac{w}{t} + 0.8)}t \tag{4.3}$$

Equation 4.4 is usually used to derive the width of the patch antenna.

$$w = \frac{c}{2f_0}\sqrt{\frac{2}{\mathbb{L}_r + 1}} \tag{4.4}$$

4.3.1   A Microstrip Patch Antenna for Medical Applications

In this study, a rectangular patch antenna for body-centric applications is presented and designed to operate in the medical and scientific band of 2.65 GHz. The antenna was designed using CST, having 2.54 mm² thick Rogers RO5880 substrate with a relative permittivity of 3.3 and a copper thickness of 35 μm.

4.3.2   Simulation Results

The centre resonant frequency was simulated at the spectrum of 2.6 GHz. Using Equation 4.2 and Equation 4.4; the patch length and width are calculated to be 19.29 mm² and 18. 98 mm² respectively. The initial return loss is not favourable, as shown in Figure 4.13. The length of the pin position is independently optimised to get better return loss for the patch at 2.65 GHz, as shown in Figure 4.14.
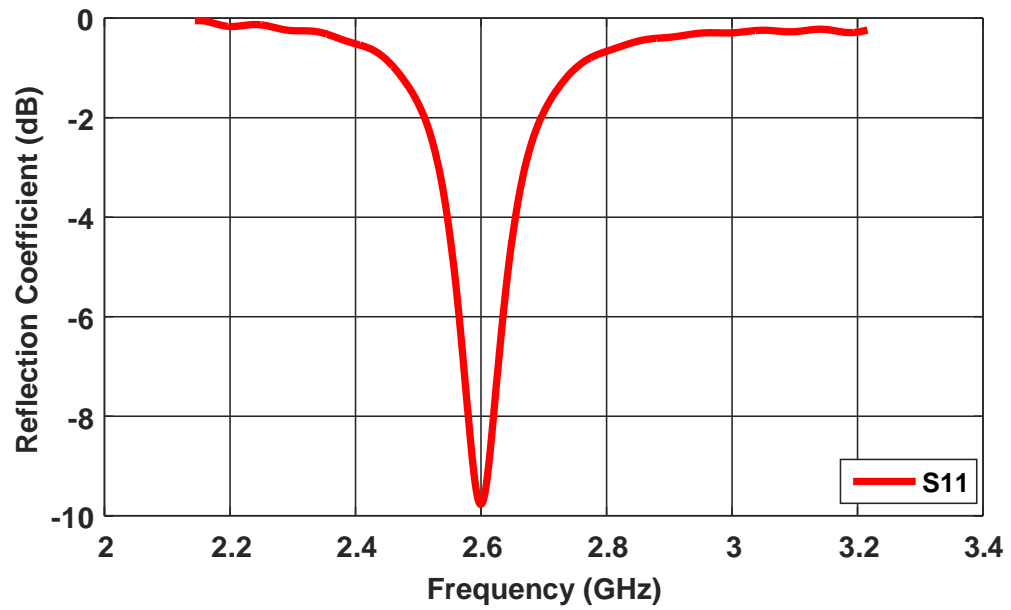
Figure 4.13: The S_{11} of the rectangular patch antenna before optimisation.
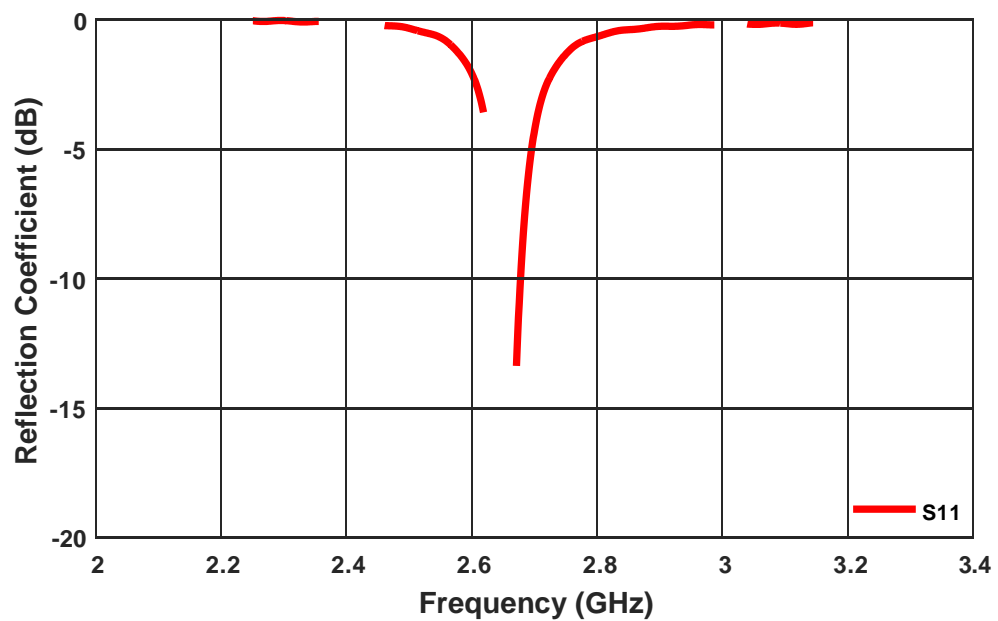
Figure 4.14: The S_{11} of the rectangular patch antenna after optimisation.

The pattern of a rectangular patch antenna is rather broad, with a maximum direction normal to the plane of the antenna and null in directions tangential to the ground plane [159]. On smaller ground planes, the null-depth is reduced. On thicker substrates, the feeding pin may cause spurious cross polarised radiation [160].

The simulated radiation pattern for Φ =0 and 90° is shown in Figure 4.15 and Figure 4.16, respectively. As can be seen from these plots, the radiation pattern is relatively broad in both orthogonal directions. The beamwidth is 80. 7° and 92.1° when Φ = 0 and 90° respectively. The maximum gain is 6.8 dB with the main lobe direction of 0°, and a side lobe level is -11.9 dB. The fabricated antenna is indicated in Figure 4.18. The measured return loss is in good agreement with the simulated results, as shown in figure 4.19. Although the achieved return loss is about 17 dB, which is less compared to the simulation results, that could be due to the fabrication tolerance and soldering of the SMA connector.
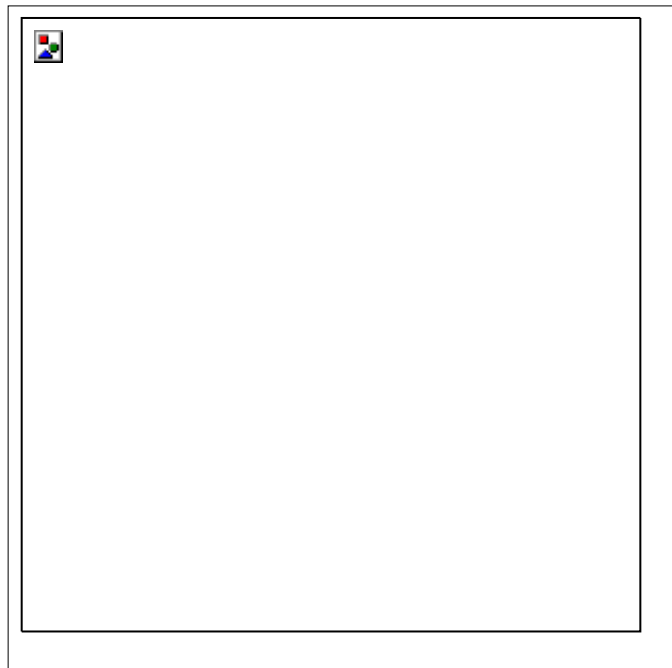
Figure 4.15: Rectangular patch antenna radiation pattern at 2.65 GHz for Φ=0°.
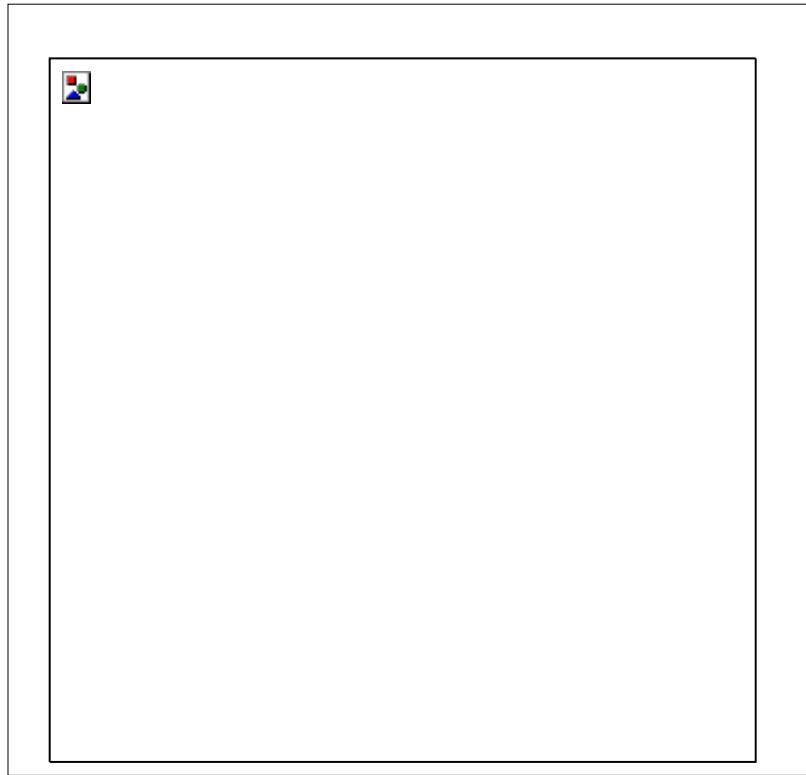
Figure 4.16: Rectangular patch antenna radiation pattern at 2.65 GHz for Φ=90°.

Figure 4.17: The Elevation and Azimutal Plane radiation pattern at 2.65 GHz.
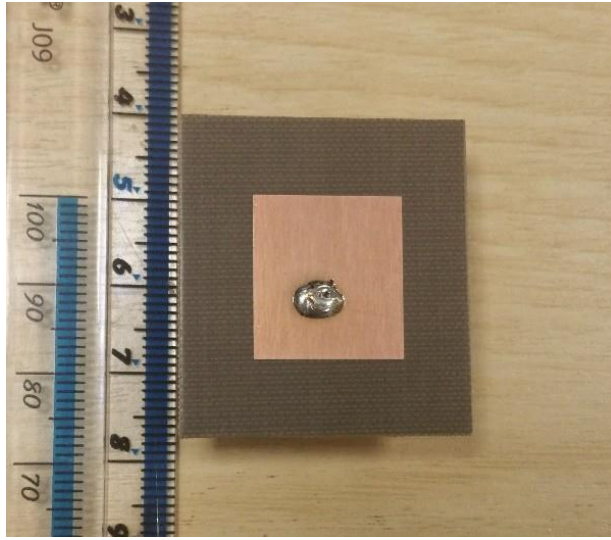
Figure 4.18: The fabricated rectangular patch antenna.
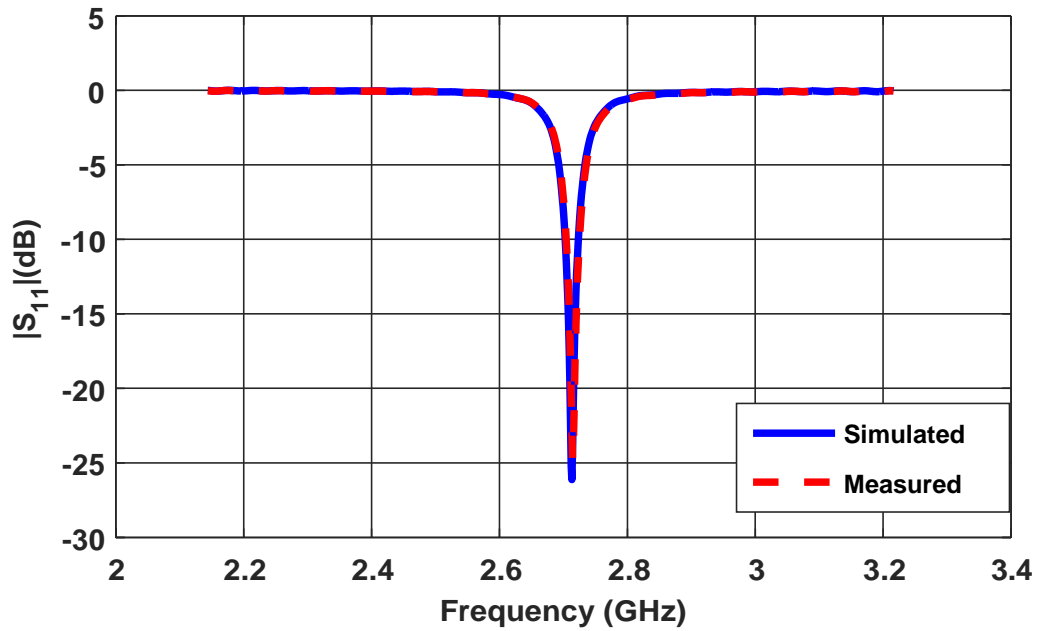
Figure 4.19: The simulated and measured S_{11} of the patch antenna.

4.4   Printed Vivaldi Antenna for Breast Cancer Applications

Vivaldi antenna is a UWB sensor which was originated by Gibson [161] and widely used as radiation elements for UWB arrays applications. The antenna belongs to the class of end-fire travelling wave antennas used in many applications including radar systems [162], wireless communications systems

[163-166], medical imaging [167-169] and through the wall imaging application [11, 170, 171].

Vivaldi antenna is a good candidate for breast cancer microwave imaging application due to its ultra-wideband characteristics, high gain, stable directional radiation pattern, the capability to obtain resonant at a lower frequency, easy fabrication, low profile and end-fire radiation [58]. Additionally, Vivaldi antenna is suited for medical imaging system due to its reconfigurable features, high gain, highly directional and higher efficiency. Numerous types of antenna are developed for microwave imaging such as unit cell antenna, cross-Vivaldi antenna, compact metamaterials antenna and slot antenna [47, 172]. However, Vivaldi antennas also have challenges such as larger sizes and limitation of high losses associated with high-frequency bands [51].

Vivaldi antenna as member of TSA radiators requires slot line feeding approach for its effective performance. As a result, a transition is needed to couple the signals to the slot line of the Vivaldi from the transmitter or receiver circuitry. The transition should be compact, easy to fabricate and with low loss over the entire frequency range so as not to limit the bandwidth of operation. Vivaldi antenna has various feeding techniques which can be classified as either directly coupled transition or transition, which is electromagnetically coupled. In the direct-coupled feeding, Coaxial to slot line transition is the most successful directly coupled feeding transition where a wire or soldering connection is required to provide a direct current path for the electrical connections. Alternatively, in the electromagnetically coupled transition, Electromagnetic fields are used in coupling the signal to the slot line in order to excite the antenna. Frequent electromagnetically coupled transitions are microstrip to slot line, strip line to slot

line, antipodal slot line and balanced antipodal slot line. The typical characteristics of a Vivaldi antenna are indicated inTable 4.3:

Table 4.3: Typical characteristics of a Vivaldi antenna.

Quantity	Typical	Minimum	Maximum
Polarisation	Linear	-	-
Radiation pattern	End-fire	-	-
Gain	4 dBi	2 dBi	17 dBi
Performance bandwidth	3:1	-	6:1
Complexity	Medium	-	-
Impedance	100Ω	50Ω	200Ω
Balun	Not required	-	-

The 3-D plot radiation properties of Vivaldi antenna are determined by a set exponential curve, Cavity diameter, tapered rate, back wall offset, the edge offset, feeding position and slot width. The exponential curve of the Vivaldi antenna is defined as:

$$X = C_1 + e^{RZ} + \ C_2 \qquad (4.5),$$

Where, C_1 and C_2 are in equations 4.6 and 4.7 respectively.

$$C_1 = \frac{x_2 - x_1}{\left(e^{RZ_2} - e^{RZ_1}\right)} \qquad (4.6)$$

$$C_2 = \frac{x_1 e^{RZ_2} - x_2 e^{RZ_1}}{\left(e^{RZ_2} - e^{RZ_1}\right)} \qquad (4.7)$$

4.4.1 *Design of a Taper Slot Low Profile Vivaldi Antenna*

In this study, the design of a tapered slot low profile Vivaldi antenna for ultra-wideband microwave breast cancer imaging applications was presented. The discussion was also carried out on the experimental characterisation of the antenna in proximity to the breast phantom. The performance indicators of the antenna, including its return loss, gain, and radiation patterns characteristics were also analysed. The proposed antenna was designed to provide optimise wide-band performance in the UWB range of 1 GHz to 4 GHz. The antenna also exhibits high immunity and stable radiation pattern in proximity to the breast tissue. The antenna geometry and design process will be following this section.

4.4.2 *Antenna Geometry and Design Guidelines*

Antenna design is one of the main challenges in the modelling, analysis and design of microwave imaging system for medical diagnostics. The main challenge is to be able to design an effective and efficient compact antenna with high sensitivity, low loss and stable radiation pattern over the whole frequency band. The layout geometry in Figure 4.20 and prototype in Figure 4.21 of the proposed antenna shows the antenna dimensions as 62.8 mm x 36mm fabricated on Rogers RT/ Druid 5870 substrates with dielectric constants of 2.33 and loss tangent of 0.0012. UWB antenna designs on low frequencies are more desirable for medical detection to guarantee the deep penetration of the signal inside the breast tissue. Additionally, the use of low frequency would guarantee an improve resolution and reduction of losses associated with high microwave bands. In this analysis, the proposed antenna would be operating at a low-frequency range covering 1GHz - 4 GHz. Following the design guidelines and principles of an

effective and efficient UWB antenna in [173, 174], and improved UWB Taper Slot

Low Profile Vivaldi antenna is designed and tested for the imaging scenarios.
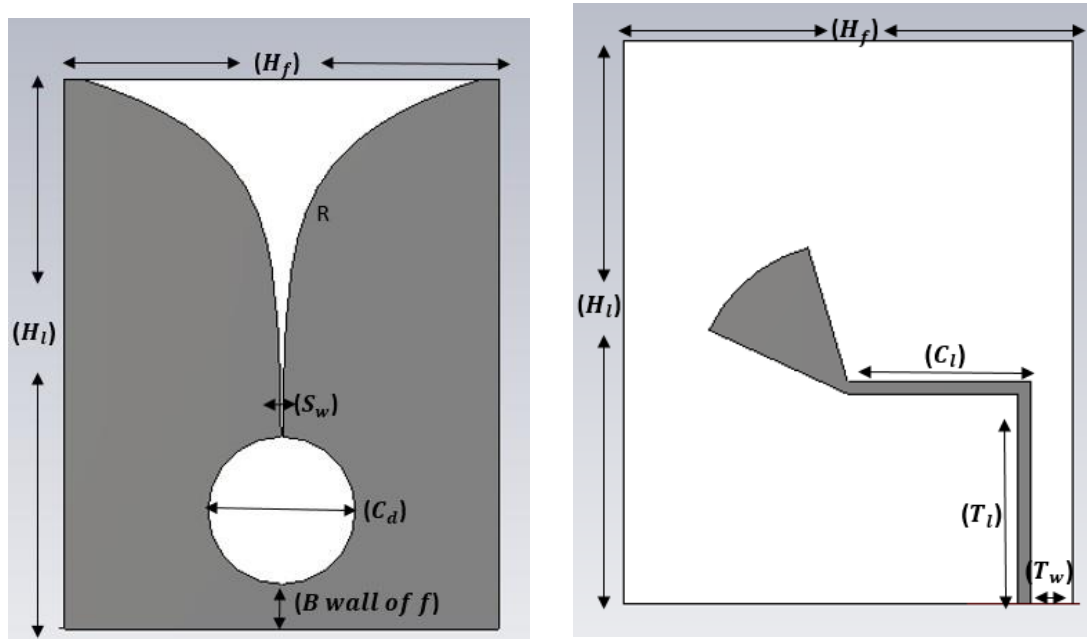
Figure 4.20: Geometry of the designed Vivaldi antenna: left (top view), right

(bottom view). All dimensions in mm.
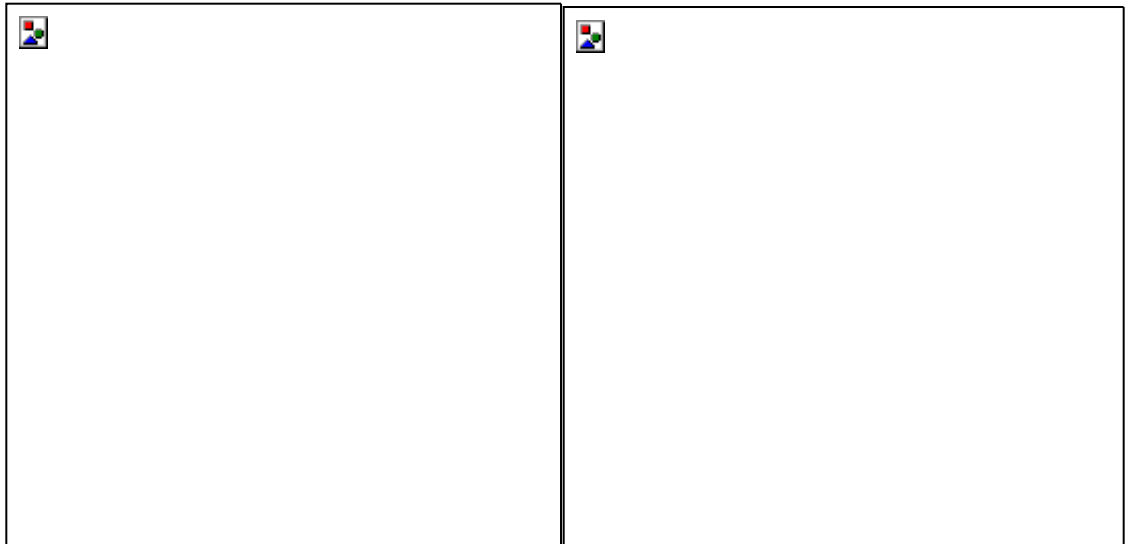
Figure 4.21: Prototype of the designed Vivaldi antenna: left (top view), right

(bottom view). All dimensions in mm.

Table 4.4: Designed Vivaldi antenna parameters.

Constructional Parameters	Dimensions in mm
Flare Height (H_f)	35.00
Flare Length (L_f)	65.80
Taper Rate (T_r)	1.1
Slot Width (S_w)	0.5
Back wall offset ($B\ wall\ of\ f$)	1
Strip Line Width (SL_w)	2.5
Strip Line Length (SL_l)	27.5
Stub angle (φ)	90
Cavity diameter (R)	9
Cavity distance (C_l)	3.3
Taper Width (T_w)	2.5
Taper Length (T_l)	16.2
Coupler Width (C_w)	1.5
Coupler Length (C_l)	11.9

Table 4.5: Substrate details used for the design.

Substrate Parameters	Values
Name	Rogers RT 5880
Relative permittivity	2.2
Electrical Conductivity	0.0009
Substrate Height	65 mm
Substrate width	36 mm
Substrate thickness	2.82 mm
Copper Height	0.035 mm

Table 4.6: Homogeneous Dry Concrete Wall Electrical Properties.

Wall	Dimension
Thickness	150 mm
Length	150 mm
Breath	150 mm
Relative Permittivity	7.5
Equivalent Conductivity	0.5

4.4.3   Antenna Performance Analysis

The proposed antenna has been analysed using CST microwave studio. The main goal and objective of the design are to measure and analyse the scattered electromagnetic waves due to the transmitted UWB microwave signal penetrating through the medium containing the wall. The evaluation of the antenna design analysis was carried out by examining its reflection coefficient (S_{11}) and envelope correlation. These are essential parameters of the overall antenna system design

as they take into account the mutual coupling effect of the system. The -10 dB impedance bandwidth of the proposed antenna is 1.8 GHz – 4.2 GHz, as indicated in Figure 4.22. The Return loss of the antenna parameter is affected by the stub angle, substrate type and the cavity diameter while the antenna gain is affected by the stub radius.

A parametric simulation of the proposed antenna was carried out using the parameters in Table 4.5. The prototypes of the fabricated antenna are indicated in Figure 4.21. Different antenna parameters were considered at the operating bandwidths which are required to obtain the desired gain. Relevant parameters, including the antenna size, feeding position, slot width, substrate type, and the microstrip line size, were also measured. To check the influence of these parameters on the impedance bandwidth, parameters were varied one after the other during the parameterisation task. The simulation result indicates the effect of these parameters variation on the resonant frequency and the return loss, as indicated in Figure 4.22 and Figure 4.23, respectively.
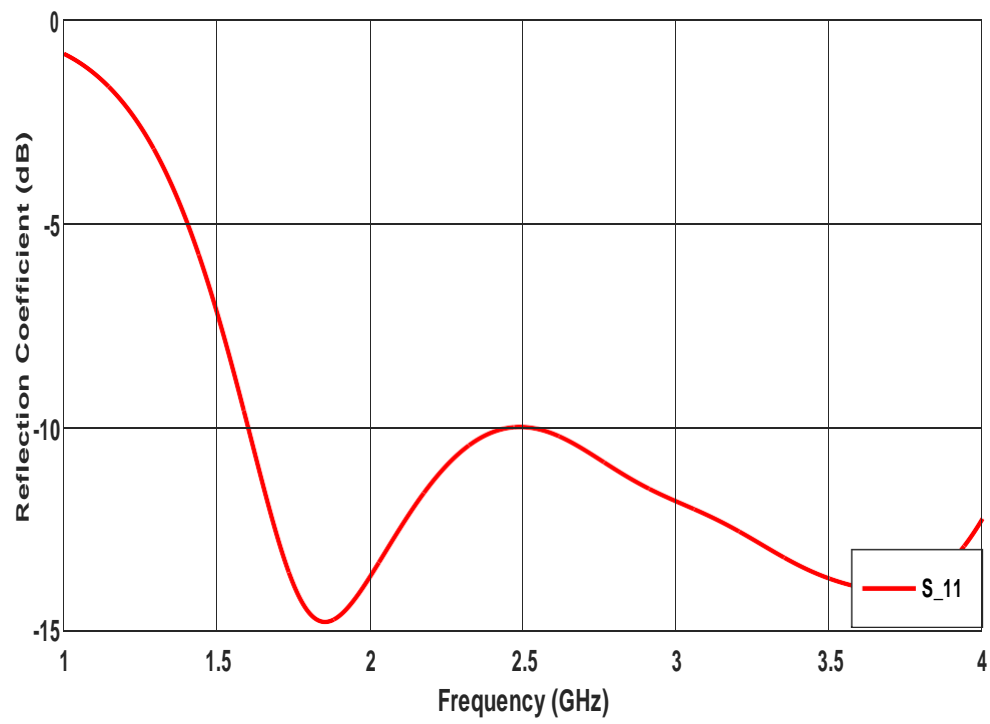
Figure 4.22: Simulated S_{11} of the Vivaldi antenna.
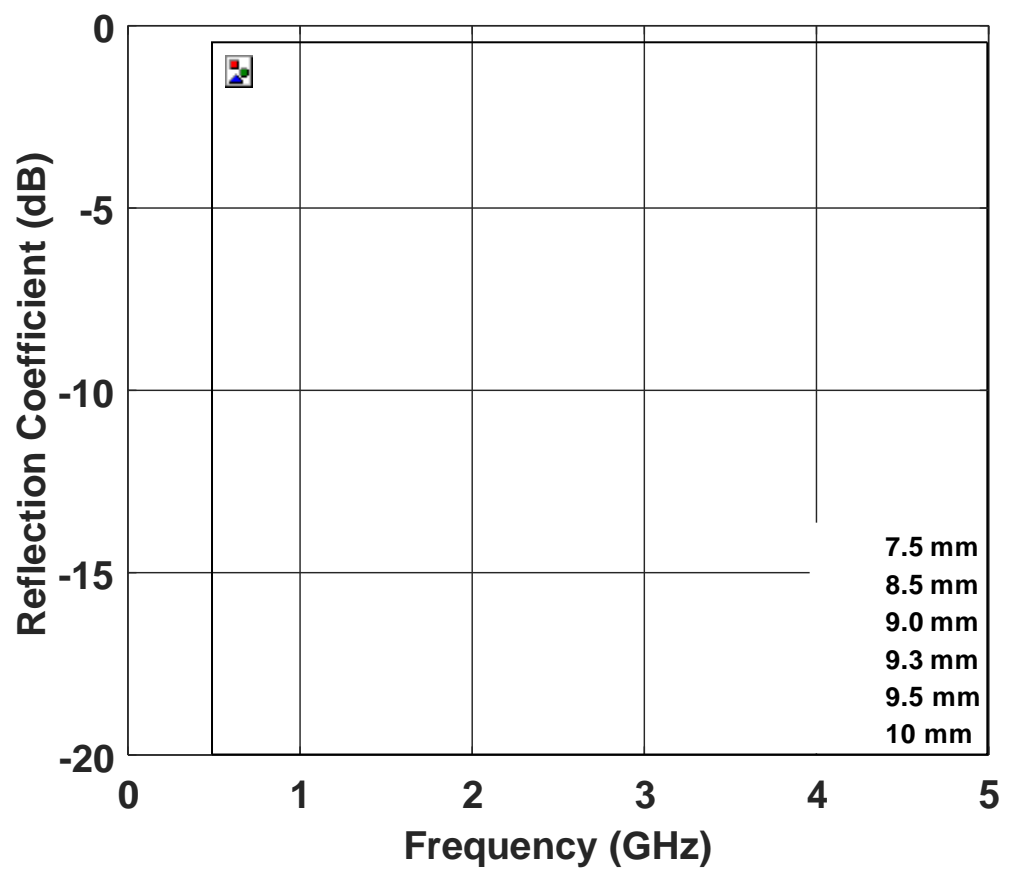
Figure 4.23: Effects of the Stud radius to the S_{11} of the Vivaldi antenna.
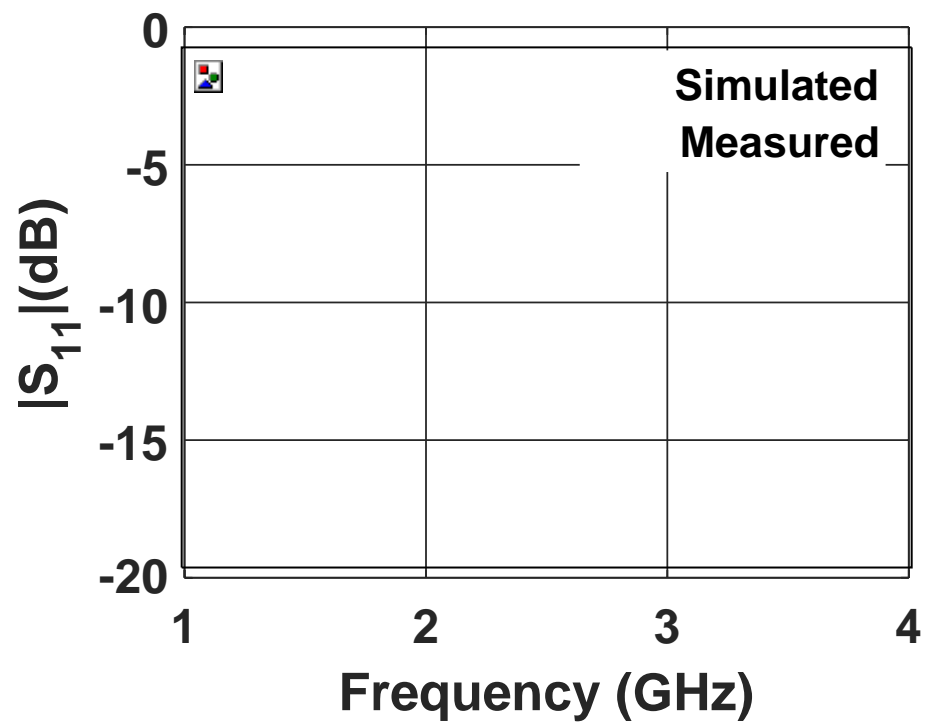
Figure 4.24: The simulated and measured S_{11} of the Vivaldi antenna.
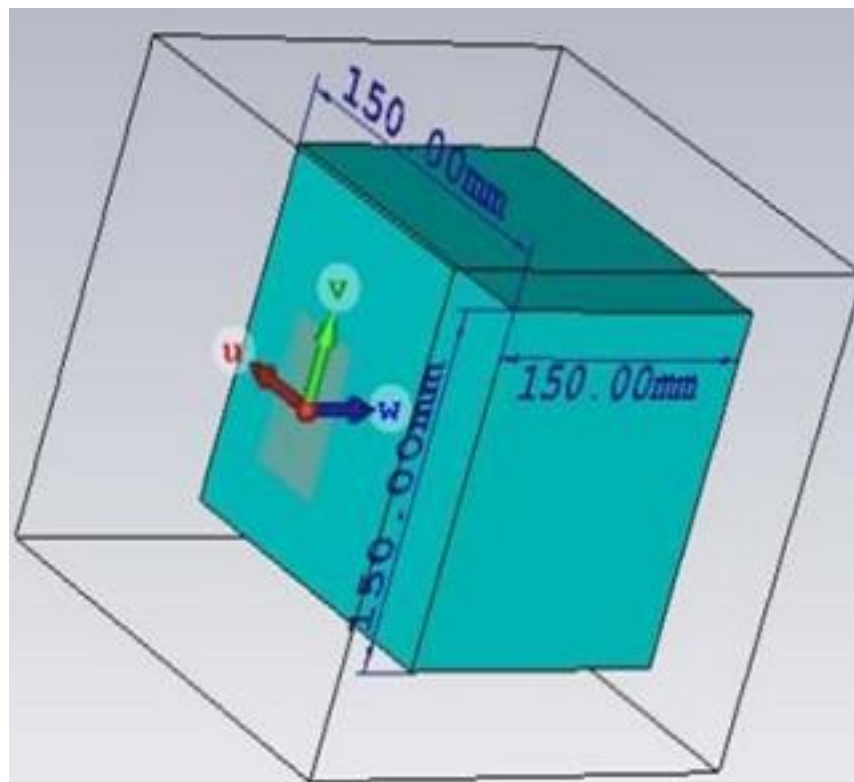
Figure 4.25: Geometry model of the proposed antenna with the wall.
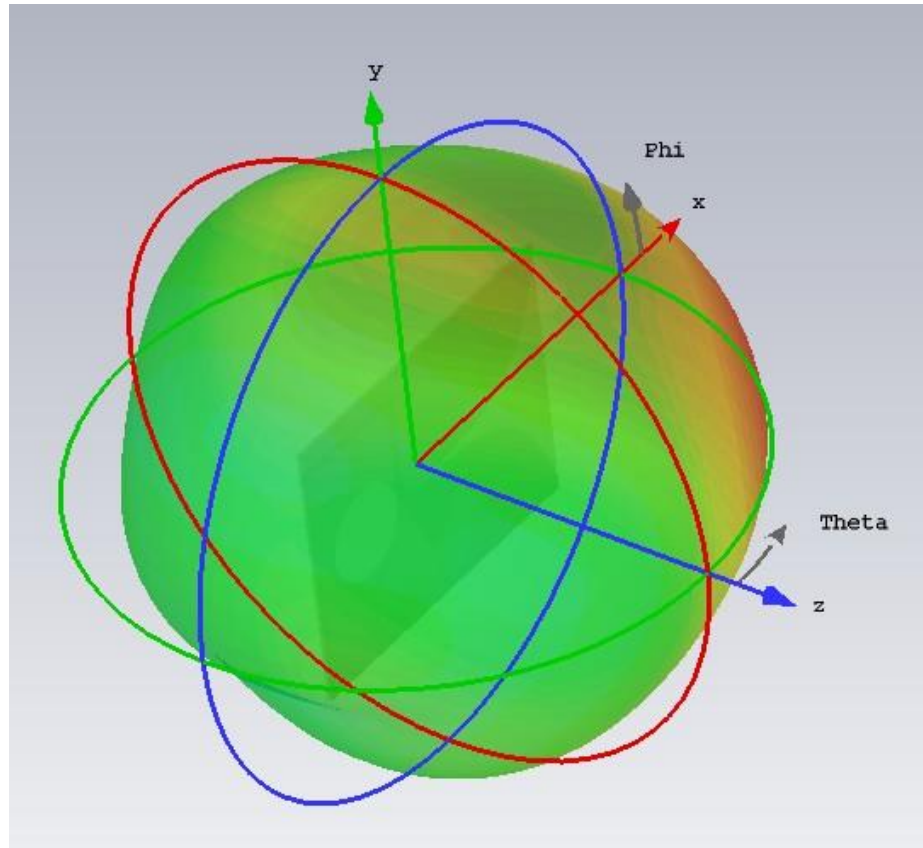
Figure 4.26: 3D far-field radiation pattern of the Vivaldi antenna.

The simulated and measured return loss are in good agreement, as indicated in Figure 4.24. This indicates that the antenna is robust to fabrication tolerance. The 3D far-field radiation pattern of the proposed antenna is shown in Figure 4.26.

The simulated radiation pattern for Φ =0 and 90° is shown in Figure 4.27 and Figure 4.28, respectively. The elevation and azimuthal Plane radiation pattern at the centre frequency of 2.5 GHz are shown in Figure 4.29. The beamwidth is 67. 7° and 78.1° when Φ = 0 and 90° respectively. The maximum gain is 6.8 dB with the main lobe direction of 0°, and a side lobe level is -5.9 dB.
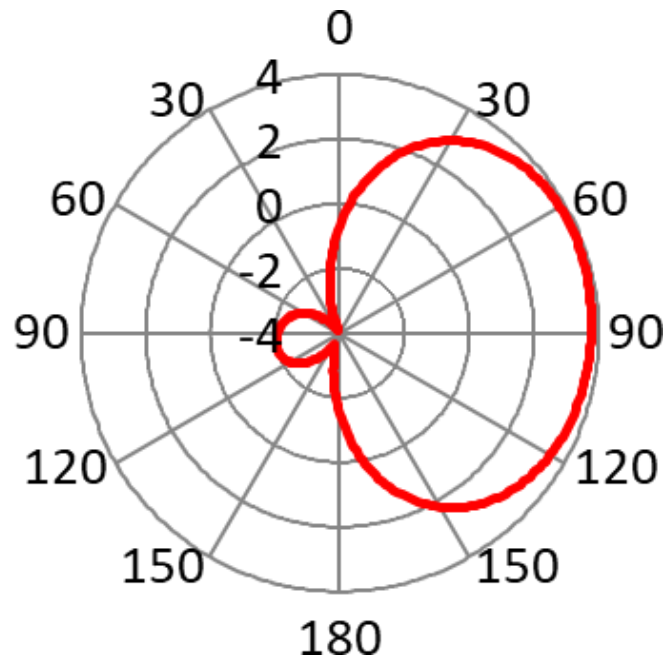
Figure 4.27: Measured radiation pattern for the fabricated Vivaldi antenna for
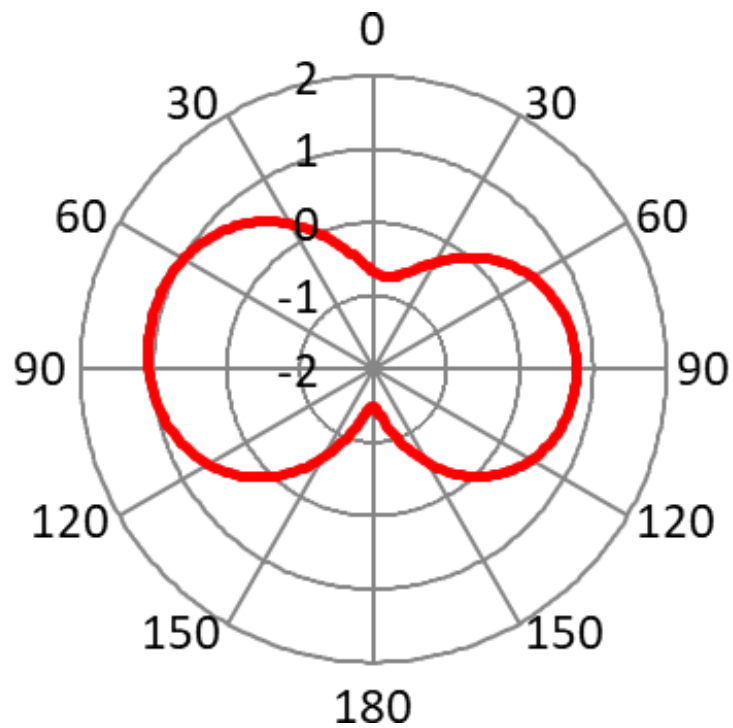
Φ=0° cutting plane.

Figure 4.28: Measured radiation pattern for the fabricated Vivaldi antenna for

Φ=90° cutting plane.
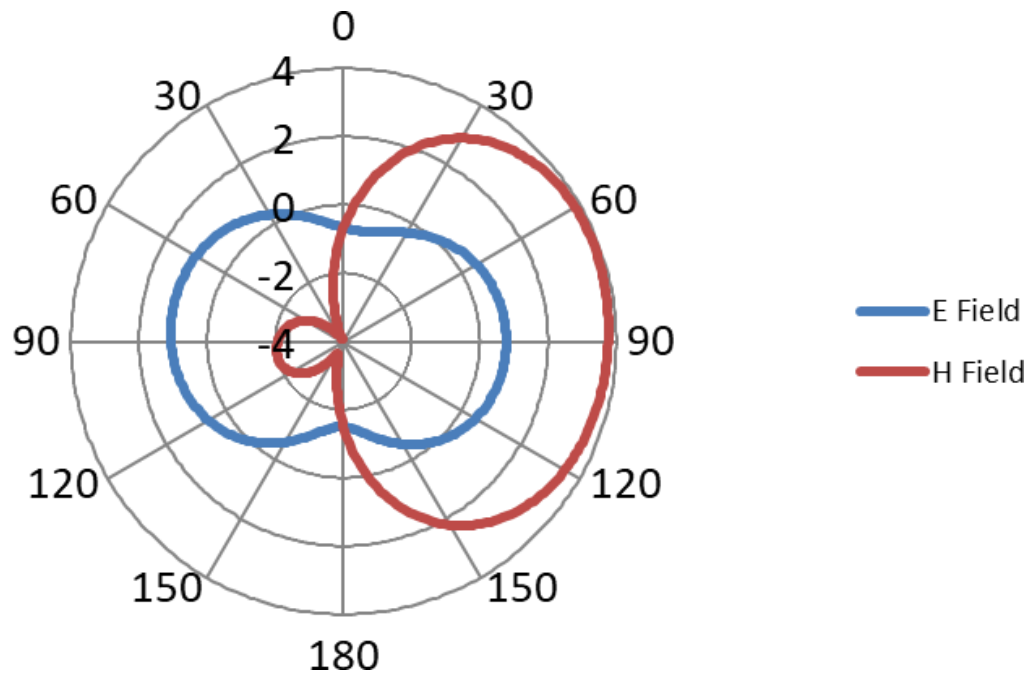
Figure 4.29: The Elevation and Azimutal Plane radiation pattern at 2.5 GHz.

4.5 Conclusion

This chapter presents the various practical antenna design including bow-tie, microstrip patch and Vivaldi antenna, particularly for microwave imaging applications. In this chapter, the antenna geometry with their complete design guidelines, including the antennas performance analysis, were all highlighted. Additionally, parametrisation and optimisation of the various antennas were also carried out in this chapter.

Chapter 5

Monopoles Antenna for Microwave Imaging Applications

5.1   Introduction

This section highlighted various monopoles antenna designed for microwave imaging applications. The monopole antenna in Figure 5.1, results from applying the image theory to the dipole. According to this theory, if a conducting plane is placed below a single element of length L/2 carrying a current, then the combination of the element and its image acts identically to a dipole of length L except that the radiation occurs only in the space above the plane [175].
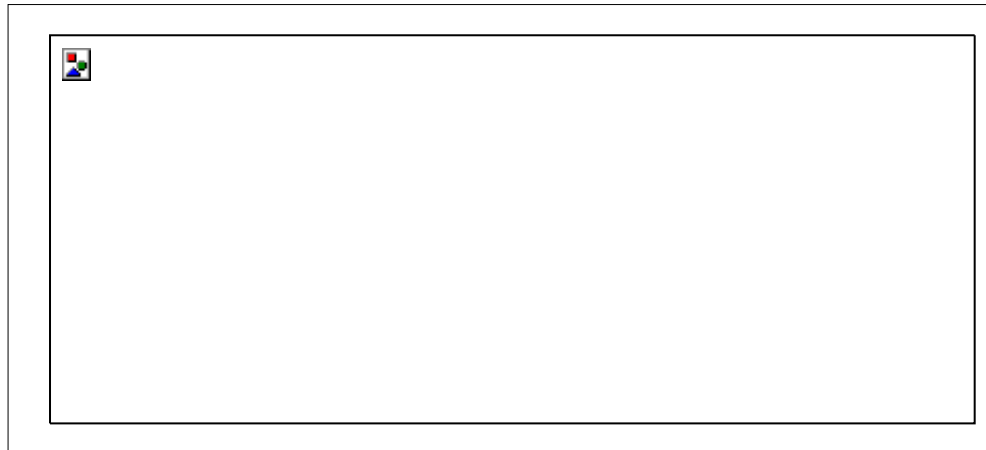
Figure 5.1: Monopole Antenna [24].

Monopole antenna has directivity doubled, and its radiation resistance halved when compared to the dipole. Thus, a half-wave dipole can be approximated by a quarter-wave monopole (L /2 = λ/4). The typical gain for the quarter wavelength monopole is 2- 6dB, and it has a bandwidth of about 10%. Its radiation resistance is 36.5Ω, and its directivity is 3.28 (5.16dB).

As printed monopoles antenna offer relatively ultra-wideband spectrum and radiation patterns similar to dipole antennas, as well as simple structure and low fabrication cost, in this study, various configurations of printed monopole antenna including T-slot, rectangular slot and Hexagonal slot monopoles antennas were considered for microwave imaging applications.

5.2   A T Slot Monopole Antenna for Microwave Imaging Applications

This Section considered the design, optimisation and physical implementation of a compact ultra-wideband (UWB) printed circular monopole antenna (PCMA) for microwave imaging applications, specifically for breast cancer detection. The profile of the proposed antenna features T-Slots etching over a driven circular patch. To achieve the desired impedance bandwidth both in free-space and in proximity to human tissues, the geometrical profiles of the T — slot monopole antenna is optimised using the surrogate model-assisted differential evolution for antenna synthesis (SADEA) optimiser. The bandwidth, gain, radiation pattern and efficiency of the optimised antenna are all analysed and evaluated. The simulation and measurement results of the antenna's responses are in reasonable agreement for the input impedance, gain, radiation pattern and efficiency, respectively, in the operating band of 3.1 GHz to 10.6 GHz. The proposed antenna also gives adequate radiation in the broadside direction, which contributes significantly to clutter level reduction, and makes the proposed antenna applicable for effective and efficient microwave imaging applications.

5.2.1   Antenna Geometry and Design Guidelines

The layout of the printed circular monopole antenna (PCMA) is shown in

Figure 5.2. The PCMA consists of a driven circular patch having four uniform T

slots and is implemented on an FR-4 substrate having a thickness 0.8 mm^2, relative permittivity (ε_r) of 4.3 and a loss tangent (tanδ) of 0.025. The PCMA features two uniform rectangular planes acting as a partial ground. The feeding of the PCMA is via a 50 Ω coaxial cable and a microstrip line.

Minimise max|S11| over 3.1 GHz to 10.6 GHz   (5.1)
Subject to: GR ≥ 2 dB

Figure 5.2: Geometry of the designed Monopole Antenna.

5.2.2 Antenna Performance Analysis

An initial parametric study of the PCMA was achieved with CST-MWS to determine the possible search ranges of the design variables. The physical dimensions considered for the parametric study of the PCMA include substrate's length (Ls) and width (Ws), the ground plane's length (Gl) and width (Gw), the radius of the driven circular patch (R) and the microstrip feedline's length (Fl) and width (Fw) at a fixed copper layer thickness of 0.035 mm^2. The width of throat and depth of head for all the T-slots are equal; the depth of throat and width of the head for all the T-slots are equal; thus, all the dimensions of the T slots are uniform and relative to R as shown in Figure 5.2. The PCMA is optimised using SADEA in ADE 1.0 using the recommended settings in [176]. The design exploration goal is to minimise to the maximum reflection coefficient (S_{11}) in the

operating band of 3.1 GHz to 10.6 GHz subject to the realised gain (GR) not being less than 2 dB over the bandwidth as shown in Equation 5.1. The selected values of the design variables for the proposed PCMA after the parametric study and design exploration are shown in Table 5.1.

Table 5.1: Designed T Slot Monopole antenna parameters.

Antenna Parameters	Dimension
Substrate Length	41.50 mm
Substrate Width	26.20 mm
Circle Radius	12. 50 mm
Ground Length	15.57 mm
Ground Width	12. 10 mm
Feeding Length	15. 84 mm
Feeding Width	1.47 mm

Table 5.2: Designed T Slot Monopole substrate parameters.

Substrate Parameters	Values
Name	Fr-4 Substrate
Relative permittivity	4.3
Electrical Conductivity	0.025
Substrate Height	41.50 mm
Substrate width	26.20 mm
Substrate thickness	0.8 mm
Copper Height	0.035 mm
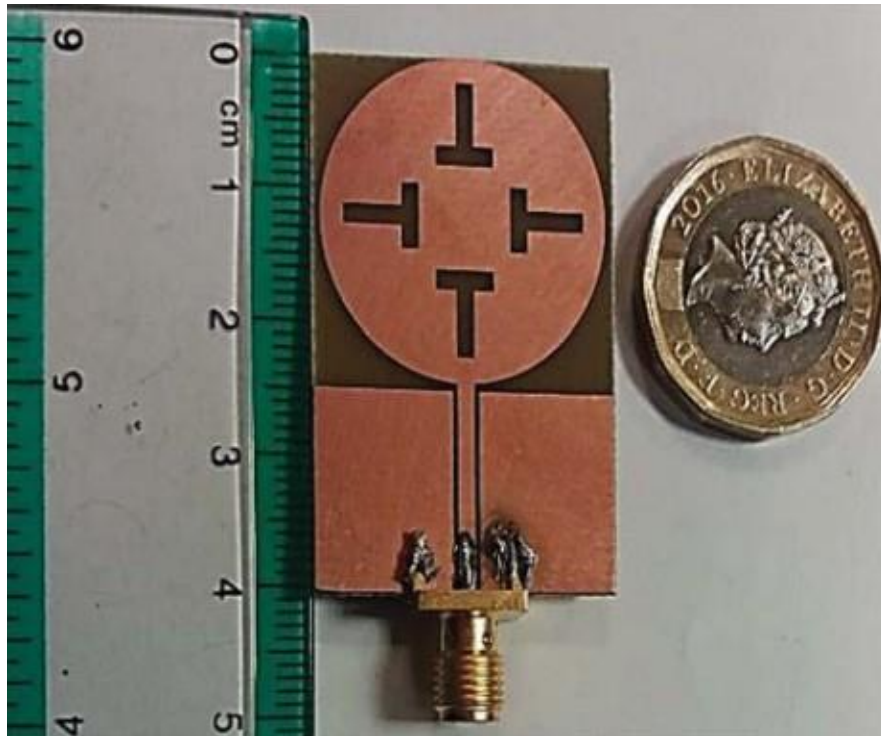
Figure 5.3: Prototype of the designed Monopole Antenna.

A low profile, compact and durable design is realised for the proposed PCMA, and the physical implementation is shown in Figure 5.3. To evaluate the efficiency and performance of the proposed PCMA, the simulated and measured results for the return loss over the operating bandwidth (3.1 GHz to 10.6 GHz) are indicated in Figure 5.4, and the normalised and unnormalised Eθ and Eφ far-field characteristics are shown for two planes (x- z and y-z planes) at two selected frequencies in the operating bandwidth (6 GHz and 9 GHz) in Figure 5.5a and Figure 5. 5b. The proposed PCMA also satisfies the requirement in equation 5.1 for the realised gain (GR) at a minimum value of 2.3 dB in the operating bandwidth (3.1 GHz to 10.6 GHz). Specifically, GR > 4.5 dB is achieved in the broadside direction. Using the standard -10 dB reference for the evaluation of the return loss, Figure 5.4 shows that the proposed PCMA achieves a good impedance bandwidth in the operating bandwidth, and the measured and simulated results are in reasonable agreement. Figure 5.4 also shows that the PCMA is multi-

resonant with sharp resonances at frequencies, which include, but are not limited to 3.66 GHz, 3.8 GHz, 4.6GHz, 7.76 GHz and 8.5 GHz for the measured results. These resonances are expected due to their inducement by the uniform T-slots etched on the driven circular patch. Figure 5.5a and Figure 5.5b shows that the proposed PCMA has sufficient radiation (over 4.5 dB) in the broadside.
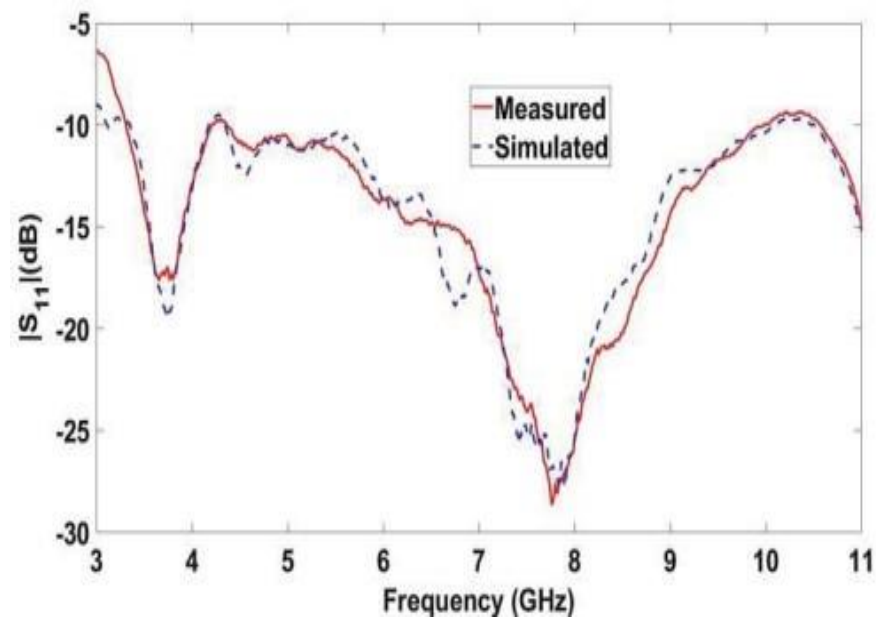
Figure 5.4: The simulated and measured S_{11} of the Monopole antenna.
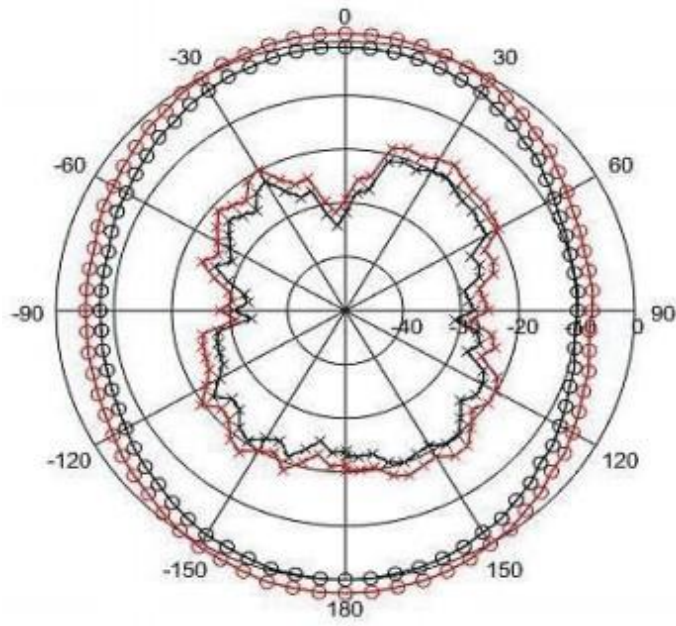
(a) 6 GHz
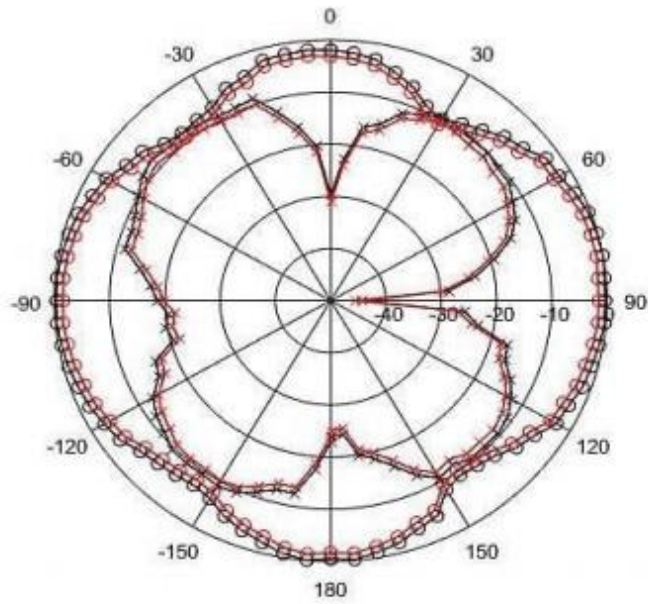
(b) 9 GHz

Figure 5.5: Normalised and un-normalised Eθ and Eφ field characteristics (x-z and y-z planes) of the proposed PCMA; Black curve: Normalized, Red: Un-normalized.

5.3 A Rectangular Slot Monopole Antenna for Microwave Imaging Applications

As discussed earlier, numerous types of monopoles antenna with ultra-wide impedance bandwidth have been proposed for on-body and microwave imaging applications [177]. Monopole antennas are compact, simple structure, ease of fabrication and suitable for low-cost physical implementation [178]. They also offer a good radiation pattern and wide frequency impedance bandwidth [179]. They are also easy to construct and implement from simulation to practical experiment [154]. These characteristics and other features make monopole antennas good candidates for body-centric imaging applications. Different configuration of Monopole antennas, including rectangular, square, triangular, circular, semi-circular, hexagonal, ellipse, are used for practical UWB applications, as shown in Figure 5.6 [177, 180].

| | | | |
| (a) | (b) | (c) | (d) |

| | | | |
| (e) | (f) | (g) | (h) |
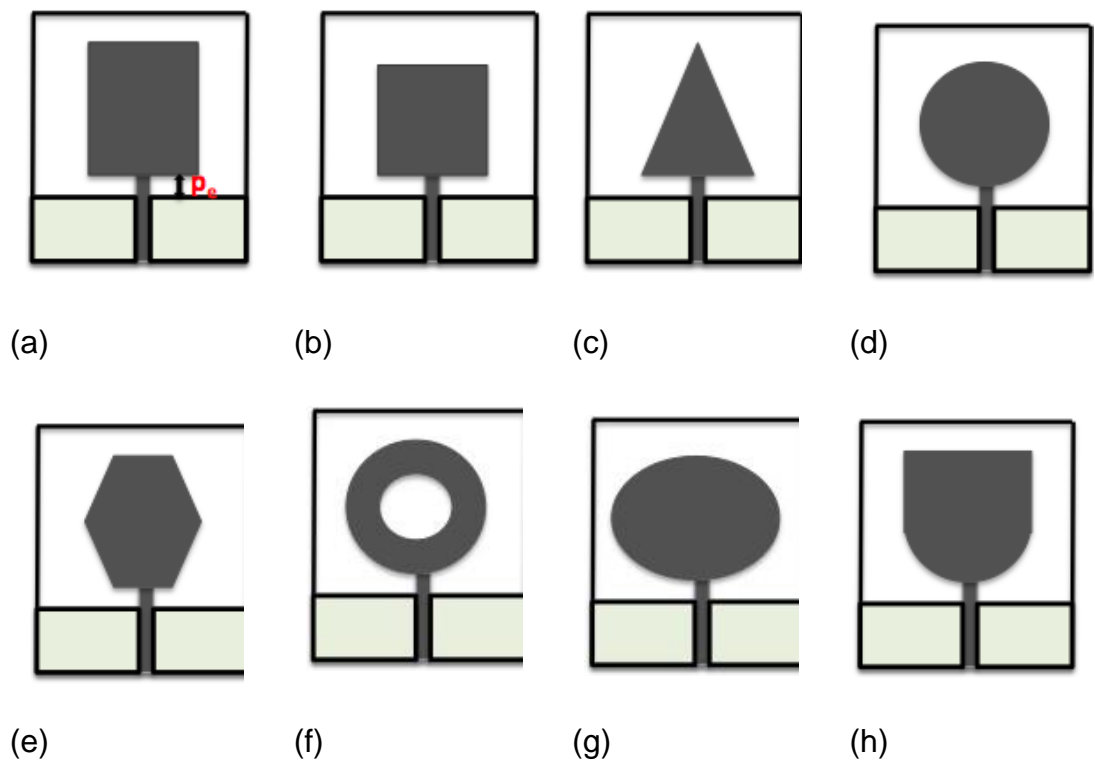
Figure 5.6: Different Configurations of Monopole antenna [177].

This work presents the design, optimisation and analysis of a printed monopole UWB antenna with a rectangular-slot for on-body and breast cancer microwave imaging applications. The experimental characterisation of the antenna in proximity to the human body and breast mimicking tissues (phantom) was also carried out. Also, other performance parameters of the antenna, including its return loss, radiation patterns and time-domain characteristics with more emphasis on fidelity and impulse response were all considered. Additionally, the specific absorption rate of the antenna was also analysed.

The proposed antenna is designed with the aid of computer simulation technology microwave studio software (CST-MWS) and optimised using the surrogate model-assisted hybrid differential evolution for antenna optimisation algorithm (SADEA). The antenna is implemented on an FR-4 substrate and analysed in terms of bandwidth, gain, efficiency, and radiation pattern. The antenna fidelity factor is also analysed to characterise the UWB antenna time-domain operation. All measured results are found to be in good agreement with the simulated results. The antenna provides an excellent return loss in the UWB frequencies of 3.1 GHz to 10.6 GHz and maintains its bandwidth UWB operation without detuning when placed in closed contact with the human body or breast mimicking tissues (phantoms).

The design and optimisation of the proposed antenna present the following as a new case in point:

- Experimental paradigm for the design exploration of slotted monopole antennas considering the use of fused T-slots on the driven element to

improve the impedance bandwidth and control the surface current distribution in a predefined frequency spectrum, in this case, 3.1 GHz to 10.6 GHz;

- The real-world use case for the novel surrogate model-assisted hybrid differential evolution for antenna optimisation algorithm (SADEA) considering a constrained optimisation problem with multiple geometric constraints.

- Highly compact design and physical implementation of a slotted monopole antenna for a real-world application with over 1.6 times area reduction compared to similar designs [181, 182];

The experimental paradigm and the efficiency of the SADEA [183, 184] are all validated by the proposed antenna which provides excellent characterisation in terms of bandwidth, gain, efficiency while showing a high immunity to fabrication tolerances.

.

5.3.1 *Proposed Antenna Geometry and Design*

The layout of the primitive design of the proposed antenna is shown in Figure 5.7, and the performance requirements are given in Table 5.3. The proposed antenna consists of a driven circular patch of radius, DP_R. Furthermore, four T-slots, which are fused at the centre of the driven circular patch to form a quasi-cross slot. The proposed antenna is fed by a 50 Ω coaxial microstrip line with dimensions, M_L by M_W. It has two uniforms rectangular planes with dimensions, RP_L by RP_W, which are abreast and separated by the microstrip line. The uniform rectangular planes act as a partial ground and are both truncated. The truncation of the ground plane is primarily to enhance the input impedance of the proposed antenna. The

uniform gap width, M_G between the surface, partial ground planes and the microstrip line chiefly keeps the characteristic impedance of microstrip line constant The proposed antenna is modelled and simulated in CST-MWS using the time domain finite integration technique (FIT) method with an accuracy of -40 dB, a maximum cell density of 20 cells per wavelength and a total of about 300,000 hexahedral mesh cells. It is implemented on the FR-4 substrate having a thickness of 0.8 mm^2, tangential loss ($\tan \delta$) of 0.025 and a relative permittivity (ε_r) of 4.3. Several techniques have been proposed for the control of the surface current distribution in UWB antennas [185-187]. Amongst these techniques, slot etching on the radiating patch has been well demonstrated to be both practical and efficient [188-190].
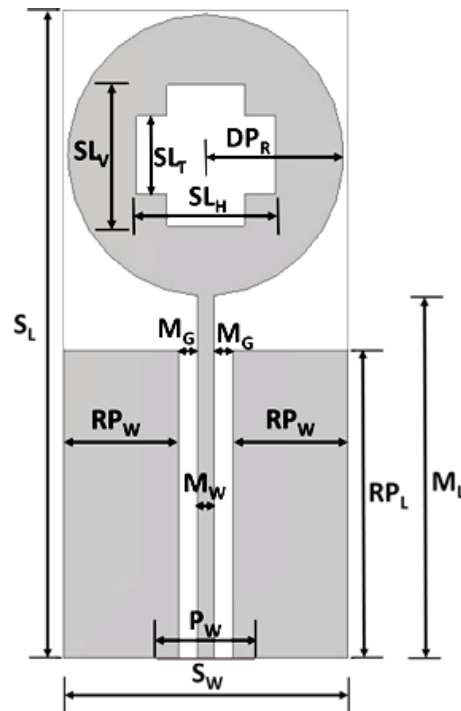
Figure 5.7: Layout of the proposed slotted planar monopole antenna.

Table 5.3: Performance specification for the Slot Monopole antenna.

Parameter	Specification	Description
Desired Spectrum	3.1 GHz-10.6 GHz	UWB Spectrum
Return Loss (S_{11})	< -10 dB	UWB Spectrum
Boresight gain (G_B)	1 dBi < G_B < 5 dBi	UWB Spectrum

Table 5.4: Dimensions specification for the Slot Monopole antenna.

Parameter	Dimensions
Substrate width (S_W)	14.90 mm
Substrate length (S_L)	33.12 mm
Substrate thickness	0.8 mm
Microstrip length (M_L)	18.52 mm
Microstrip width (M_W)	0.84 mm
Microstrip gap (M_G)	0.12 mm
Circular patch radius (DP_R)	7.21 mm
Width of slot throat (SL_T)	5.98 mm
Vertical slots' depth (SL_V)	12.06 mm
Horizontal slots' depth (SL_H)	5.98 mm
Partial ground plane width (RP_W)	6.91 mm
Port width (P_W)	5.13 mm

Table 5.5: Breast Tissue Electrical Properties.

Layers	Skin	Breast
Thickness	2	100
Relative Permittivity	36	9
Equivalent Conductivity	4	0.4

The slots on the radiating patch change the current path and; thus, generates higher-order current modes. This development resulted in significant changes in the antenna characteristics, which leads to a reduction in the side.

At high frequencies on planar antennas, the current flow tends to follow curvy paths rather than straight paths and become distributed. The current density then becomes largest on the planar surface due to skin effects. If a slot is etched on the radiating patch, that is the current surface by convention, and the current flow will follow the curvature of the slot. As a result, the geometry of the slot affects the surface current distribution, as shown in Figure 5.8. The radiation of the antenna can then be controlled by controlling the path of the surface current [191].
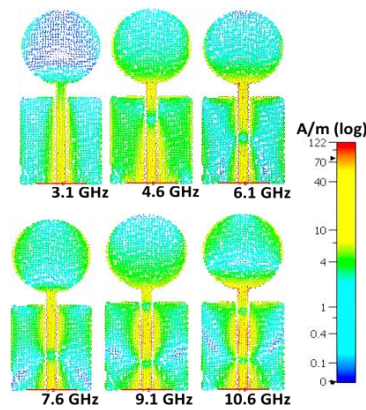
(a) Without etching or slot.
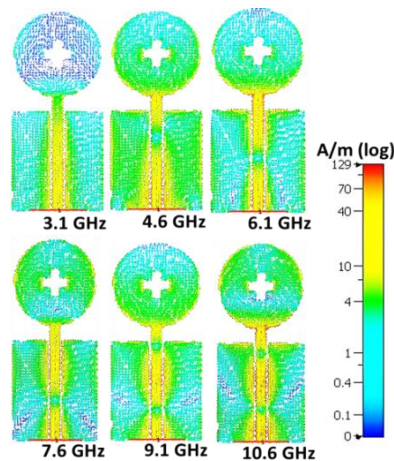
(b) With etching or slot.

Figure 5.8: Surface current densities of the primitive design of the proposed antenna.
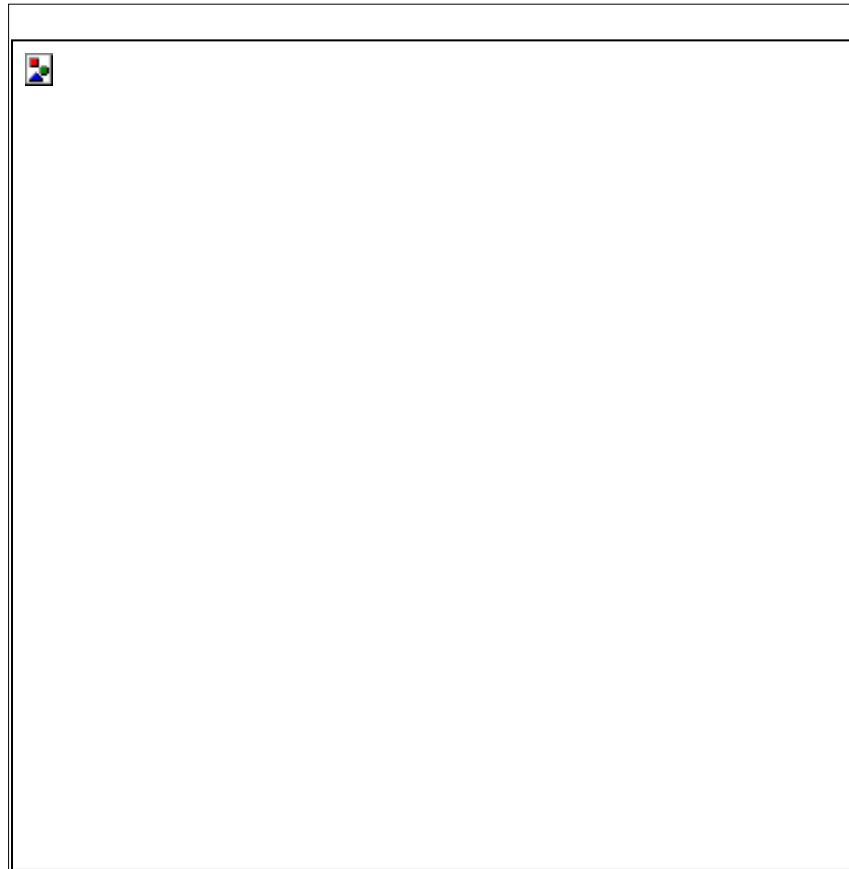
Figure 5.9: Physical implementation of the proposed slotted planar monopole antenna.

The primary purpose of the quasi-cross slot feature is to enhance the monopole's performance over the UWB spectrum by controlling the surface current distribution path. The dimensions of the etching in the slots can be estimated by examining the surface current distribution of the antenna as illustrated in Figure 5.8 for a slot configuration and six frequency samples, 3.1 GHz, 4.6 GHz, 6.1 GHz, 7.6 GHz, 9.1 GHz, and 10.6 GHz, respectively, within the UWB spectrum. However, this is time costly and may become prohibitive if a large number, slot configurations and frequency samples are to be considered. To allow for a reasonable degree of freedom in the configuration of the etching for the proposed antenna, the quasi-cross slot is parameterised for easy transitioning from the quasi-cross configuration to rectangular configuration by using two control

parameters to vary its dimensions. This enables a mechanical design of the etching based on optimisation, as discussed in the next section.

The first control parameter (SL_H) for the determination of the configuration of the etching is obtained by making the equal width of the heads of the two horizontally placed T-slots to constitute the equal depth of the throats and the equal depth of the heads of the two vertically placed T-slots (see Figure 5.7). The second control parameter (SL_V) is obtained similarly by making the equal width of the heads of the two vertically placed T-slots to constitute the equal depth of the throats and the equal depth of the heads of the two horizontally placed T-slots (see Figure 5.7). By varying the dimensions of SL_H and SL_V, the configuration of the etching can transition seamlessly between quasi-cross slot and rectangular slot (x-dominant or y-dominant: see equation (5.2). To ensure that the etching is always formed inside the driven patch in all possible cases of transitioning, a uniform width of throat (SL_T) is specified for all the four T-slots (see Figure. 5.7). The overall dimensions of the proposed antenna are $33.12 \ mm^2 \times 14.90 \ mm^2 \times \ 0.8 \ mm^2$, which are less than those of similar designs [181], [182]. The compact design is obtained by optimising the antenna using SADEA [184], and the optimisation process is discussed in the next section. The optimised dimensions of the antenna are shown in Table 5.4, and the physical implementation is shown in Figure 5.9.

5.3.2 *Optimisation Using SADEA*

Antenna design optimisation methods can be broadly grouped into local and global optimisation methods. Local optimisation methods require a reasonably high-quality initial design to obtain reasonable design solutions, while global

optimisation methods often require a considerable number (in some cases prohibitive) amount of EM simulations to obtain good designs [192]. To address the drawbacks of local and global optimisation methods, surrogate model-assisted optimisation methods are necessitated due to their added efficiency improvement, robustness, high-quality design solutions free of an initial design requirement [193, 194].

SADEA [184, 195] is employed for the optimisation of the proposed antenna. SADEA [194, 196] algorithm, which are purpose-built methods offering around 3 to 20 times efficiency improvement for the surrogate model-assisted global optimisation of antenna designs. Gaussian process surrogate modelling, differential evolution search and the surrogate model-aware evolutionary search framework [196] are the critical elements in the SADEA algorithm.

For the synthesis of the proposed antenna, SADEA is used to minimise the fitness function, F_{mpa} in (5.2), to satisfy the specifications in Table 5.3.

$$F_{mpa} = \max\left(S_{11}\right) + w \times \max\left([2\ dBi - G_{min}]\right) + \dots w \times \max\left([G_{max} - 5\ dBi]\right) \qquad (5.2)$$

Where w is the penalty coefficient, and it is set to 50. By setting w to be equal to 50, the specifications for the bore-sight gain (i.e., G_{min} and G_{max}) are satisfied first by largely penalising F_{mpa} if they are violated. Then, meeting the S_{11} the requirement becomes the primary focus of the optimisation procedure as soon as G_{min} and G_{max} are satisfied.

The design parameters and their search range considered for the optimisation are given in Table 5.3. It can be seen that the search ranges are large (i.e., without ad-hoc selection). The geometric constraints considered to avoid

geometric incongruities as far as possible during the optimisation are also shown in Table 5.4. After 2.5 days of optimisation on an Intel i7-8700 CPU with 3.2 GHz CPU and 32 GB RAM, SADEA obtains the optimum design in Table 5.3 and the performance results for this design are shown in Table 5.4. From Table 5.4, it can be seen that SADE obtains a design that satisfies all the specifications. Hence, the optimisation ability and efficiency of SADEA is demonstrated. Note that CST-MWS optimisers (Trust Region Framework and Particle Swarm Optimisation [194]) failed to meet the specifications in Table 5.3 for several independent runs of the proposed antenna's optimisation that cost over 20 days each. The fabricated SADEA synthesised antenna is shown in Figure 5.9, and the overall dimensions are 33.14 mm^2 × 14.90 mm^2 × 0.8 mm^2, which is compact and 1.6 times smaller than a similar-state-of-the-art design [185]. The simulation and measurement results for the free space return loss are shown in Figure 5.10. From Figure 5.10, it can be seen that the simulation results are in close agreement with the measurement results. The microwave imaging application test and measurement results using the fabricated antenna are discussed in the next section.

5.3.3 Tests, Measurements and Results

A. Free Space Return Loss

The proposed antenna was experimentally characterised by an Agilent technologies N5242A vector network analyser (VNA) for comparing the simulated and measured results in free space. To study the antenna operation in free space, the comparative investigation was carried out between the simulated (using CST) and measured reflection coefficient S_{11} with the VNA. The antenna S_{11} was calculated between 3 GHz and 11 GHz, as this was the UWB range of interest covering the spectrum of 3.1 GHz to 10.6 GHz. The free space simulated and

measured results agree very well up to 10.8 GHz, with some differences arising around the second resonance, which is not as strong and narrow for the experimental measurement as for our simulation. These slight differences in the return loss curves can be attributed to fabrication inaccuracies.
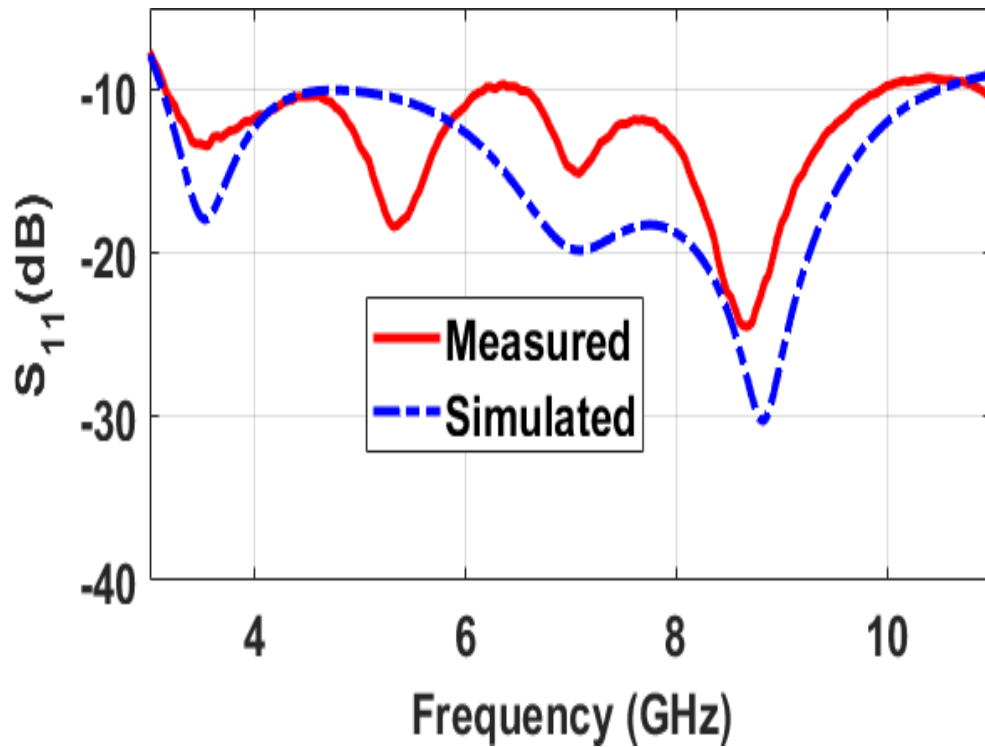
Figure 5.10: Proposed antenna free space simulated and measured results.
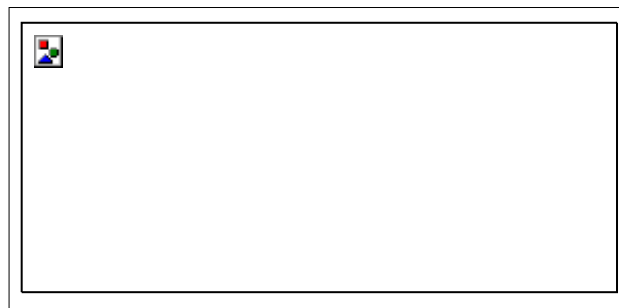
Figure 5.11: Proposed antenna with the phantom body model.
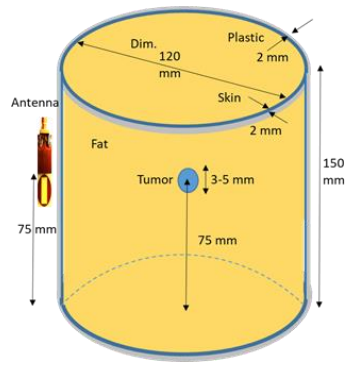
Figure 5.12: Breast tissue model with the antenna element
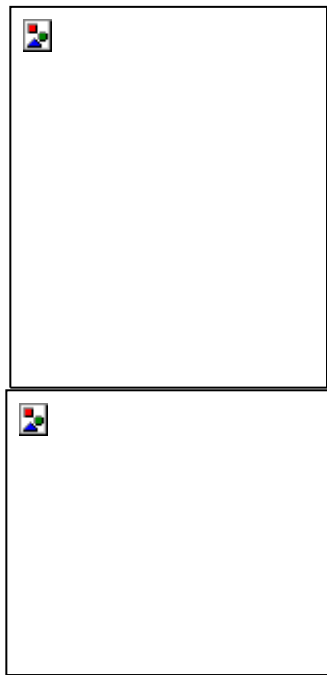
(a) One spherical cancer model (top), prototype (bottom).
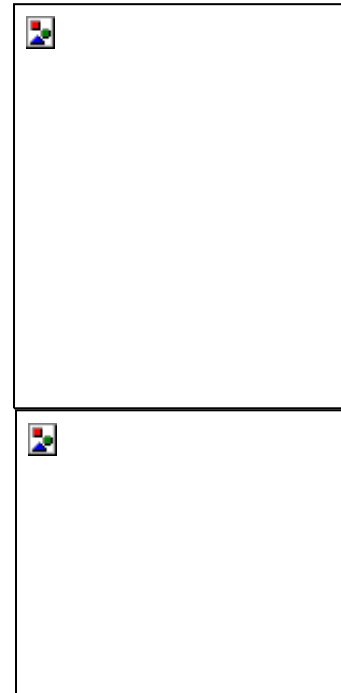
(b) Two spherical cancer model (top), prototype (bottom).

Figure 5.13: Proposed antenna placed in the closed distance to the breast mimicking phantom.
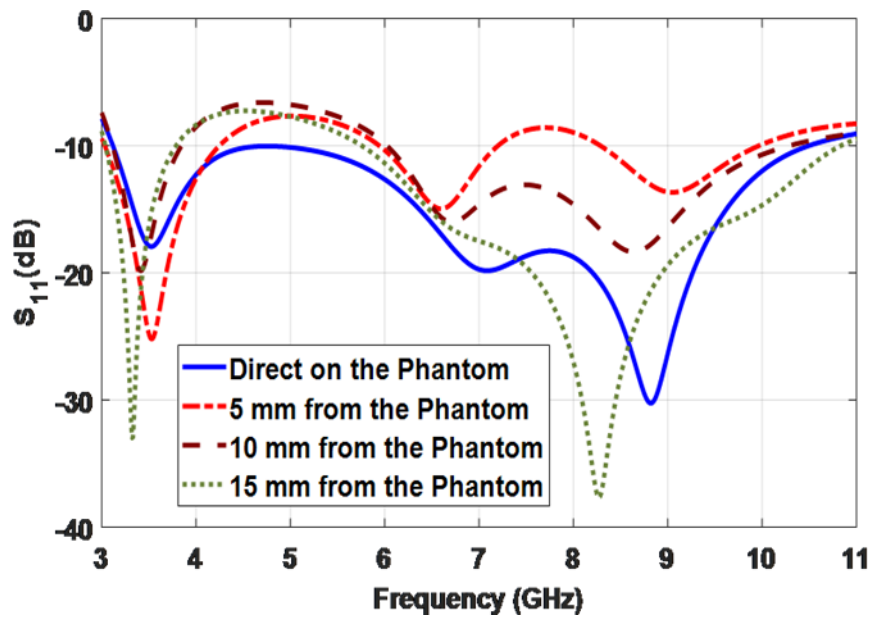
Figure 5.14: S_{11} plots of the antenna near the body the phantom.
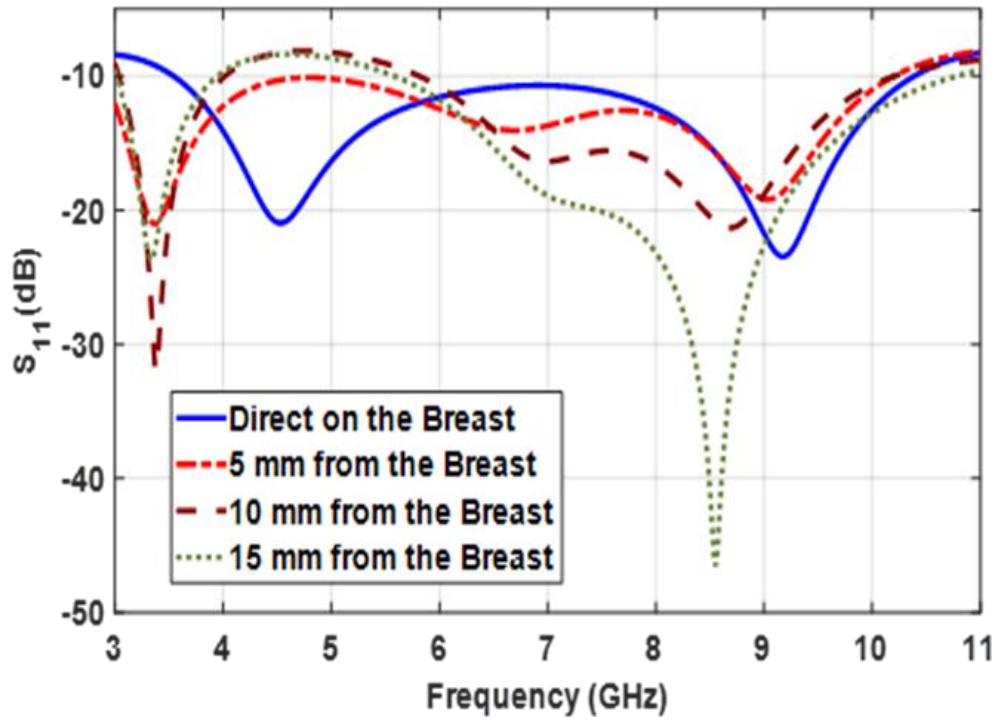
Figure 5.15: Proposed antenna placed in the closed (varying) distance to the breast mimicking tissue (phantom).

B.   On Body Return Loss

To analyse the antenna performance for on body imaging applications, a three-layer phantom mimicking the human arm model was used. The model composed of a wet skin having dielectric properties of (ε_r= 45.85, σ = 1.59), fat (ε_r= 5.28, σ = 0.1), and muscle (ε_r= 52.73, σ = 1.74), all these are calculated at the lower edge band of the UWB spectrum of 3.1GHz [197]. These dimensions are taken as an approximate tissue model since these tissue properties are not constant across the whole UWB frequency range. The dimension of the human arm model is $50\ mm^2 \times 50mm^2 \times 400\ mm^2$ equivalent to the one considered in [198] as shown in Figure 5.11. The specific absorption rate (SAR) of the antenna was also considered to determine the amount of power that the antenna can transmit within the safety limits. The IEEE C95.1-2005 standard set the SAR average value not to exceed 2 W/Kg over 10 g of human tissue mass [199]. Regarding SAR values, the IEEE limit (1.6 W/kg over 1 g) is exceeded in all the considered situations, while the CENELEC limit (2 W/kg over 10 g) is always respected [37, 199]. When the proposed antenna was fed with a 1.3 W peak input reference power, the SAR distribution averaged over 10 g of human tissue mass, extended to15.85 W/Kg value at 9 GHz. In order to satisfy the regulatory requirements of the IEEE C95.1-2005 standard, the delivered power of the antenna was decreased to 135 mW.

The effect of the human body was observed when the distance of the antenna from the human body is varied, ranging from 3 mm^2 to 15 mm^2, and the antenna response is studied and shown in Figure 5.14. From Figure 5.14, it can be seen that the antenna is a good candidate for the body-centric applications because

its S_{11} does not change significantly when in free space and proximity to the phantom.

C.   Antenna Performance in Proximity to Breast Phantom

The experiment of the proposed antenna was also carried out to evaluate the antenna performance when placed in proximity to a phantom mimicking average breast tissue, based on the recent developments of various medical diagnostic applications of microwave technologies [200]. The breast-mimicking phantom was prepared from scattering materials used to represent the tumour including 10 g of wheat flour mixed with 5.5 g of water. The combined mixture has a relative permittivity of 23 with a conductivity of 2.57 S/m at a frequency of 4.7 GHz [201]. This mixture is used in this experiment to represent and place inside the phantom breast oil for the experimentation analysis. Our experiments are summarised in Figure 5.13. It comprises of circular tube dimensions of 8 cm x 8 cm x 20 cm, filled with vegetable oil, as indicated in Figure 5.12. The circular tube is mimicking the skin being replaced by a Plexiglas barrier of 2 mm^2 thickness having dielectric constant varying between 2.39 to 2.59, with corresponding conductivity of 0.009-0.007 S/m. The vegetable oil acted as the dielectric filler for safety and cost reasons as it has been used in [202-204]. The measured S_{11} for the antenna placed on the breast phantom is plotted in Figure 5.15 with varying distances from the antenna, as illustrated in Figure 5.13 (a) and (b) respectively. Although the properties of the tissue-mimicking phantom are quite different from the simulated phantom or its equivalent tissue, volume seen by the antenna when placed on-body as in Figure 5.11 and on the breast as in Figure 5.12 suggests that the antenna is robust to variation in the properties of tissues and maintains its UWB operation.

D.   Breast Cancer Image Reconstruction Algorithm

Image reconstruction algorithm can be either a data-dependent or non-data dependent image reconstruction algorithm. The data-dependent algorithms can reconstruct high-resolution images when the array steering vector corresponding to the signal of interest (SOI) is accurately known, which is difficult in realistic imaging scenarios. In contrast, data-independent beamformers are free from this prior information and have been continuously developed. Several data-independent algorithms are proposed, including delay-multiply-and-sum (DMAS) modified weighted- delay-and-sum (MWDAS) and filtered delay-and-sum (FDAS) [34] as indicated in Figure 5.16 and Figure 5.17, respectively. Compared with the classical algorithms, improved performance of clutter rejection is offered by DMAS and DAS. FDAS shows its capability of detecting multiple scatters in dense breasts, where the presence of fibro-glandular tissue is considered. It is recognised that the increased heterogeneity of healthy breasts introduced by glandular tissues constitutes a big challenge for tumour detection. There are two reasons for this: first, although there are a large dielectric and conductivity contrast between healthy and cancerous tissues, the difference between glandular and cancerous tissues is much less pronounced. Also, the glandular tissue introduces a significant amount of attenuation and dispersion in backscattered signals, making it more challenging to detect any small tumours present.
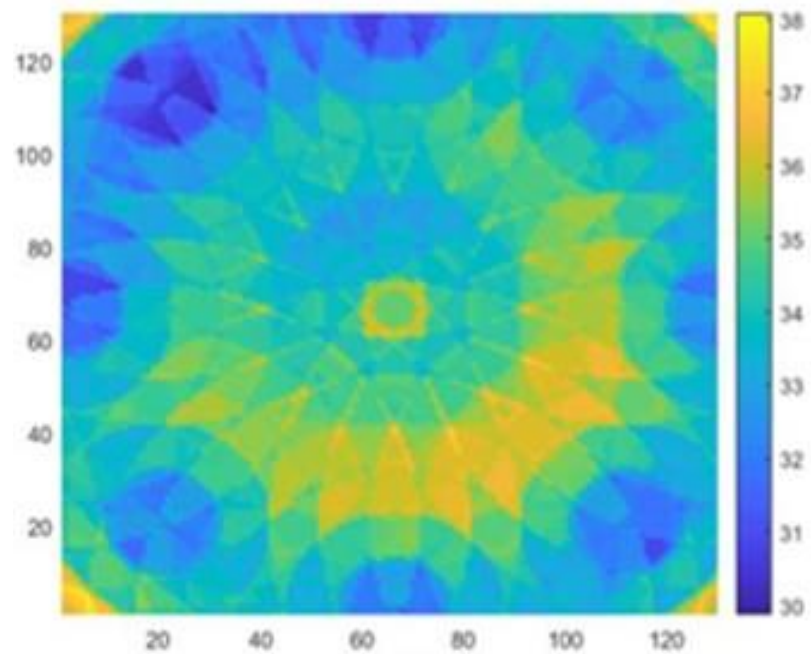
(a)
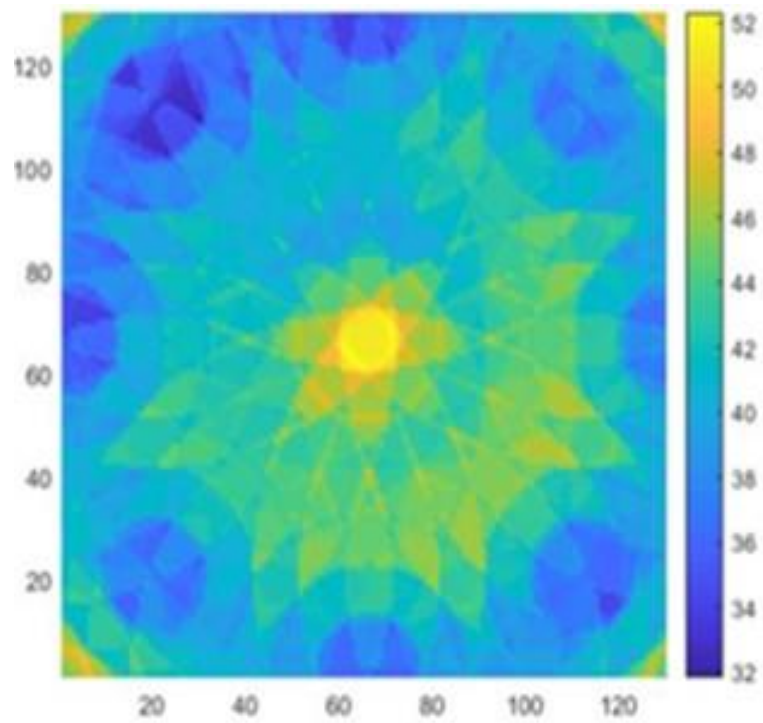
(b)

Figure 5.16: (a) DAS algorithm with Cancer Cell (b) DMAS algorithm with

Cancer Cell.

(a)

(b)

(c)
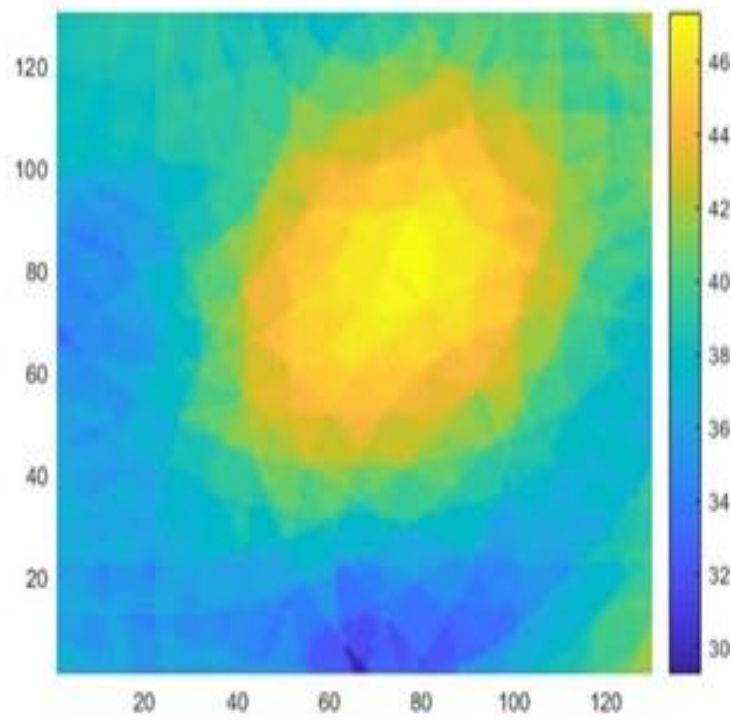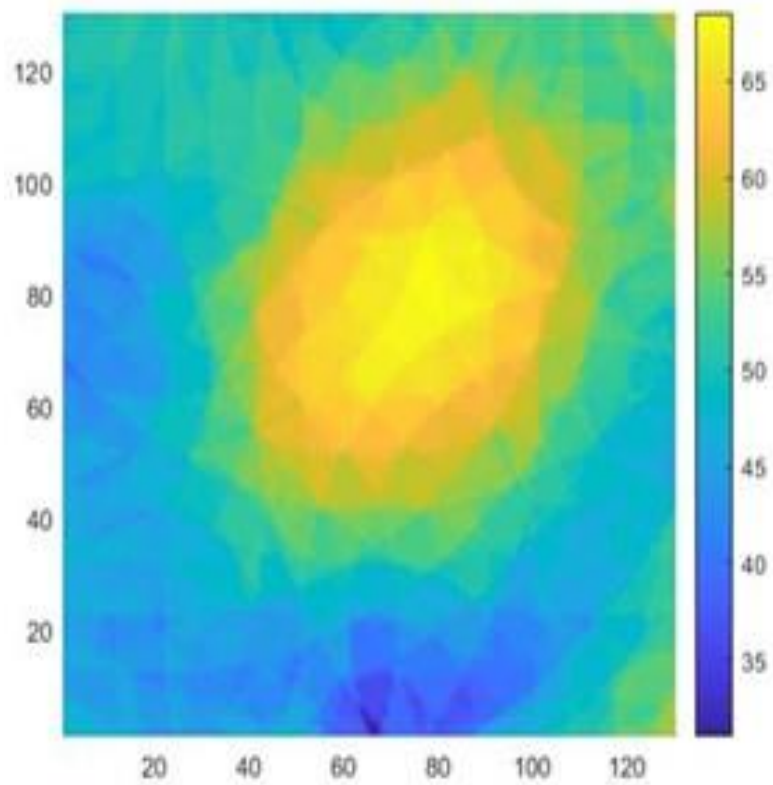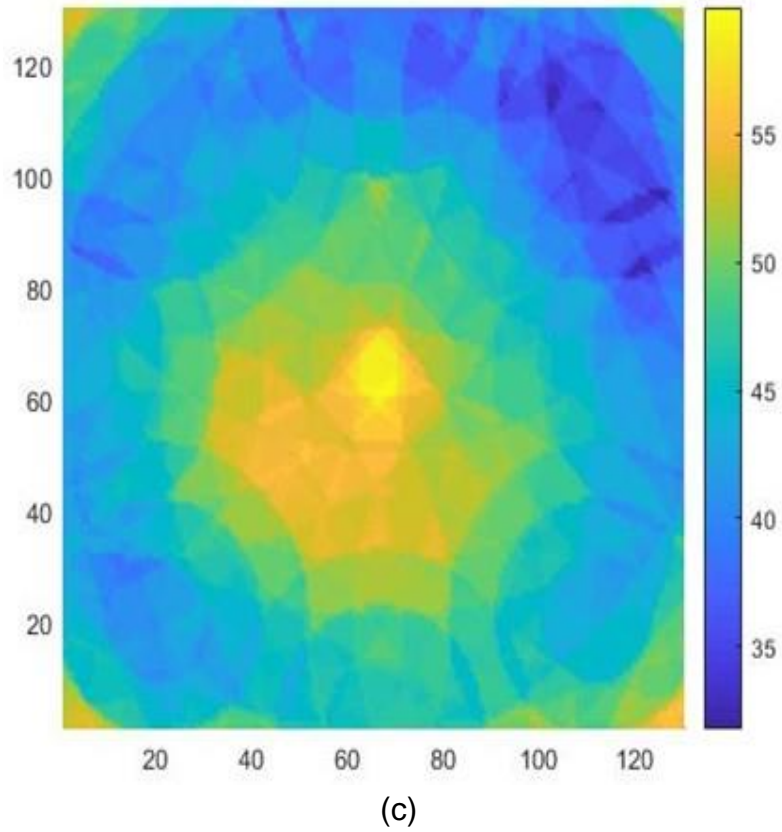
Figure 5.17: (a) DAS algorithm without Cancer Cell, (b) DMAS algorithm without Cancer Cell, (c) FDAS with double cancer cells.

E.   Time-Domain Study Analysis

The performance of the UWB antenna depends on its time-domain operation used in characterising the received signal relative to the transmitted signal. To achieve this, the scattered signal will be post-processed and then compared it with the source signal. Therefore, it is vital to compute the level of distortion of the radiated signals in the time-domain. One parameter to consider in this analysis is the antenna's fidelity, which measures the cross-correlation of the input signal relative to the received signal by their energy. Gaussian pulse being the simplest signals was used to analyses the antennas fidelity by exciting the proposed antenna using equation 5.3, owing to its unique properties in terms of time and frequency-domain operation.

126

$$V_{\mathrm{mod}}(t) = \left[\sin\left(2\pi f_c t\right)\right] e^{-\left(\frac{t-d}{b}\right)^2} \qquad (5.3)$$

Where $V_{\mathrm{mod}}(t)$ represent the sine-modulated signal, b is the pulse width, d is the time delay, and f_c is the modulated frequency. The sine modulated excitation signals are shown in Figure 5.18, and the spectrum of interest is centred at two various modulated frequencies, f_c= 4.5 GHz and 6.5 GHz, using b = 220 and 420 as shown in Figure 5.19.

In the experiment setup, the configuration composed of two similar rectangular slotted monopole antennas. The transmitter and receiver are collocated in two different scenarios, i.e. face to face and side by side to each other, with a distance of 12 λ spectrum of the lower band of the UWB frequency. The fidelity factor for face-to-face was 0.9481, and side-to-side was 0.5676, which proves the lower distortion of the signal and confirms that these pulses are within the FCC regulations. It can be seen that the power spectral density at two various modulated frequencies of the radiated pulse, clearly indicate the uniform signal strength in the energy variation of the two frequencies and satisfy the FCC defined emission mask in most of the UWB spectrum. The Modulated Gaussian Pulse with varying pulse width is shown in Figure 5.20.
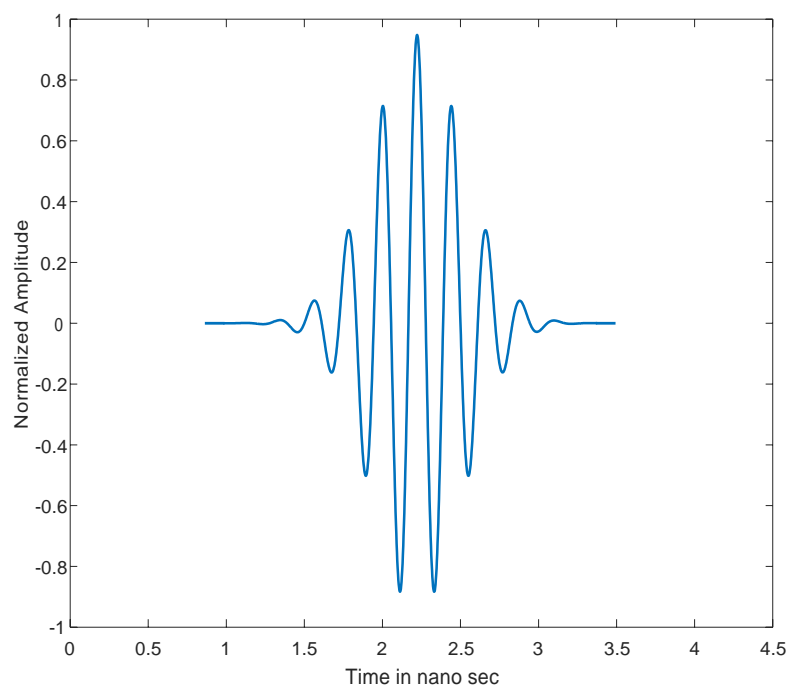
Figure 5.18: Sine modulated excitation signal.
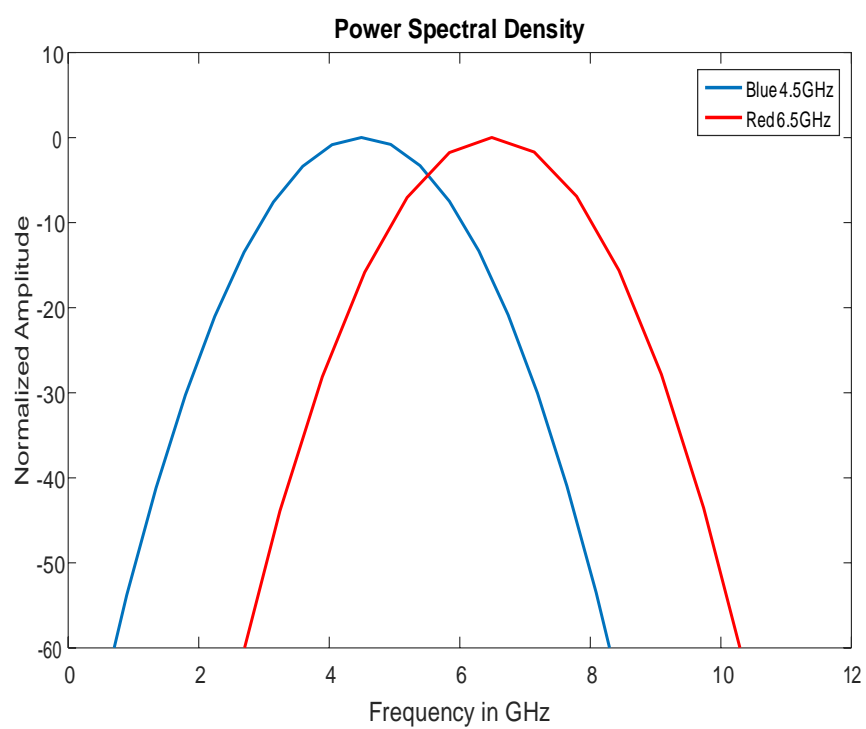
Figure 5.19: Modulated Gaussian pulse Power Spectral Density at 4.5 GHz

and 6.5 GHz.
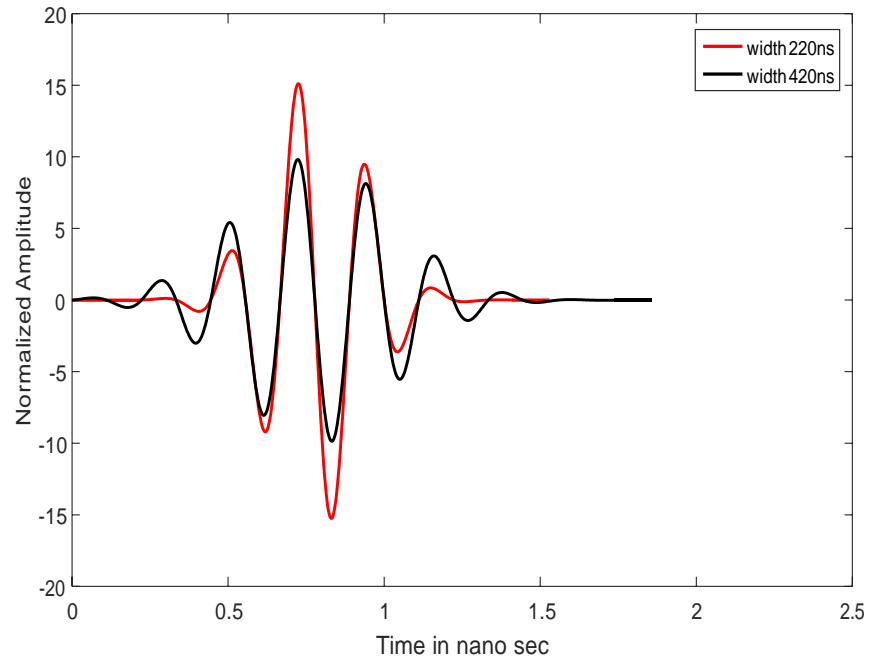
Figure 5.20: Modulated Gaussian Pulse with varying pulse width.

5.4 Conclusion

This chapter emphasised mainly on two monopoles antenna designed for microwave imaging applications. The on-body performance of printed circular monopole antenna with T- and Rectangular slots were examined respectively, by using an actual human body as a case study. An experimental investigation was made by taking on-body measurements on the chest of the human body. Also, the measurement of the antenna performance on other parts of the body was carried out. The results suggest that the antenna is robust to variation in the properties of the body tissues and maintains its UWB operation. An experiment was also conducted on the time domain operation of the proposed antenna using the sine modulated signal to determine the modulated Gaussian pulse power spectral density at the spectrum of 4.5 GHz and 6.5 GHz respectively. The antenna fidelity factor for face-to-face and side-to-side was 0.9481 and 0.5676, which proves the lower distortion of the signal and confirms that these pulses are within the FCC regulations.

Chapter 6

Antenna Array Applications

6.1   Introduction

The term array, in antenna concept, refers to the arrangement or assembly of radiating or receiving antenna elements in the electrical and geometric configuration. These antenna configurations are arranged in such a way that the radiation from the individual elements ''sums up'' to give the desired maximum field intensity in a given direction or directions and cancels or nearly cancels in the other direction or directions.

Assemblies of antenna elements (arrays) are used to achieve the required gain characteristic and directive radiation pattern of the sensors using an antenna with smaller dimensions. The geometrical antenna configuration, individual elements performance, mutual coupling, amplitude and phase excitation are factors used in the determination of the radiation pattern array. This concept can be used to design a directional antenna with the required gain.

6.2   Microwave Imaging Using Arrays of Antenna Elements

The microwave imaging technology uses the characteristics of the different dielectric properties of the tumour and the neighbouring healthy tissues to determine the accurate and high-resolution properties of the target of interest.

Microwave frequencies identify the tumour and healthy tissues differently, which is the basis for possible detection of cancerous cells. An antenna array will be

used in transmitting these microwave pulses to the suspected area of the human tissue. The reflected signals are backscattered and picked up by the array and then analysed using a suitable computing system to detect the present or absent of the tumour.

Array configurations can be divided into three main classes including linear, planar and circular arrays in the geometrical arrangement. The linear array is formed by placing the elements with finite distances apart along a straight line. Figure 6.1 shows the linear array structure. In planar array, the antenna elements are distributed on a plane or flat surface, as shown in Figure 6.2. Planar array offers the advantage of controlling the radiation pattern and scanning the main beam in the given direction quickly. Symmetrical patterns are formed by planar arrays with lower side lobes as compared to those of linear arrays. In a circular array, the elements of the array are placed in a rotational manner along a circle. The circular array is usually used for specific applications like navigation, radar and sonar, as indicated in Figure 6.3.
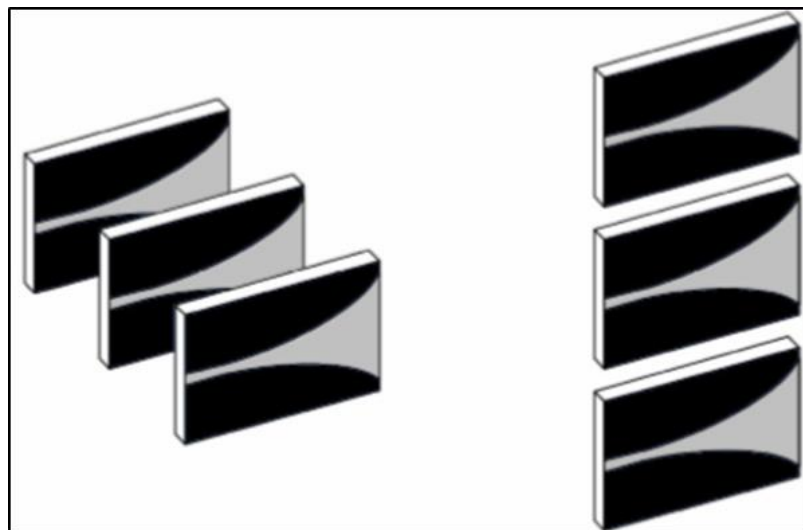
Figure 6.1:   Linear array configuration [24].
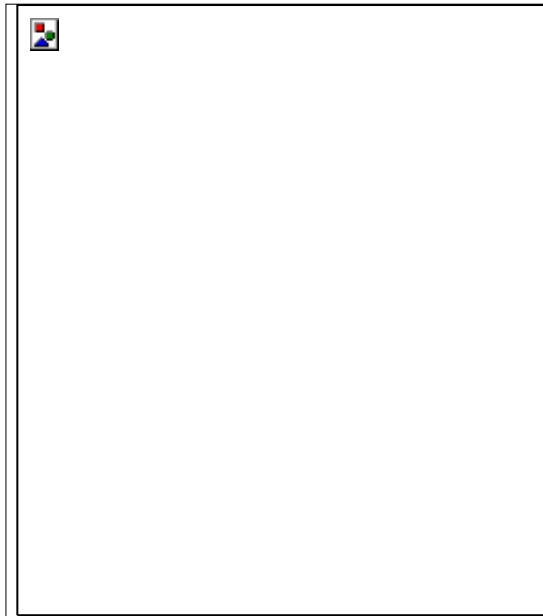
Figure 6.2:   Planar array configuration [24].
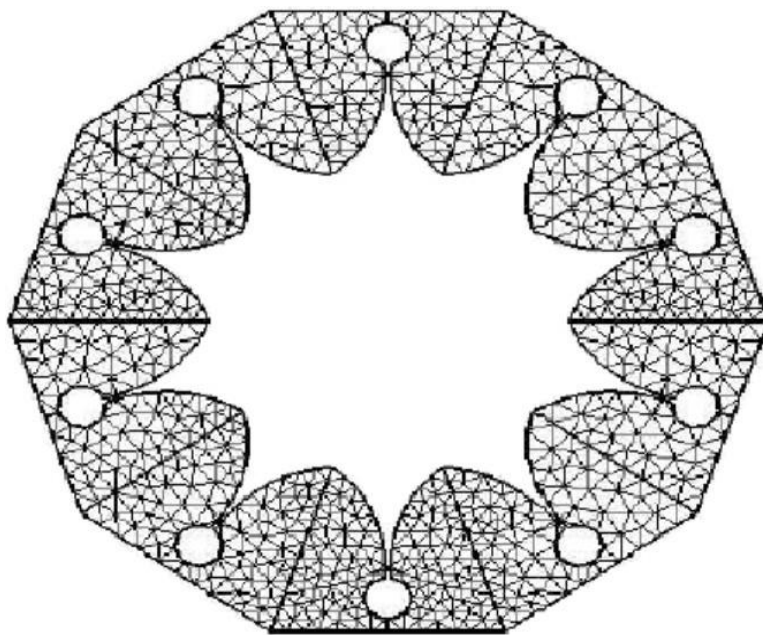
Figure 6.3:   Circular array configuration [24].

6.3 A Compact UWB Antenna Array for Microwave Imaging Applications

Microwave imaging applications in non-destructive experiments have yielded tremendous and vital impact in both military and civilian applications. This application also finds ongoing and potential relevance for several medical applications such as breast cancer imaging application [205]. Breast cancer is a disease that occurs due to the presence of a malignant cell inside the breast tissue. This scourge constituted a major cause of unwanted death among women all over the world [206]. In the United Kingdom, one in eight women are being diagnosed; thus, causing many thousands of deaths every year [207], it is therefore imperative for its early detection. Early detection and treatment could yield the survival rate of almost 97%, which emphasises the vital requirement for a reliable, effective and efficient method of early breast cancer detection.

Medical imaging currently depends on various techniques, including X-ray mammography, magnetic resonance imaging (MRI) and echography. However, these techniques witness some impediments and hence, more effective and efficient approaches are desired. The use of microwave subsurface radar (MWR) as a medical imaging technique for breast cancer screening offers several benefits over other imaging methods. Microwave imaging is a non-ionizing, non-invasive, and low cost, and it does not require breast compression as compared to x-ray mammography [58]. Microwave imaging does not need the infrastructure of the MRI, which is very large and costly. Additionally, Microwave imaging techniques have the advantages of high data rates, low complexity, and low spectral power density.

In microwave imaging, the antenna is used as a transceiver to transmit and receive microwave signals into the breast tissues. This principle is based on the variation of electrical properties of different tissues such as the relative permittivity and conductivity. The scattered signal reflected from the antenna is used to detects the contrast in the dielectric properties between healthy and tumour tissue in a more efficient, effective, safe and accurate manner. This technique uses the differential of the water content between the cancerous tissues and non-cancerous tissue. Healthy tissue is transparent to microwaves in contrast to the abnormal tissue. The high water content clustered within the cancerous cell colonies and act as a strong scattering point resulting in differential response for the determination of tumour [58]. Thus microwave imaging could serve as an early-stage screening tool, thereby saving much life.

In this work, a novel compact UWB antenna array is presented for microwave imaging. The antenna was designed to operate in the UWB band spectrum ranging from 3.1 GHz -10.6 GHz. The antenna is characterised by its ease of fabrication, small size and low profile, making it suitable for array in the microwave imaging application. The resulting array features excellent mutual coupling between the neighbouring antennas, which is below -20 dB.

6.3.1 Proposed Antenna Geometry and Design

The proposed antenna has a uniform geometry of 30 mm^2 x 30 mm^2 on FR4 substrate with a thickness of 1.6 mm^2, the permittivity of 4.6, and loss tangent of 0.0025. The primary antenna structure consists of a hexagonal patch, a feed line and 2 uniform rectangular planes acting as a partial ground. The hexagonal patch parameters were as follows: Substrate length (SL), Substrate width (SW), Patch

length (PL) Microstrip length (ML), Microstrip width (MW), short side (SS), Long side (LS), radius (R), and angle (a^0), as shown in Figure 6.4. The values of UWB antenna parameters are tabulated in Table 6.1. The proposed antenna is connected to a 50-Ω SMA connector for signal transmission.
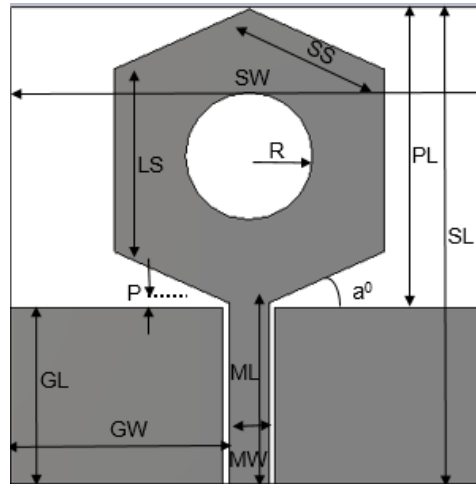
Figure 6.4:   Geometry layout of the hexagonal monopole antenna.
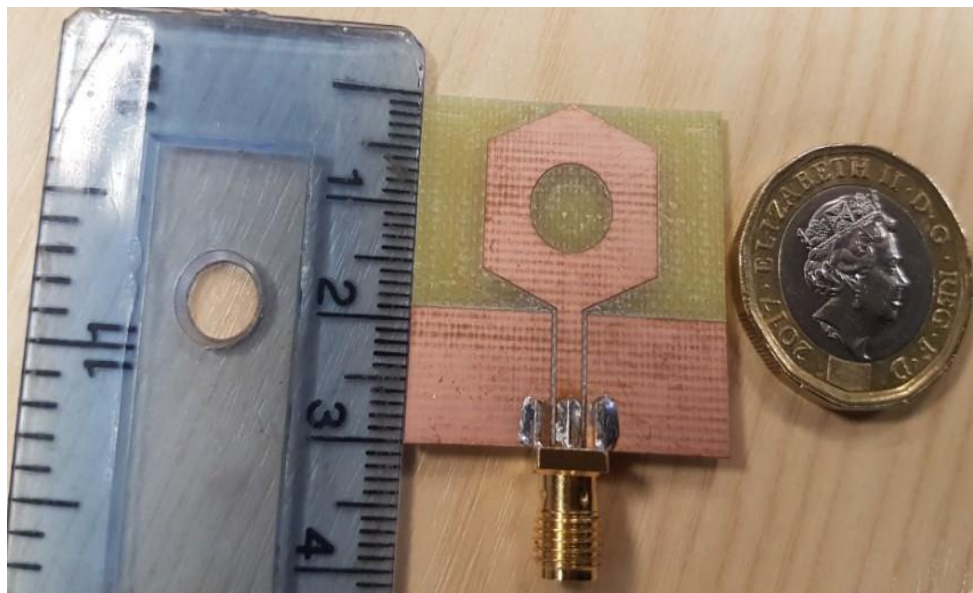
Figure 6.5:   Physical implementation of the proposed slotted planar monopole antenna.
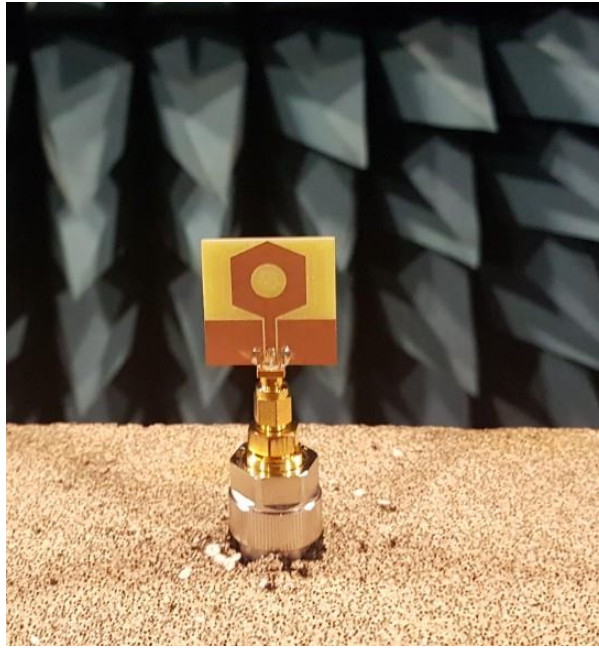
Figure 6.6:   Far-field Measurement of the proposed hexagonal monopole

antenna in the anechoic chamber.

Table 6.1: Dimensions specification for the Hexagonal Monopole antenna.

Parameter	Dimensions in mm
Substrate width (SW)	30
Substrate length (SL)	30
Substrate thickness	1.6
Microstrip length (ML)	11.40
Microstrip width (MW)	2.50
Microstrip gap (M_G)	0.4
Long Side (LS)	11.49
Short Side (SS)	9.30
Radius (R)	4
Angle (a^0)	25
Partial ground length (GL)	11.10
Partial ground width (GW)	13.35

The simulation results of the proposed antenna have been analysed and optimised using CST microwave studio. The simulated result was plotted using Matlab software while the measured results were obtained using Agilent technologies N5242. A vector network analyser is covering the spectrum ranging 10 MHz - 26 GHz. The simulated measurement is shown in Figure 6.7, while the simulated and measured return loss results are indicated in Figure 6.8. It can be seen that the -10 dB operating bandwidth of the proposed antenna covers the UWB spectrum ranging from 3.1 GHz to 10.6 GHz.
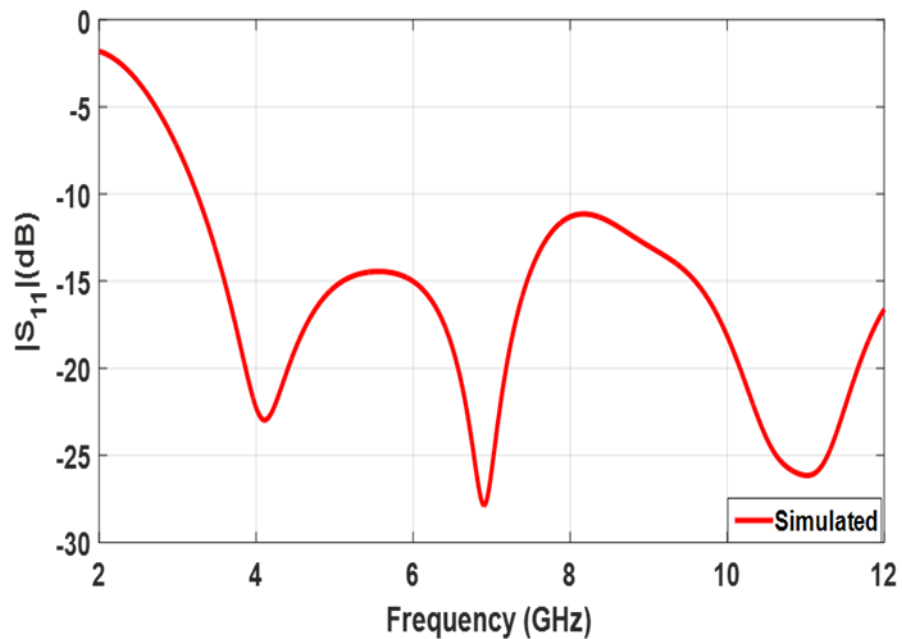
Figure 6.7: Simulated result of the proposed hexagonal monopole antenna.
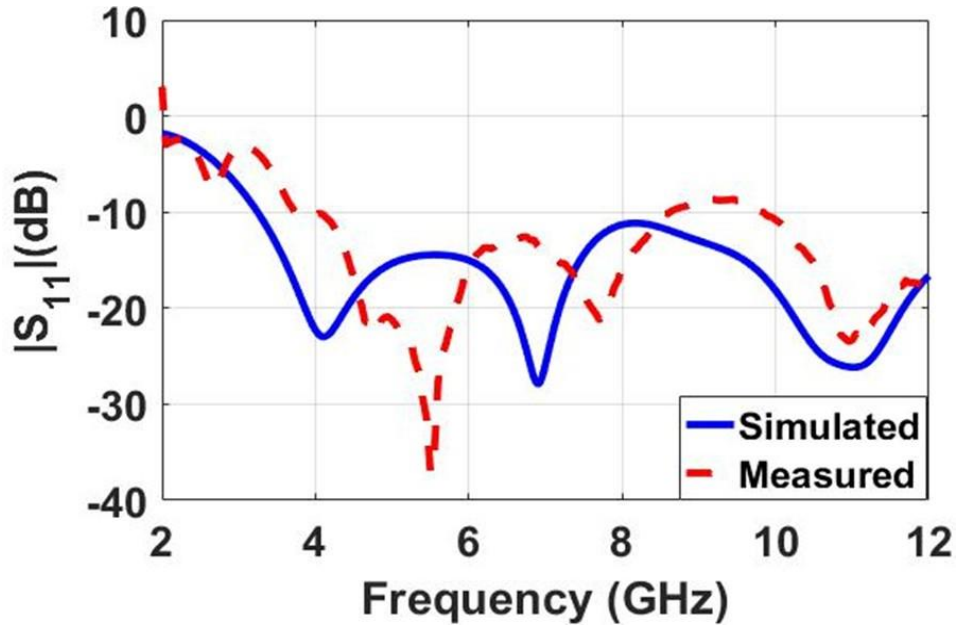
Figure 6.8: Simulated and measured results of the hexagonal monopole
antenna.

The first resonance is indicated at 3.99 GHz, the second resonance at 6.5 GHz
while the highest resonance is at 10.6 GHz. The lower frequency bandwidth is
primarily affected by the use of the slot in the patch of the monopole antenna. If
the slot is etched on the radiating patch, then by convention, the current flow will
follow the curvature of the slot. As a result, the geometry of the slot affects the
surface current distribution, as shown in Figure 6.9. The radiation of the antenna
can then be controlled by controlling the path of the surface current [191].
Although the proposed antenna design is simple and compact in size
configuration, it achieves the overall impedance bandwidth of the UWB spectrum,
and the simulated and measured results are in good agreements.
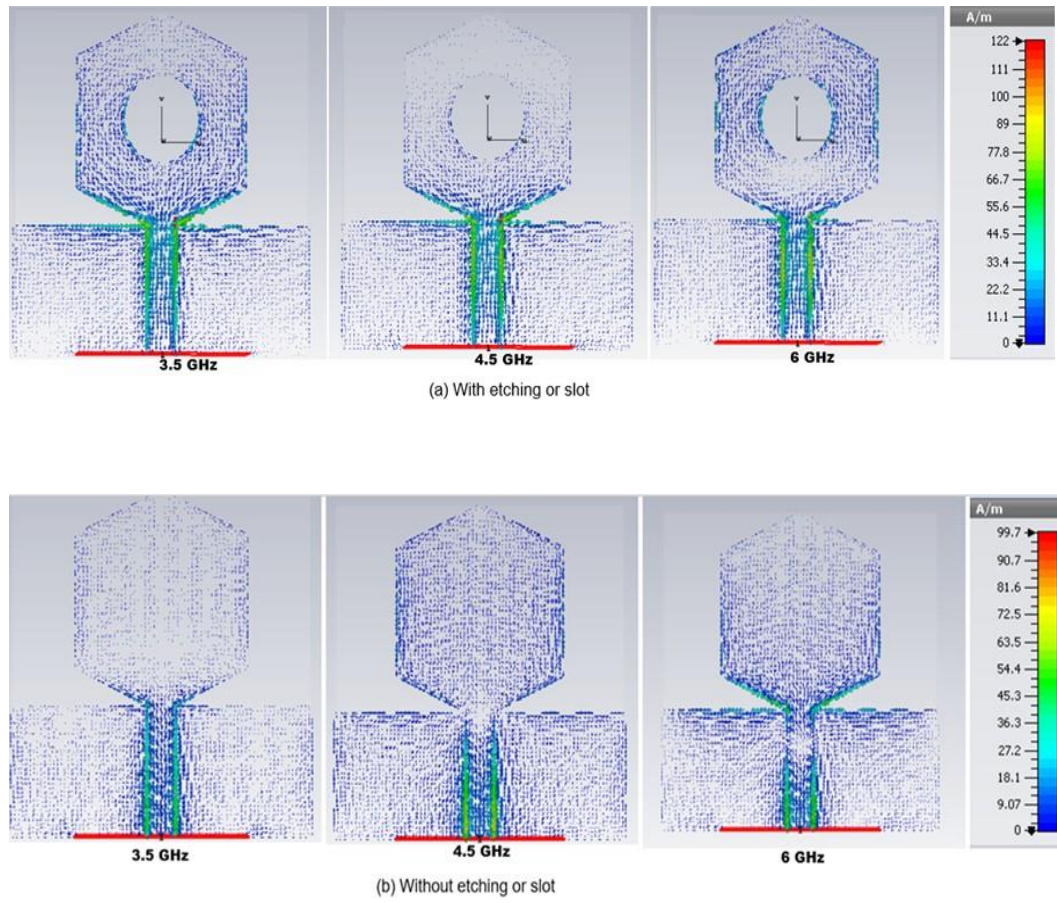
Figure 6.9: Surface current densities of the design proposed antenna.
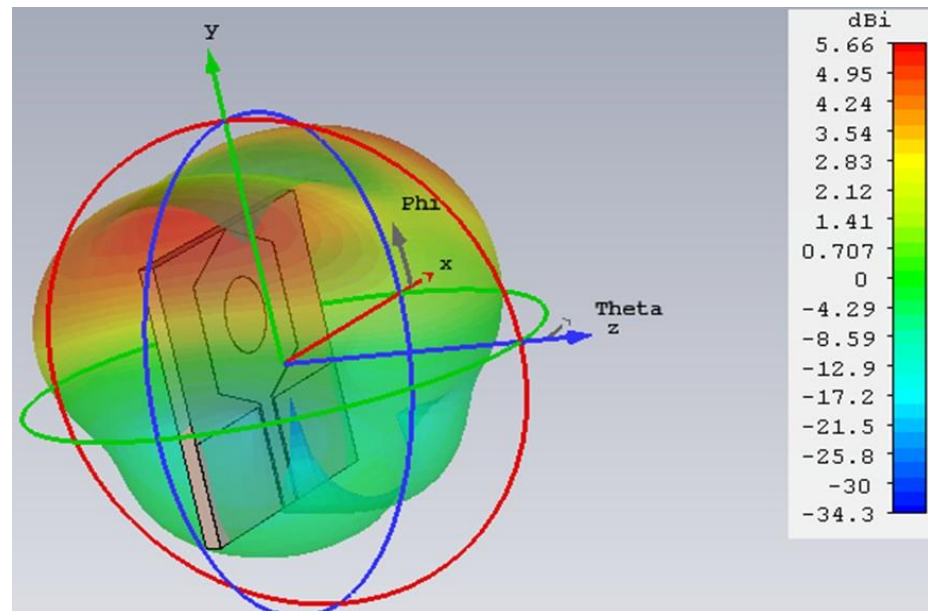
Figure 6.10: 3D far-field radiation pattern of the proposed hexagonal monopole antenna.

The array configuration has been analysed such that each antenna element is arranged halfway from each other according to the number of the antenna elements of 360/n where n is the number of the antenna elements. Circular array configuration was used for this experiment to model the three-layer phantom consisting of tumour, fat and skin. The tumour has a dimension of radius 4 mm and the scattering material used to model the tumour consisted of 10 g of wheat flour mixed with 5.5 g of water acting as a solvent. The tumour mixture electrical parameters have a relative permittivity of 23 and a conductivity of 2.57 S/m at a spectrum of 4.7 GHz. [201]. This mixture is used to represent a tumour of various sizes and usually used within the breast phantom for experimental purposes.

The breast phantom electrical properties were taken from [51], and the modelling of skin and fat phantom were taken from CST's material library. The skin and fat have the following dimensions: skin with radius 82 mm^2, the thickness of 2 mm^2 and depth of 32 mm^2, fat with radius 80 mm^2 and depth of 32 mm^2. The plastic layer was modelled around the breast phantom as it was used in [208] to support the antenna array. The plastic layer has a dimension including relative permittivity of ε_r = 3, conductivity of σ = 0.0015 s/m, radius = 92 mm^2, thickness = 8 mm^2 and depth of 32 mm^2. In order to compare the performances of the experiments, four antenna array configurations were conducted.

The breast phantom and four-antenna array elements configuration are indicated in Figure 6.11. This particular array configuration was chosen as the design is proposed for a hemispherical cup having a radius of 101 mm^2 adopting a rotation mechanism for the microwave breast imaging application. The coupling between the four arrays elements with the breast phantom is shown in Figure 6.12. There is a good mutual coupling between the antennas, which is below -20 dB.
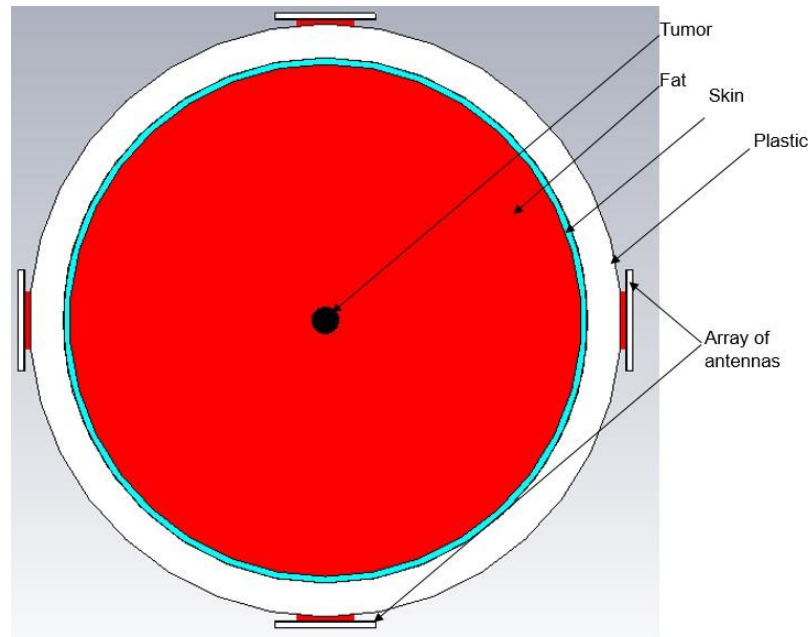
Figure 6.11: Model of the phantom with the antenna array elements.

6.4   Microwave Imaging Using Arrays of Vivaldi Antenna for Breast Cancer Applications.

In this work, microwave imaging using arrays of Vivaldi antenna was presented for breast cancer detection. The design of a Vivaldi antenna was initially carried out, and many parameters are studied and optimised for breast imaging application over ultra-wideband frequency (3.5 GHz-9 GHz). The overall size of the antenna is 0.57 λ x 0.406 λ at the lower frequency of 3 GHz. Advanced image reconstruction algorithms based on the reflected signal of the Vivaldi antennas are then utilised for the imaging task. The algorithms provide sharper and superior identification capability, accurate and reliable positioning, strong robustness, and efficient computational speed.

Vivaldi antenna is a good candidate for microwave imaging due to its wideband, high gain, stable directional radiation pattern, end-fire radiation, and resonant at

a lower frequency. Other features are low cost and low profile [51]. Several types of Vivaldi antenna have been designed for medical imaging such as miniaturised antipodal- Vivaldi antenna, cross-Vivaldi antenna, Vivaldi antenna with planer director and cavity-backed Vivaldi antenna [58, 172, 209]. Vivaldi antenna designs have challenges of size reduction and gain that are due to its feeding transition techniques and parametric geometry of the antenna [58]. Some of these challenges are studied to improve the performance of the antenna. In [210], a Vivaldi antenna is proposed by adding parasitic ellipse inside the flare. Although the parasitic ellipse improves the field coupling, however, the antenna has large dimensions of (140 mm^2 x 66 mm^2), and the antenna does not reach lower frequency and hence not suitable for arrays. In [211], a tapered slot antenna of size (75 mm^2 x 75 mm^2) is studied. Antenna parameters were optimised, and the directive radiation pattern is achieved, but resonant is not obtained at high frequency.

6.4.1 Design and Physical Implementation of the Proposed Antenna

The geometric layout of the top and bottom of the Vivaldi UWB antenna is shown in Figure 6. 12 and 6.13, respectively. The antenna is printed on FR4 substrate with a thickness of 1.6mm, the relative permittivity of 4.3 and a loss tangent of 0.025. The overall size of the antenna is 0.57λ x 0.406 λ at the lower frequency of 3 GHz. The Vivaldi antenna is fed with 50 Ω coaxial cable microstrip lines. Simulated and measured results indicated that the proposed antenna could obtain bandwidth from 3.5 GHz to 9 GHz with high directive radiation pattern, as indicated in Figure 6.14. The radiating properties of the proposed antenna are determined by a set of exponential curves, slot lines, tapered rates, the cavity structures, the slot lines, back wall offset, stub arrangement and the feeding

position. The main radiating fins are flare with height H_f = 36 mm² and length L_f =20 mm² with a taper rate R of 0.18 (factor determining the initial rate of the flare) of the inner exponential curve and the exponential curve is determined by:

$$x = C_1 e^{Rz} + C^2 \tag{6.1}$$

Where

$$C_1 = \frac{x_2 - x_1}{\left(e^{RZ_2} - e^{RZ_1}\right)} \tag{6.2}$$

And,

$$C_2 = \frac{x_1 e^{RZ_2} - x_2 e^{RZ_1}}{\left(e^{RZ_2} - e^{RZ_1}\right)} \tag{6.3}$$

The points(x_1, z_1) and (x_2, z_2) represents the end-points of the flare. The cavity at the end of the flare is C_d= 10 mm² . This cavity is adjusted with the equation:

$$C_d = 0.5\ C_d - 0.5\ (\cos\theta) \text{ and } \theta = \sin\left(\frac{S_w}{C_d}\right)$$

The cut-off frequency of the proposed taper slot antenna can be calculated with equation 6.4.

$$fc = \frac{c}{W'\sqrt{\varepsilon_r}} \tag{6.4}$$

Where fc the centre frequency, c is the speed of light, ε_r is the relative permittivity, and W' is the flare opening rate. S_L represents the slot line between the cavity and flare with a slot line width S_W of 0.5 mm². The back wall offset has a value of 5 mm². A microstrip slot with a radial stub is introduced to achieve a wider operating bandwidth. The stub angle of the radial stub is at θ = 55 degrees with a radius of R = 10 mm². The feeding line has a microstrip taper of length F_L = 31.50 mm² and taper feed width of F_W = 1.50 mm². The microstrip taper is

connected to the stub with a microstrip coupler of length L_c = 16.80 mm² and width L_w of 1.50 mm². The microstrip feeding line is fed with a 50 Ω Subminiature connector version A to feed the antenna. The electrical properties of the SMA connector are 2.08 dielectric constant and 4.62 S/m electrical conductivity.
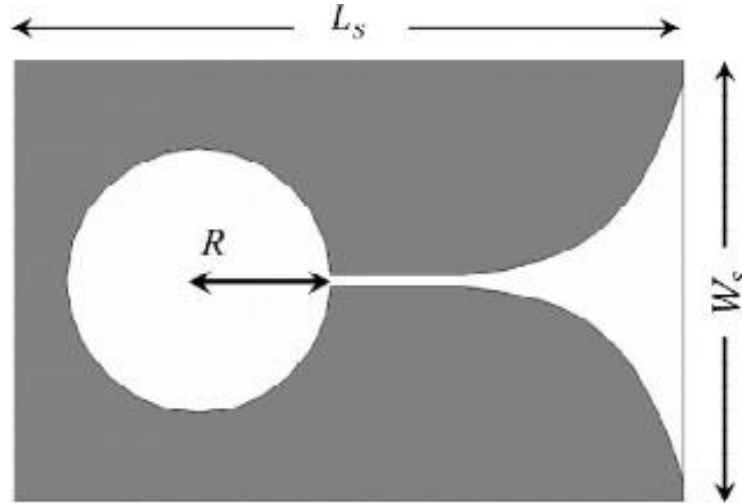
Figure 6.12: Top view of the proposed antenna.
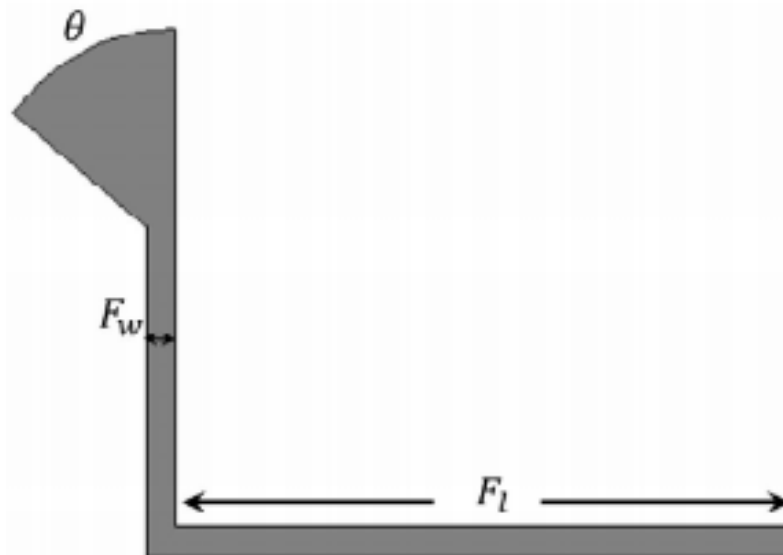
Figure 6.13: Bottom view of the proposed antenna.

6.4.2 Parametric study and optimisation of the Proposed Antenna

An initial parametric study of the proposed Vivaldi antenna is carried out using CST MWS to determine the possible search ranges of the design variables. The physical dimensions considered for the parametric study of the antenna include substrate's length (L_s) and width (W_s), the ground plane's length (G_l) and width (G_w), the radius of the stub (R) and the microstrip feed line's length (F_l) and width (Fw) at a fixed copper layer thickness of 0.035 mm^2 . The Vivaldi antenna is optimised using a Surrogate Assisted Differential Algorithm (SADEA) in ADE 1.0 using the recommended settings in [145]. The design exploration goal is to minimise the maximum reflection coefficient (S $_{11}$) in the operating band of 3 GHz to 9 GHz subject to the realised gain (G_R) not being less than 2 dB over the operating bandwidth. The selected values of the design variables for the proposed antenna after the parametric study and design exploration are shown in Table 6.2, and the simulated results are indicated in Figure 6.13.

Table 6.2: Dimensions specification for the selected values of the Vivaldi antenna (all sizes in mm).

Variables	Values
Ls	57
W_s	40.6
F_l	31.5
F_w	1.5
S_w	0.5
⌑	55
R	10
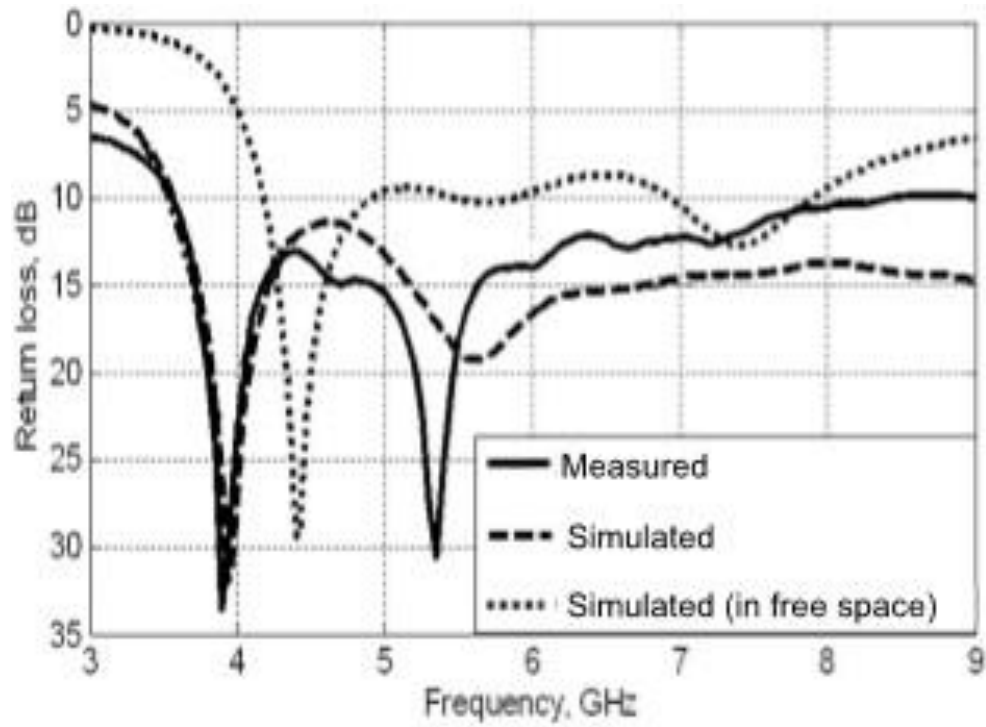
Figure 6.14: Simulated results of the proposed Vivaldi antenna.

6.4.3 Image Reconstruction Algorithm for the Proposed Antenna

Image reconstruction algorithms are proposed in recent years, including delay-multiply-and-sum (DMAS) modified weighted- delay-and-sum (MWDAS) and filtered delay-and-sum (FDAS). Compared with the classical DAS algorithm, improved performance of clutter rejection is offered by DMAS and MWDAS [34]. FDAS shows its capability of detecting multiple scatters in dense breasts, where the presence of fibro-glandular tissue is considered. It is recognised that the increased heterogeneity of healthy breasts introduced by glandular tissues constitutes a big challenge for tumour detection. There are two reasons for this: first, although there is a significant contrast in dielectric and conductivity electrical properties between healthy and cancerous breast tissues as shown in Figure 6.15 and 6.16 respectively, the difference between glandular and cancerous tissues is much less pronounced. Also, the glandular tissue introduces a significant amount

146

of attenuation and dispersion in backscattered signals, making it more challenging to detect any small tumours present.

6.4.4 *Imaging System and Results of the Vivaldi array Antenna Elements*

The antenna is the main building block for any imaging system that acts as a transceiver for transmitting and receiving microwave signals. The scattering signal is collected with the aid of a vector network analyser (VNA). All these devices are electromechanical circuits and are controlled with a PC. The measurement set up is achieved with these devices to carry out the measurement. The arrangements of the UWB Vivaldi antenna arrays on the breast tissue is shown in Figure.6.17.

The main aim is to relate the change in the backscattering signal with the presence of a tumour. The tumours present within the breast tissue are detected with the antenna arrays. In the experimental setup measurement, the VNA parameters are set with a bandwidth of 10 Hz, the number of points is M = 203, and the spectrum range of 3 GHz to 9 GHz are covered. The use of GPIB port is required to connect the PC to the VNA, and the data are received for further processing and analysis. The complex frequency-domain S- parameter data are captured with m ranging from m=1, 2…M, and n=1, 2…N, which represents the angular position of the rotation in the experimental setup.
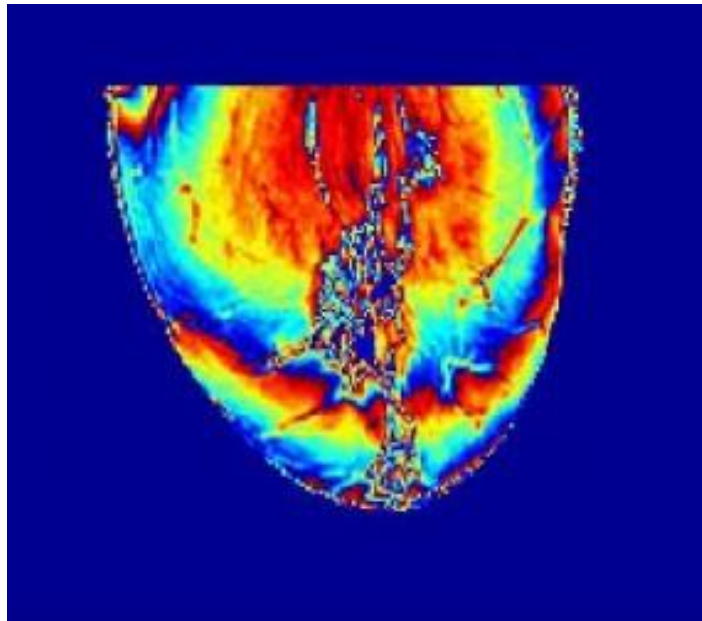
Figure 6.15: MRI Dielectric [58].
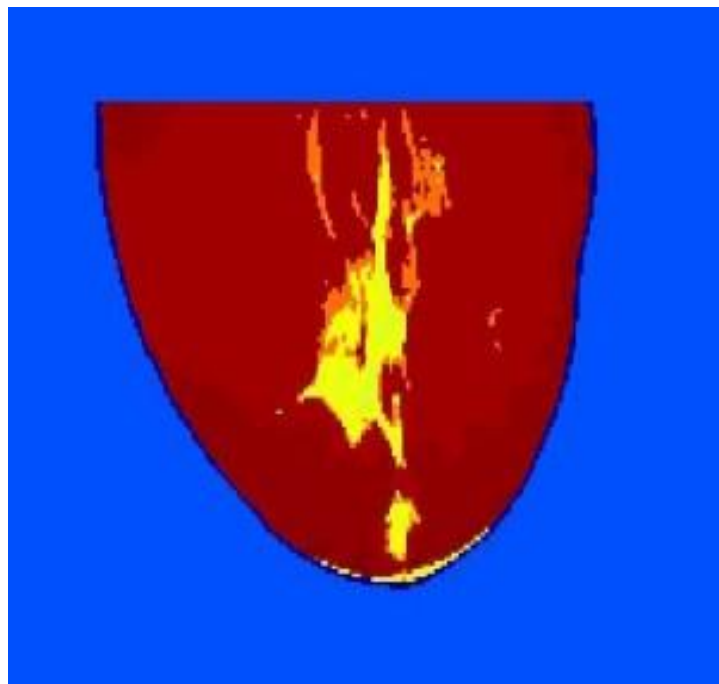
Figure 6.16: MRI Conductivity [58].
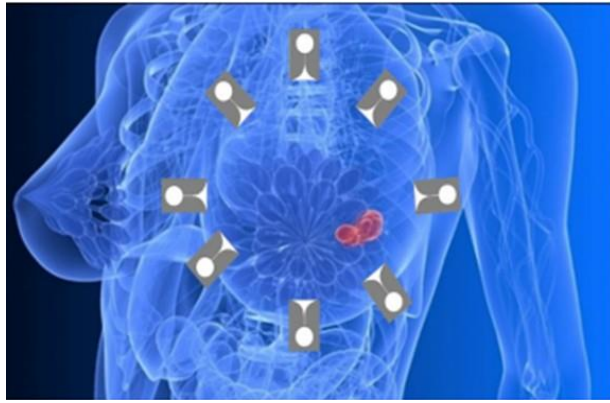
Figure 6.17: Antenna array elements of the Vivaldi antenna with the breast

tissues [58].
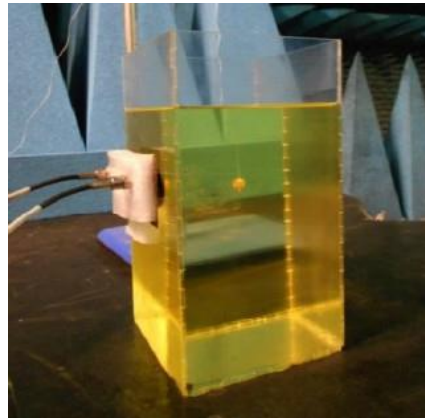
Figure 6.18: Model for the measurements [58].
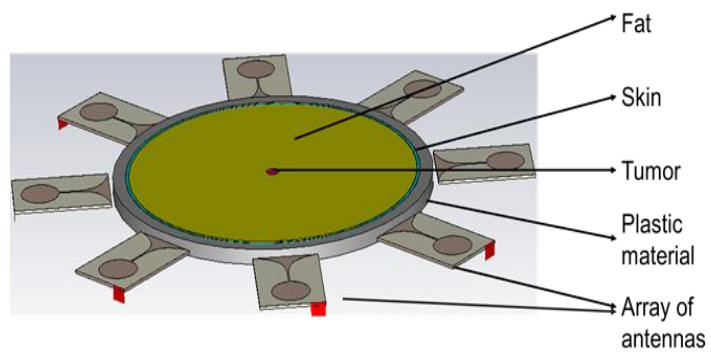
Figure 6.19: Arrangements of sensors using CST.
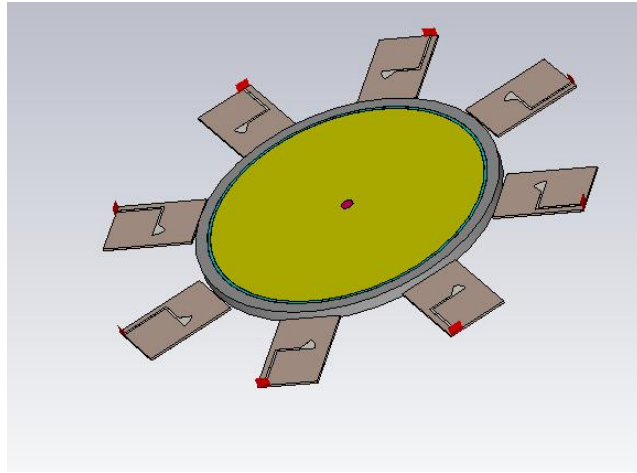
Figure 6.20: Bottom view of the array elements.
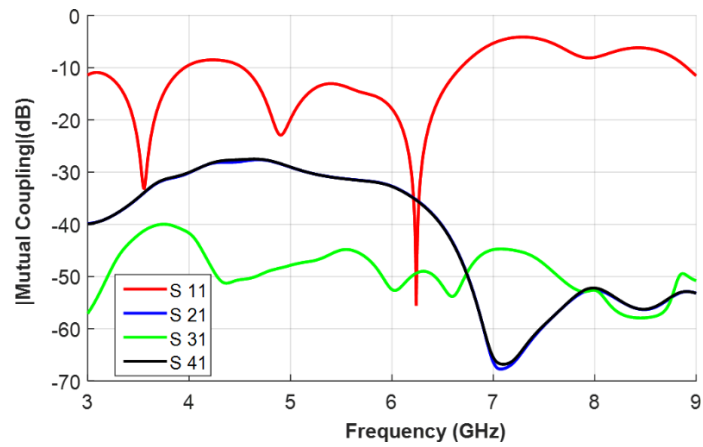
Figure 6.21: Mutual coupling of the 4 x 4-array element of the antenna.
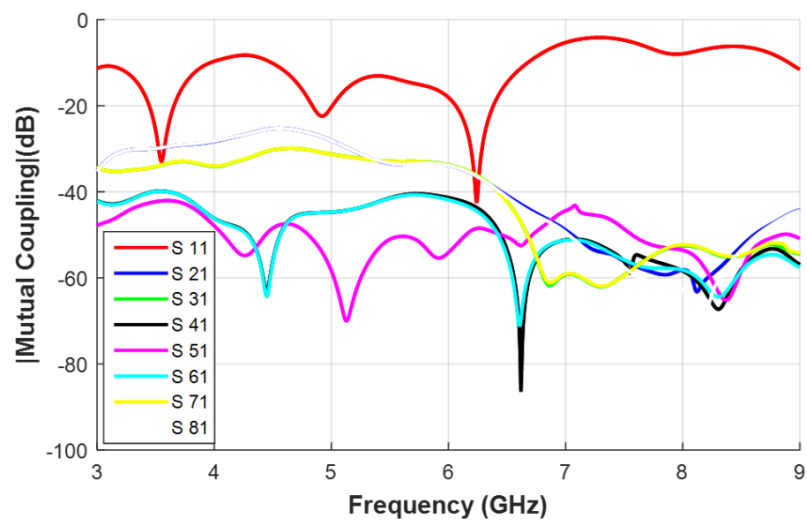
Figure 6.22: Mutual coupling of the 8 x 8-array element of the antenna.

6.5   Conclusion

This chapter presented two sensors, including hexagonal monopole and Vivaldi antennas for microwave imaging applications arrays. The proposed antennas are suitable for the array applications due to their compact size to efficiently and effectively fit within the array area and thus, making an enhanced microwave imaging resolution. Circular array configuration was chosen as the design is proposed for a hemispherical cup adopting a rotation mechanism for the microwave breast imaging application. The coupling between the elements of the array with the breast phantom provides good mutual coupling between the antennas, which is below -20 dB.

The chapter also demonstrated that the antennas could detect a small object with 5 mm in radius. At this stage, image reconstruction has not been attempted as the focus of this study is to design small UWB antennas for microwave imaging array applications. However, the results and the designs presented may be used as a step for future image reconstruction algorithms. These are usually achieved through the use of the reflected signal for subsequent image reconstruction of the target or tumour to picture the location and size of the target.

Chapter 7

Conclusions and Recommendations for Future Work

7.1 Conclusions

This thesis presented design, development and measurements of six new ultra-wideband antenna for microwave near-field imaging applications by applying optimisation algorithms. The proposed antennas designed are bow-tie antenna, a microstrip patch antenna, Vivaldi antenna and monopoles antennas including rectangular slot, T-slot and hexagonal on a circular slot antenna. These antennas were simulated in free space and through various media such as wall and human body locations to assess their performance. UWB spectrum ranging from 3.1 GHz – 10.6 GHz was used for through the wall and breast cancer imaging applications in Chapter 4 and 5, respectively. These are achieved by using the reflected signals of the UWB antennas from the target of interest. An image representation of the target or tumour is reconstructed using the reflected signal to picture the location and size of the target.

A bow ties antenna adjacent to dielectric material was designed and optimised for through the wall imaging application. The modelling and analysis of the proposed antenna use hybrid electromagnetic computational techniques of finite-difference time-domain and method of moments. The antenna shapes were parametrised and optimised using surrogate model-assisted differential Evolution Algorithm in reducing the return loss in a specific frequency band. Additionally, impedance matching and gain are optimised over a predefined frequency range. This resulted in a very small and compact bow-tie antenna with a compact size of $12.87mm^2$ x $28.62mm^2$. A new microstrip rectangular patch antenna designed for the medical and scientific band has also been presented. The designed antenna is to operate at 2.65 GHz specifically, for body-centric applications. The

compact size of the proposed antenna has a significant impact mainly when adopted for arrays. The initial return loss is not favourable. However, the length and pin position is independently optimised to get better return loss for the patch at 2.65 GHz. Additionally, the simulated and measured results are in good agreements.

A new miniaturised printed Vivaldi antenna have been proposed for breast cancer imaging applications. In this study, the design of a tapered slot low profile Vivaldi antenna for ultra-wideband microwave breast cancer imaging applications was carried out. The discussion on the experimental characterisation of the antenna in proximity to the breast phantom and wall medium were also analysed. Additionally, the performance indicators of the antenna, including its return loss, gain and radiation patterns characteristics were examined. The proposed antenna was designed to optimise the wide-band performance in the UWB range of 1 GHz to 4 GHz. The antenna also exhibits high immunity and stable radiation pattern in proximity to the breast tissue. Furthermore, antenna performance, including efficiency and radiation pattern was a trade-off for the smaller size of the proposed antenna for its to be effectively and efficiently used for arrays.

A printed circular monopole antenna (PCMA) with T slots for UWB microwave imaging applications, specifically for breast cancer detection, has been presented. The profile of the proposed antenna features T-Slots etching over a driven circular patch. The results presented in this study show that the proposed PCMA with T-slot offers high immunity into the human body. The simulated and measured results were in good agreement over the entire UWB spectrum band measured. Two new compact rectangular slots on a circular patch and hexagonal patch with circular slot monopoles UWB antennas for microwave imaging were presented. UWB signal investigation in the presence of breast phantoms was

carried out in both analyses. In the first study. It has been shown that the UWB antenna is best characterised by analysing it in its time domain operation. An experimental investigation was also carried out using a compact UWB antenna, a breast phantom consisting of simulated tumour targets, volunteer human body and a vector network analyser. The antenna performance was evaluated in free space and on-body applications. This performance shows that the antenna performs well, even in proximity to the phantoms. It is demonstrated experimentally that the proposed antenna can generate a UWB signal covering the FCC range of the UWB spectrum. Simulated and measured results demonstrate good agreements.

In the secondary analysis of the monopole antenna, the first resonance is indicated at 3.99 GHz, the second resonance at 6.5 GHz while the highest resonance is at 10.6 GHz. The lower frequency bandwidth is primarily affected by the use of the slot in the patch of the monopole antenna. If the slot is etched on the radiating patch, then by convention, the current flow will follow the curvature of the slot. As a result, the geometry of the slot affects the surface current distribution. Additionally, the experimental analysis was also carried out using a compact UWB antenna array for breast cancer microwave imaging. In the investigation, there are variations in the transmission and reception of UWB signals from phantom without tumour and with the tumour. The low profile and simple design of the antenna make it a good candidate for microwave imaging applications arrays. The antenna performance is measured based on the good mutual coupling between the antenna array elements. The antenna uniform size of 30 mm^2 x 30 mm^2 is good enough for integration into many microwave devices.

7.2   Recommendation for future work

Microwave imaging in the near-field method for exploring interior structures, including wall and the human body is a topic of growing demand. The work presented in this thesis unlocks many possible areas for further research. Microwave imaging has the advantages of fast illumination capability response of electromagnetic wave propagation. Additionally, higher range measurement accuracy and range resolution are possible with microwave imaging in the near-field. These features are achieved by enhancing the performance of the microwave imaging sensors, reducing the antenna sizes by optimisation methods for compact arrays.

Further studies on the miniaturisation and immunity of UWB antennas for microwave imaging applications should be exploited. Other significant areas that could be exploited include:

- ✓ The proposed antennas could be further investigated for the different interior part of the human body, including brain and heart.

- ✓ The efficiencies of the proposed antennas could be investigated, and the antenna array application could be extended to operate in the millimetre wave bandwidth that represents the new development of 5G mobile generation.

- ✓ The number of antenna array elements could be increased. In this study, fewer antenna elements are used in the simulations and measurements. Increasing the antenna array elements could be exploited to see if the coupling between the antenna elements would improve for further optimisation and imaging in the far-field applications such as through-wall and ground-penetrating radar.

Bibliography

1.   Mirza, A., et al., *An Active Microwave Sensor for Near Field Imaging.* IEEE Sensors Journal, 2017,p. 2749-2757.
2.   See, C.H., et al., *The design of a resistively loaded bowtie antenna for applications in breast cancer detection systems.* IEEE Transactions on Antennas and Propagation, 2012. 60(5): p. 2526-2530.
3.   Adnan, S., et al., *Microstrip antenna for a microwave imaging application.* 2011.
4.   Adnan, S., et al., *A compact UWB antenna design for breast cancer detection.* PIERS Online, 2010. 6(2): p. 129-132.
5.   Fear, E.C., et al., *Enhancing breast tumour detection with near-field imaging.* IEEE Microwave Magazine, 2002. 3(1): p. 48-56.
6.   Commission, F.C., *First report and order regarding ultra-wideband transmission system.* FCC 02-48, 2002.
7.   Berens, F. *The European flexible DAA approach towards an open UWB regulation*.
8.   Davis, J.L. and A. Annan, *GROUND-PENETRATING RADAR FOR HIGH-RESOLUTION MAPPING OF SOIL AND ROCK STRATIGRAPHY 1.* Geophysical prospecting, 1989. 37(5): p. 531-551.
9.   Baranoski, E.J., *Through-wall imaging: Historical perspective and future directions.* Journal of the Franklin Institute, 2008. 345(6): p. 556-569.
10.   Venkatasubramanian, V., H. Leung, and X. Liu, *Chaos UWB radar for through-the-wall imaging in* IEEE Transactions on Image Processing, 2009. 18(6): p. 1255-1265.
11.   Yilmaz, B. and C. Ozdemir. *A radar sensor design and prototype for through-the-wall imaging radar applications*.
12.   Danjuma, I.M., et al. *Design and optimization of a bowtie dipole adjacent to dielectric material for through the wall imaging using hybrid electromagnetic computational analysis techniques*. In *Internet Technologies and Applications (ITA), 2017*.
13.   Hunt, A.R. and R.D. Hogg. *Stepped-frequency CW radar for concealed weapon detection and through-the-wall surveillance*. In *Proc. SPIE*. 2002.
14.   Zhuge, X. and A. Yarovoy. *MIMO-SAR based UWB imaging for concealed weapon detection*. In *8th European Conference on Synthetic Aperture Radar*. 2010.
15.   Zhuge, X. and A.G. Yarovoy, *A sparse aperture MIMO-SAR-based UWB imaging system for concealed weapon detection.* IEEE Transactions on Geoscience and Remote Sensing, 2011. 49(1): p. 509-518.
16.   Cheng, T., et al. *Performance evaluation of ultra-wideband technology for construction resource location tracking in harsh environments.* Automation in Construction, 2011. 20(8): p. 1173-1184.
17.   Segura, M., et al. *Experimental demonstration of self-localized ultra-wideband indoor mobile robot navigation system*. In *Indoor Positioning and Indoor Navigation (IPIN), 2010 International Conference on*. 2010.
18.   Zhu, J. and S. Roy, *MAC for dedicated short-range communications in the intelligent transport system.* IEEE Communications Magazine, 2003. 41(12): p. 60-67.
19.   Beach, R.D., et al., *Feasibility of stereo-infrared tracking to monitor patient motion during cardiac SPECT imaging.* IEEE transactions on nuclear science, 2004. 51(5): p. 2693-2698.
20.   Ma, Y., et al. *Real-time respiratory motion correction for cardiac electrophysiology procedures using image-based coronary sinus catheter tracking*. In *International Conference on Medical Image Computing and Computer-Assisted Intervention*. .

21. Fear, E.C., et al., *Confocal microwave imaging for breast cancer detection: Localization of tumours in three dimensions.* IEEE Transactions on biomedical engineering, 2002. 49(8): p. 812-822.

22. Kumari, V., et al., *Early Detection of Cancerous Tissues in Human Breast utilizing Near field Microwave Holography.* arXiv preprint arXiv:1904.09870, 2019.

23. Mirza, A.F., et al., *An Active Microwave Sensor for Near Field Imaging.* IEEE Sensors Journal, 2017. 17(9): p. 2749-2757.

24. Pozar, D.M., *Microwave engineering.* Wiley, 2012.

25. Balanis, C.A., *Antenna theory: A review.* Proceedings of the IEEE, 1992. 80(1): p. 7-23.

26. Levin, M. and M. Miller, *Maxwell a treatise on electricity and magnetism.* Uspekhi Fizicheskikh Nauk, 1981. 135(3): p. 425-440.

27. Stutzman, W.L. and G.A. Thiele, *Antenna theory and design.* 2012: John Wiley & Sons.

28. Commission, F.C., *The first report and order regarding ultra-wideband transmission systems.* FCC 02, 2002.

29. Valderas, D., et al., *ULTRAWIDEBAND ANTENNAS.* 2011.

30. Richards, M.A., et al., *Principles of modern radar.* 2010: Citeseer.

31. Skolnik, M.I., *Introduction to radar.* Radar Handbook, 1962.

32. Ghavami, M., L. Michael, and R. Kohno, *Ultra-wideband signals and systems in communication engineering.* 2007: John Wiley & Sons.

33. Venkatasubramanian, V. and H. Leung, *A novel chaos-based high-resolution imaging technique and its application to through-the-wall imaging.* IEEE Signal Processing Letters, 2005. 12(7): p. 528-531.

34. Yin, T., F.H. Ali, and C.C. Reyes-Aldasoro, *A robust and artefact resistant algorithm of an ultrawideband imaging system for breast cancer detection.* IEEE Transactions on Biomedical Engineering, 2015. 62(6): p. 1514-1525.

35. Batra, A., S. Lingam, and J. Balakrishnan. *Multi-band OFDM: a cognitive radio for UWB.* in *Circuits and systems, 2006.*

36. Immoreev, I.I. and P.D.V. Fedotov. *Ultra-wideband radar systems: advantages and disadvantages.* in *Ultra Wideband Systems and Technologies, 2002.*

37. Abd-Alhameed, R.A., P.S. Excell, and M.A. Mangoud, *A hybrid computational electromagnetics formulation for Simulation of antennas coupled to lossy and dielectric volumes.* IEEE transactions on broadcasting, 2004. 50(3): p. 253-259.

38. Amin, M.G., *Through-the-wall radar imaging.* 2016: CRC Press.

39. Ahmad, F., M.G. Amin, and S.A. Kassam, *Synthetic aperture beamformer for imaging through a dielectric wall.* IEEE transactions on aerospace and electronic systems, 2005. 41(1): p. 271-283.

40. Chauhan, P.P.S. and D. Singh. *Through-the-wall imaging (TWI) radar for detection, classification and identification of targets based on RCS.* in *2015 National Conference on Recent Advances in Electronics & Computer Engineering (RAECE).* 2015.

41. Montoya, T.P. and G.S. Smith, *Land mine detection using a ground-penetrating radar based on resistively loaded vee dipoles.* IEEE Transactions on antennas and propagation, 1999. 47(12): p. 1795-1806.

42. Gashinova, M., M. Cherniakov, and A. Vasalos. *UWB signature analysis for detection of body-worn weapons.*

43. Paglieroni, D.W., et al., *Imaging Modes for Ground Penetrating Radar and Their Relation to Detection Performance.* IEEE Journal of Selected Topics in Applied Earth Observations and Remote Sensing, 2015. 8(3): p. 1132-1144.

44. Francké, J.C. and R. Yelf. *Applications of GPR for surface mining.* In *Advanced Ground Penetrating Radar, 2003. Proceedings of the 2nd International Workshop.*

45. Scheers, B., M. Piette, and A. Vander Vorst. *The detection of AP mines using UWB GPR.* in *Detection of Abandoned Land Mines, 1998. Second International Conference on the (Conf. Publ. No. 458).* 1998. IET.

46. Gokhale, S. and J.A. Graham, *A new development in locating leaks in sanitary sewers.* Tunnelling and underground space technology, 2004. 19(1): p. 85-96.

47. Danjuma, I.M., et al., *AT slot monopole antenna for UWB microwave imaging applications.* 2018.

48. Wang, J., et al., *1-D microwave imaging of human cardiac motion: An ab-initio investigation.* IEEE Transactions on Microwave Theory and Techniques, 2013. 61(5): p. 2101-2107.

49. Semenov, S.Y. and D.R. Corfield, *Microwave tomography for brain imaging: Feasibility assessment for stroke detection.* International Journal of Antennas and Propagation, 2008.

50. Zhang, H., et al. *Microwave imaging for brain tumour detection using a UWB Vivaldi Antenna array.* In *2012 Loughborough Antennas & Propagation Conference (LAPC).* 2012.

51. Danjuma, I., et al., *Design of a tapered slot low profile Vivaldi antenna for ultra-wideband microwave breast imaging applications.* Journal of Multidisciplinary Engineering Science and Technology (JMEST).

52. Li, X., et al., *An overview of ultra-wideband microwave imaging via space-time beamforming for early-stage breast-cancer detection.* IEEE Antennas and Propagation Magazine, 2005, p. 19-34.

53. Klemm, M., et al., *Microwave radar-based differential breast cancer imaging: Imaging inhomogeneous breast phantoms and low contrast scenarios.* IEEE Transactions on Antennas and Propagation, 2010, p. 2337-2344.

54. Bourqui, J., M. Okoniewski, and E.C. Fear. *Balanced Antipodal Vivaldi Antenna for Breast Cancer Detection.* in *The Second European Conference on Antennas and Propagation, EuCAP 2007.* 2007.

55. Imaging, T.-D.M.B., *Dispersive Dielectric Properties Estimation Using Patient-Specific Basis Functions DW Winters et al 2009.* IEEE Transactions on Medical Imaging, p. 969.

56. Li, D., et al., *Parallel-detection microwave spectroscopy system for breast imaging.* Review of Scientific Instruments, 200, p. 2305-2313.

57. Shea, J.D., et al., *Three-dimensional microwave imaging of realistic numerical breast phantoms via a multiple-frequency inverse scattering technique.* Medical Physics, 2010, p. 4210-4226.

58. Danjuma, I., et al., *Microwave Imaging Using Arrays of Vivaldi Antenna for Breast Cancer Applications.* International Journal, 2018.

59. Meaney, P.M., et al., *A clinical prototype for active microwave imaging of the breast.* IEEE Transactions on Microwave Theory and Techniques, 2000, p. 1841-1853.

60. Meaney, P.M., et al. *Microwave Breast Imaging with a Non-Contacting, Monopole Antenna Array.* In *2000 30th European Microwave Conference.* 2000. IEEE.

61. Henriksson, T., et al. *Clinical trials of a multistatic UWB radar for breast imaging.* In *2011 Loughborough Antennas & Propagation Conference.*

62. Li, X., et al., *Numerical and experimental investigation of an ultrawideband ridged pyramidal horn antenna with curved launching plane for pulse radiation.* IEEE Antennas and Wireless propagation letters, 2003, p. 259-262.

63. Li, X., et al., *Microwave imaging via space-time beamforming: Experimental investigation of tumour detection in multilayer breast phantoms.* IEEE Transactions on Microwave Theory and Techniques, 2004,p. 1856-1865.

64. Bourqui, J., J.M. Sill, and E.C. Fear, *A prototype system for measuring microwave frequency reflections from the breast.* Journal of Biomedical Imaging, 2012, 9.

65. Young, J. *A brief history of GPR fundamentals and applications.* In *Proc. 6th Int. Conf. Ground Penetrating Radar, 1996.*

66. Annan, A., *GPR—History, trends, and future developments.* Subsurface sensing technologies and applications, 2002. **3**(4): p. 253-270.

67. Jol, H.M. and A. Albrecht. *Searching for submerged lumber with ground-penetrating radar: Rib Lake, Wisconsin, USA.* in *Proceedings of the Tenth International Conference on Grounds Penetrating Radar, 2004.*

68. Francké, J.C. and R. Yelf. *Applications of GPR for surface mining.* In *Proceedings of the 2nd International Workshop on Advanced Ground Penetrating Radar, 2003.*

69. Benson, A.K., *Applications of ground-penetrating radar in assessing some geological hazards: examples of groundwater contamination, faults, cavities.* Journal of Applied Geophysics, 1995, p. 177-193.

70. Mellett, J.S., *Ground-penetrating radar applications in engineering, environmental management, and geology.* Journal of Applied Geophysics, 1995, p. 157-166.

71. Zeng, X. and G.A. McMechan, *GPR characterization of buried tanks and pipes.* Geophysics, 1997, p. 797-806.

72. Al-Nuaimy, W., et al., *Automatic detection of buried utilities and solid objects with GPR using neural networks and pattern recognition.* Journal of Applied Geophysics, 2000, p. 157-165.

73. Hugenschmidt, J. and R. Loser, *Detection of chlorides and moisture in concrete structures with ground-penetrating radar.* Materials and Structures, 2008, p. 785-792.

74. Maierhofer, C., *Nondestructive evaluation of concrete infrastructure with ground-penetrating radar.* Journal of Materials in Civil Engineering, 2003, p. 287-297.

75. Soliman, M. and Z. Wu, *Design, simulation and implementation of UWB antenna array and it is an application in GPR systems.*

76. Savelyev, T.G., A.G. Yarovoy, and L.P. Ligthart, *Weighted near-field focusing in an array-based GPR.* Radio Science, 2008.

77. Scott, W.R., et al., *Combined seismic, radar, and induction sensor for landmine detection.* The Journal of the Acoustical Society of America, 2008. **123**(5): p. 3042-3042.

78. Scott, W.R., et al. *Combined seismic, radar, and induction sensor for landmine detection.* In *IGARSS 2004. 2004 IEEE International Geoscience and Remote Sensing Symposium.* 2004.

79. Bourgeois, J. and G. Smith. *A complete electromagnetic simulation of ground-penetrating radar for mine detection: Theory and Experiment.* in *IEEE Antennas and Propagation Society International Symposium 1997.*

80. Kim, K. and W.R. Scott, *Design of a resistively loaded vee dipole for ultrawide-band ground-penetrating radar applications.* IEEE Transactions on Antennas and Propagation, 2005. **53**(8): p. 2525-2532.

81. Zhou, M., *Design and Time-domain Analysis of Antenna Array for UWB Imaging Application.* 2014, Queen Mary University of London.

82. Sato, M., K. Takahashi, and J. Fujiwara. *Handheld dual-sensor ALIS and its evaluation test in Cambodia.* In *2007 IEEE International Geoscience and Remote Sensing Symposium.*

83. Sato, M. and K. Takahashi. *ALIS development for humanitarian demining and its evaluation tests.* In *2008 European Radar Conference.* 2008.

84. Mahmoudzadeh, M., et al. *Water table detection by GPR in Sardon, Salamanca, Spain.* In *Proceedings of the XIII International Conference on Ground Penetrating Radar.* 2010.

85. Francés, A.P., et al., *Hydrogeophysics and remote sensing for the design of hydrogeological conceptual models in hard rocks–Sardón catchment (Spain).* Journal of applied geophysics, 2014, p. 63-81.

86. Yarovoy, A., et al. *UWB array-based radar for landmine detection.*

87. Yarovoy, A., et al. *Performance of UWB array-based radar sensor in a multi-sensor vehicle-based suit for landmine detection.* In *2008 European Radar Conference.* 2008.

88. Tivive, F.H.C., M.G. Amin, and A. Bouzerdoum. *Wall clutter mitigation based on eigen-analysis in through-the-wall radar imaging.* In *2011 17th International Conference on Digital Signal Processing (DSP).* 2011.

89. Debes, C., et al., *Target discrimination and classification in through-the-wall radar imaging.* IEEE transactions on signal processing, 2011. 59(10): p. 4664-4676.

90. Chen, P.-H., et al., *A portable real-time digital noise radar system for through-the-wall imaging.* IEEE Transactions on Geoscience and Remote Sensing, 2012. 50(10): p. 4123-4134.

91. Leigsnering, M., et al., *Compressive sensing-based multipath exploitation for stationary and moving indoor target localization.* IEEE Journal of Selected Topics in Signal Processing, 2015. 9(8): p. 1469-1483.

92. Stiefel, M., et al., *Distributed greedy signal recovery for through-the-wall radar imaging.* IEEE Geoscience and Remote Sensing Letters, 2016. 13(10): p. 1477-1481.

93. Yang, Y., et al. *Development of an ultra-wideband Vivaldi antenna array.* In *2005 IEEE Antennas and Propagation Society International Symposium.* 2005.

94. Yang, Y., C. Zhang, and A.E. Fathy, *Development and implementation of ultra-wideband see-through-wall imaging system based on a sampling oscilloscope.* IEEE Antennas and Wireless Propagation Letters, 2008. 7: p. 465-468.

95. Salman, R., et al. *On polarization diversity gain in short-range UWB-Radar object imaging.* In *2012 IEEE International Conference on Ultra-Wideband.* 2012.

96. Harker, B., A. Chadwick, and G. Harris, *Ultra-wideband 3-dimensional imaging (uwb 3d imaging).* Roke Manor Research Limited, 2008: p. 1-8.

97. Harker, B., A. Chadwick, and G. Harris, *© 2008 Roke Manor Research Limited, UK.* 2008.

98. Zhou, M., X. Chen, and C. Parini. *Development of rotating antenna array for UWB imaging application.* In *2013 Proceedings of the International Symposium on Antennas & Propagation.* 2013.

99. Danjuma, I.M., et al. *Design and optimization of a bowtie dipole adjacent to dielectric material for through the wall imaging using hybrid electromagnetic computational analysis techniques.* In *2017 Internet Technologies and Applications (ITA).* 2017.

100. Solla, M., H. Lorenzo, and V. Pérez-Gracia, *Ground Penetrating Radar: Fundamentals, Methodologies and Applications in Structures and Infrastructure.* Non-Destructive Techniques for the Evaluation of Structures and Infrastructure, 2016. 11: p. 89.

101. Venkateswarlu, B. and V.C. Tewari, *Geotechnical Applications of Ground Penetrating Radar (GPR).* Jour. Ind. Geol. Cong, 2014. 6(1): p. 35-46.

102. Daniels, D., *Ground-penetrating radar, ser.* IEEE Radar, Sonar, Navigation and Avionics Series. London: The Institution of Electrical Engineers, 2004(15).

103. Daniels, D., *Ground Penetrating Radar, 2nd edn London: Institution of Electrical Engineers.* 2004.

104. Chen, Z.N., et al., *Considerations for source pulses and antennas in UWB radio systems.* IEEE Transactions on Antennas and Propagation, 2004. 52(7): p. 1739-1748.

105. Amin, M. and K. Sarabandi, *Special issue on remote sensing of building interior.* IEEE Transactions on Geoscience and Remote Sensing, 2009. 47(5): p. 1267-1268.

106. Swanson, D.G. and W.J. Hoefer, *Microwave circuit modelling using electromagnetic field simulation.* 2003: Artech House.

107. Deshpande, M. and J. Shin. *Characterization of meta-materials using computational electromagnetic methods.* In *IEEE/ACES International Conference on Wireless Communications and Applied Computational Electromagnetics, 2005.*

108. Hand, J., *Modelling the interaction of electromagnetic fields (10 MHz–10 GHz) with the human body: methods and applications.* Physics in Medicine & Biology, 2008. 53(16): p. R243.

109. Willets, K.A. and R.P. Van Duyne, *Localized surface plasmon resonance spectroscopy and sensing.* Annu. Rev. Phys. Chem., 2007. 58: p. 267-297.

110. Lal, S., S. Link, and N.J. Halas, *Nano-optics from sensing to waveguiding.* Nature Photonics, 2007. 1(11): p. 641.

111. Yee, K.S. and J.S. Chen, *The finite-difference time-domain (FDTD) and the finite-volume time-domain (FVTD) methods in solving Maxwell's equations in* IEEE Transactions on Antennas and Propagation, 1997. 45(3): p. 354-363.

112. Tavlove, A. and S.C. Hagness, *Computational Electrodynamics: The Finite-Difference Time-Domain Method Artech House.* Norwood, MA, 1995.

113. Zheng, F., Z. Chen, and J. Zhang, *Toward the development of a three-dimensional unconditionally stable finite-difference time-domain method.* IEEE Transactions on Microwave Theory and Techniques, 2000. 48(9): p. 1550-1558.

114. Yee, K., *Numerical solution of initial boundary value problems involving Maxwell's equations in isotropic media.* IEEE Transactions on antennas and propagation, 1966. 14(3): p. 302-307.

115. Hwang, J.-N., *A compact 2-D FDFD method for modelling microstrip structures with nonuniform grids and perfectly matched layer.* IEEE transactions on microwave theory and techniques, 2005. 53(2): p. 653-659.

116. Insana, D. and C.M. Rappaport, *Using FDFD technique in two-dimensional te analysis for modeling clutter in-wall penetrating radar.* International Journal of Antennas and Propagation, 2014.

117. Hoefer, W.J., *The transmission-line matrix method--Theory and applications.* IEEE Transactions on Microwave Theory and Techniques, 1985. 33(10): p. 882-893.

118. Semlyen, A. and B. Gustavsen, *Phase-domain transmission-line modelling with the enforcement of symmetry via the propagated characteristic admittance matrix.* IEEE Transactions on Power Delivery, 2012. 27(2): p. 626-631.

119. Volakis, J.L., A. Chatterjee, and L.C. Kempel, *Finite element method electromagnetics: antennas, microwave circuits, and scattering applications.* Vol. 6. 1998: John Wiley & Sons.

120. Zienkiewicz, O.C., et al., *The finite element method.* Vol. 3. 1977: McGraw-hill London.

121. Jithesh, V. and D. Pande. *A review of computational EMI modelling techniques.* In *Electromagnetic Interference and Compatibility, 2003. INCEMIC 2003. 8th International Conference on.* 2003.

122. Newey, W.K. and K.D. West, *Hypothesis testing with an efficient method of moments estimation.* International Economic Review, 1987: p. 777-787.

123. Vipiana, F., D.R. Wilton, and W.A. Johnson, *Advanced numerical schemes for the accurate evaluation of 4-D reaction integrals in the method of moments in* IEEE Transactions on Antennas and Propagation, 2013. 61(11): p. 5559-5566.

124. Abd-Alhameed, R.A. and P.S. Excell, *Non-uniform surface current distribution on parallel wire loop antennas using curved patches in the method of moments.* 7th International Conference on Computation in Electromagnetics, CEM Brighton., 2008: p. 24-25.

125. Chung, S.W.J., R.A. Abd-Alhameed, and P.S. Excell, *Design of bow-tie wire antenna for near field imaging using genetic algorithms.* URSI Symposium, University of Portsmouth, 2-3 July 2007: p. 15.

126. Chung, S.W.J., et al., *Wideband loaded wire bow-tie antenna for near field imaging using genetic algorithms.* Progress In Electromagnetics Research Symposium (PIERS) 2008 Cambridge, USA, 2-6 July 2008.

127. S.W.J.Chung, R.A. Abd-Alhameed, and P.S. Excell, *Design of wire bow-tie antenna for near field imaging using genetic algorithms.* Proceeding of 2008 Loughborough Antenna and Propagation Conference (LAPC), 17-18 March 2008: p. 317-320.

128. See, C.H., et al., *A new design of circularly-polarized conical-beam microstrip patch antennas using genetic algorithms.* The 1st European Conference on Antennas and Propagation, Nice, France., Nov. 2006. Session 4PA1.

129. Zhou, D., R.A. Abd-Alhameed, and P.S. Excell, *Bandwidth enhancement of balanced folded loop antenna design for mobile handsets using genetic algorithms.* The Electromagnetics Academy, PIERS Online, 2008. 4: p. 136-139.

130. Zhou, D., R.A. Abd-Alhameed, and P.S. Excell, *Bandwidth enhancement of balanced folded loop antenna design for mobile handsets using genetic algorithms.* IEEE Antennas and Propagation International Symposium, June 2007: p. 3568-3568.

131. Zhou, D., R.A. Abd-Alhameed, and P.S. Excell, *Design of antenna for wide harmonic suppression using adaptive meshing and genetic algorithms.* 7th International Conference on Computation in Electromagnetics, CEM Brighton., March 2008: p. 187-188.

132. Zhou, D., et al., *Design of quadrifilar helical and spiral antennas in the presence of mobile handsets using genetic algorithms.* The 1st European Conference on Antennas and Propagation, Nice, France., Nov. 2006. Session 3PA1, no. 122.

133. Harrington, R.F., *The method of moments in electromagnetics.* Journal of Electromagnetic Waves and Applications, 1987. 1(3): p. 181-200.

134. Rokhlin, V., *Rapid solution of integral equations of scattering theory in two dimensions.* Journal of Computational Physics, 1990. 86(2): p. 414-439.

135. Chew, W.C., T.J. Cui, and J.M. Song, *A FAFFA-MLFMA algorithm for electromagnetic scattering.* IEEE Transactions on Antennas and Propagation, 2002. 50(11): p. 1641-1649.

136. Belegundu, A.D. and T.R. Chandrupatla, *Optimization concepts and applications in engineering.* 2019: Cambridge University Press.

137. Dorsey, W.M. and D.P. Scholnik. *A hybrid global-local optimization approach to phase-only array-pattern synthesis.* In *2015 IEEE Radar Conference (RadarCon).* 2015. IEEE.

138. Yan, Z., J. Fan, and J. Wang, *A collective neurodynamic approach to constrained global optimization.* IEEE transactions on neural networks and learning systems, 2016. 28(5): p. 1206-1215.

139. Liang, J.J., et al., *Comprehensive learning particle swarm optimizer for global optimization of multimodal functions.* IEEE transactions on evolutionary computation, 2006. 10(3): p. 281-295.

140. Johnson, J.M. and V. Rahmat-Samii, *Genetic algorithms in engineering electromagnetics.* IEEE Antennas and Propagation Magazine, 1997. 39(4): p. 7-21.

141. Binitha, S. and S.S. Sathya, *A survey of bio-inspired optimization algorithms.* International Journal of Soft Computing and Engineering, 2012. 2(2): p. 137-151.

142. Hussein, A.H., et al., *Optimum Design of Linear Antenna Arrays Using a Hybrid MoM/GA Algorithm.* IEEE Antennas and Wireless Propagation Letters, 2011. 10: p. 1232-1235.

143. Sijher, T.S. and A.A. Kishk, *Antenna modelling by infinitesimal dipoles using genetic algorithms.* Progress In Electromagnetics Research, 2005. 52: p. 225-254.

144. Akinsolu, M.O., et al., *Antenna design explorer: A GUI software tool for efficient antenna design optimization.* 2017.

145. Liu, B., et al., *Efficient global optimisation of microwave antennas based on a parallel surrogate model-assisted evolutionary algorithm.* IET Microwaves, Antennas & Propagation, 2018.

146. Alhaddad, A., et al., *Low profile dual-band-balanced handset antenna with the dual-arm structure for WLAN application.* IET microwaves, antennas & propagation, 2011. 5(9): p. 1045-1053.

147. Antoniades, M.A. and G.V. Eleftheriades, *A compact multi-band monopole antenna with a defected ground plane.* Antennas and Wireless Propagation Letters, IEEE, 2008. 7: p. 652-655.

148. Sadeghzadeh-Sheikhan, R., et al., *Planar monopole antenna employing back-plane ladder-shaped resonant structure for ultra-wideband performance.* Microwaves, Antennas & Propagation, IET, 2010. 4(9): p. 1327-1335.

149. Kiminami, K., A. Hirata, and T. Shiozawa, *Double-sided printed bow-tie antenna for UWB communications.* IEEE antennas and wireless propagation letters, 2004. 3(1): p. 152-153.

150. Huygens, C., *Traité de la lumiere, Van de Aa, Leyden (1690).* English translation: Treatise on light, 1960.

151. Mohammed, H., et al. *Evaluation of genetic algorithms, particle swarm optimisation, and firefly algorithms in antenna design.* In *Synthesis, Modeling, Analysis and Simulation Methods and Applications to Circuit Design (SMACD), 2016 13th International Conference.*

152. Bridges, G.E., *Transient plane wave coupling to bare and insulated cables buried in a lossy half-space.* IEEE transactions on electromagnetic compatibility, 1995. 37(1): p. 62-70.

153. Garg, R., et al., *Microstrip antenna design handbook.* 2001: Artech house.

154. Balanis, C.A., *Antenna theory: analysis and design.* 2016: John Wiley & Sons.

155. Kumar, G. and K.P. Ray, *Broadband microstrip antennas.* 2003: Artech house.

156. Wong, K.-L., *Compact and broadband microstrip antennas.* Vol. 168. 2004: John Wiley & Sons.

157. Waterhouse, R., *Microstrip patch antennas: a designer's guide.* 2013: Springer Science & Business Media.

158. Kraus, J.D., *Antennas: for all applications.* 3rd ed. 2002: McGraw- Hill.

159. Balanis, C.A., *Modern Antenna Handbook.* 2008.

160. James, J.R., *Handbook of microstrip antennas.* Vol. 1. 1989.

161. Gibson, P.J. *The Vivaldi Aerial.* In *1979 9th European Microwave Conference.* 1979.

162. Pandey, G., et al., *High gain Vivaldi antenna for radar and microwave imaging applications.* International Journal of Signal Processing Systems, 2015. 3(1): p. 35-39.

163. Natarajan, R., et al., *Modified antipodal Vivaldi antenna for ultra-wideband communications.* IET Microwaves, Antennas & Propagation, 2016. 10(4): p. 401-405.

164. He, S.H., et al., *An Improved Vivaldi Antenna for Vehicular Wireless Communication Systems.* IEEE Antennas and Wireless Propagation Letters, 2014. 13: p. 1505-1508.

165. Kumar, R. and S. Priyadarshi. *Multi-band Vivaldi antenna for wireless communication: Design, analysis and modelling of Vivaldi antenna.* In *2016 International Conference on Communication and Electronics Systems (ICCES).* 2016.

166. Behera, B.R. *Vivaldi antenna for UWB communications: Design, modelling and analysis of Vivaldi Antenna with genetic algorithm.* In *2016 International Conference on Control, Computing, Communication and Materials (ICCCCM).* 2016.

167. Mahmud, M.Z., et al., *Design and parametric investigation of directional antenna for a microwave imaging application.* IET Microwaves, Antennas & Propagation, 2017. 11(6): p. 770-778.

168. Uyanik, C., et al. *A coplanar Vivaldi antenna design with improved frequency response for microwave breast imaging.* In *2016 IEEE Conference on Antenna Measurements & Applications (CAMA).* 2016.

169. Bah, M.H., J.s. Hong, and D.A. Jarmo. *UWB antenna design and implementation for microwave medical imaging applications.* In *2015 IEEE International Conference on Communication Software and Networks (ICCSN).* 2015.

170. Fioranelli, F., et al., *Through-The-Wall Detection With Gated FMCW Signals Using Optimized Patch-Like and Vivaldi Antennas.* IEEE Transactions on Antennas and Propagation, 2015. 63(3): p. 1106-1117.

171. Sandora, J.S. and G.L. Charvat. *An ultra-wideband Vivaldi and linear hybrid taper antenna for use in a near-field real-time phased array radar system.* In *2013 IEEE International Symposium on Phased Array Systems and Technology.* 2013.

172. Zhang, J., E.C. Fear, and R.H. Johnston, *Cross-Vivaldi antenna for breast tumour detection.* Microwave and Optical Technology Letters, 2009. 51(2): p. 275-280.

173. Rai, P.K., *A Brief Review of an Ultra-Wideband Antenna Element.*

174. Wiesbeck, W., G. Adamiuk, and C. Sturm, *Basic properties and design principles of UWB antennas.* Proceedings of the IEEE, 2009. 97(2): p. 372-385.

175. Brown, T., S. Saunders, and B. Evans, *Analysis of mobile terminal diversity antennas.* IEE Proceedings-Microwaves, Antennas and Propagation, 2005. 152(1): p. 1-6.

176. Liu, B., et al., *An Efficient Method for Antenna Design Optimization Based on Evolutionary Computation and Machine Learning Techniques.* IEEE Transactions on Antennas and Propagation, 2014. 62(1): p. 7-18.

177. Gustrau, F. and D. Manteuffel, *EM Modeling of Antennas and RF Components for Wireless Communication Systems.* 2006: Springer Science & Business Media.

178. Baytöre, C., et al. *Low-cost dual-band monopole antenna design and analysis for 802.11 b/g/n/ac standards.* In *2015 23rd Signal Processing and Communications Applications Conference (SIU).* 2015.

179. Liang, J., et al., *Study of CPW-fed circular disc monopole antenna for ultra-wideband applications.* IEE Proceedings-Microwaves, Antennas and Propagation, 2005. 152(6): p. 520-526.

180. Agrawall, N.P., G. Kumar, and K. Ray, *Wide-band planar monopole antennas.* IEEE transactions on antennas and propagation, 1998. 46(2): p. 294-295.

181. Rao, S.V.P. and A. Sudhakar. *A compact OCTAGONAL printed monopole UWB antenna for biomedical applications.* In *2015 13th International Conference on Electromagnetic Interference and Compatibility (INCEMIC).* 2015. IEEE.

182. Celik, A.R. and M.B. Kurt, *Development of an ultra-wideband, stable and high-directive monopole disc antenna for radar-based microwave imaging of breast cancer.* Journal of Microwave Power and Electromagnetic Energy, 2018. 52(2): p. 75-93.

183. Liu, B., et al., *Efficient global optimisation of microwave antennas based on a parallel surrogate model-assisted evolutionary algorithm.* IET Microwaves, Antennas & Propagation, 2018. 13(2): p. 149-155.

184. Akinsolu, M.O., et al., *A parallel surrogate model assisted evolutionary algorithm for electromagnetic design optimization.* IEEE Transactions on Emerging Topics in Computational Intelligence, 2019. 3(2): p. 93-105.

185. Liu, H.-W., et al., *Compact monopole antenna with band-notched characteristic for UWB applications.* IEEE Antennas and Wireless Propagation Letters, 2010. 9: p. 397-400.

186. Abdalla, M.A., A.A. Ibrahim, and A. Boutejdar, *Resonator switching techniques for notched ultra-wideband antenna in wireless applications.* IET Microwaves, Antennas & Propagation, 2015. 9(13): p. 1468-1477.

187. Ojaroudi, M., et al., *Small square monopole antenna for UWB applications with variable frequency band-notch function.* IEEE Antennas and Wireless Propagation Letters, 2009. **8**: p. 1061-1064.

188. Tasouji, N., et al., *A novel printed UWB slot antenna with reconfigurable band-notch characteristics.* IEEE Antennas and wireless propagation letters, 2013. 12: p. 922-925.

189. Valizade, A., et al., *A novel design of reconfigurable slot antenna with switchable band notch and multi resonance functions for UWB applications.* IEEE Antennas and Wireless Propagation Letters, 2012. 11: p. 1166-1169.

190. Khaled, E.E.M., A.A.R. Saad, and D.A. Salem, *A proximity-FED annular slot antenna with different a band-notch manipulations for ultra-wideband applications.* Progress In Electromagnetics Research, 2012. 37: p. 289-306.

191. Haraz, O. and A.-R. Sebak, *UWB antennas for wireless applications*, in *Advancement in Microstrip Antennas.* 2013, InTech. p. 125-152.

192. STudio, C.M., *CST Studio Suite 2011.* Computer Simulation Technology AG, 2013.

193. Liu, B., et al., *An efficient method for antenna design optimization based on evolutionary computation and machine learning techniques.* IEEE transactions on antennas and propagation, 2013. 62(1): p. 7-18.

194. Liu, B., S. Koziel, and N. Ali, *SADEA-II: A generalized method for efficient global optimization of antenna design.* Journal of Computational Design and Engineering, 2017. 4(2): p. 86-97.

195. Liu, B., Q. Zhang, and G.G. Gielen, *A Gaussian process surrogate model assisted evolutionary algorithm for medium scale expensive optimization problems.* IEEE Transactions on Evolutionary Computation, 2013. 18(2): p. 180-192.

196. Grout, V., et al., *Software Solutions for Antenna Design Exploration: A Comparison of Packages, Tools, Techniques, and Algorithms for Various Design Challenges.* IEEE Antennas and Propagation Magazine, 2019. 61(3): p. 48-59.

197. Peyman, A., S. Holden, and C. Gabriel, *Dielectric Properties of Biological Tissues at Microwave Frequencies*, in *Final Technical Report*. 2005, MTHR Department of Health UK.

198. Lin, C.-H., et al., *A compact planar inverted-F antenna for 2.45 GHz on-body communications.* IEEE Transactions on Antennas and Propagation, 2012. 60(9): p. 4422-4426.

199. Abd-Alhameed, R.A., P.S. Excell, and M.A. Mangoud, *Computation of specific absorption rate in the human body due to base-station antennas using a hybrid formulation.* IEEE Transactions on Electromagnetic Compatibility, 2005. 47(2): p. 374-381.

200. Chen, Y., P. Kosmas, and S. Martel, *A feasibility study for microwave breast cancer detection using contrast-agent-loaded bacterial microbots.* International Journal of Antennas and Propagation, 2013. 2013.

201. AlShehri, S.A., et al., *Experimental breast tumour detection using NN-based UWB imaging.* Progress In Electromagnetics Research, 2011. **111**: p. 447-465.

202. Bialkowski, M.E., et al. *Novel image reconstruction algorithm for a UWB cylindrical microwave imaging system*. In *2010 IEEE MTT-S International Microwave Symposium*. 2010. IEEE.

203. Elsdon, M., et al. *Experimental investigation of breast tumour imaging using indirect microwave holography.* Microwave and optical technology letters, 2006. 48(3): p. 480-482.

204. Bialkowski, M.E. *Ultra-wideband microwave system with novel image reconstruction strategies for breast cancer detection*. The 40th European Microwave Conference. 2010. IEEE.

205. Fear, E.C. and M.A. Stuchly. *Microwave breast cancer detection*. In *2000 IEEE MTT-S International Microwave Symposium Digest (Cat. No.00CH37017)*. 2000.

206. Parkin, D.M., et al., *Estimating the world cancer burden: Globocan 2000.* International journal of cancer, 2001. 94(2): p. 153-156.

207. Slamon, D.J., et al., *Use of chemotherapy plus a monoclonal antibody against HER2 for metastatic breast cancer that overexpresses HER2.* New England Journal of Medicine, 2001. 344(11): p. 783-792.

208. Ahsan, S., et al. *Balanced antipodal Vivaldi antenna for microwave tomography*. In *2014 4th International Conference on Wireless Mobile Communication and Healthcare-Transforming Healthcare Through Innovations in Mobile and Wireless Technologies (MOBIHEALTH)*. 2014. IEEE.

209. Fei, P., et al., *A miniaturized antipodal Vivaldi antenna with improved radiation characteristics.* IEEE antennas and wireless propagation letters, 2011. 10: p. 127-130.

210. Bang, J., J. Lee, and J. Choi, *Design of a wideband antipodal Vivaldi antenna with an asymmetric parasitic patch.* Journal of Electromagnetic Engineering and Science, 2018. 18(1): p. 29-34.

211. Wu, B., Y. Ji and G. Fang. *Design and measurement of compact tapered slot antenna for UWB microwave imaging radar*. In *2009 9th International Conference on Electronic Measurement & Instruments*. 2009. IEEE.

Author's Publication Record

JOURNAL PAPERS

1. **I. M. Danjuma**, B. A. Mohammed, N.N Eya, G.A Oguntala, H.A. Obeidat. Raed. Abd-Alhameed, J.M.Noras, "Microwave Imaging Using Arrays of Vivaldi Antenna for Breast Cancer Imaging Applications," in International Journal of Microwaves Applications, vol. 7, issue 5, 2018, pp. 32-37.

2. **I.M.Danjuma**, Mobayode O Akinsolu, Chan See, Raed Abd Alhameed, and Bo Li, "Design and Optimisation of a Slotted Monopole Antenna for Ultra-Wideband Body Centric Imaging Applications", in IEEE Journal of EM, RF and Microwaves in Medicine and Biology,vol.4.No 2. June 2020, pp.140-147.

3. **I.M.Danjuma**, Fathi Abdussalam, Buhari Muhammad, Eya Eya, Raed Abd Alhameed, James M. Noras, "Design of a Taper Slot Low Profile Vivaldi Antenna for Ultra-Wideband Microwave Breast Imaging Applications", Journal of Multidisciplinary Engineering Science and Technology, vol. 4, issue 8, 2017, pp. 7972-7976.

4. A.F.Mirza, C See, **I. M. Danjuma**, Raed Abd Alhameed, "An Active Microwave Sensor for Near-Field Imaging," in IEEE Sensors Journal Vol. 17, Issue, 9, 2017, pp.2749-2757.

5. B. A. Mohammed, **I. M. Danjuma**, R. A. Abd-Alhameed, N. A. Abduljabbar, A. S. Hussaini, and I. T. E. Elfergani, "A Dynamic Imbalanced Load Modulation Approach To Design and Implement an Energy-Efficient RF Power Amplifier," in International Journal of Engineering and Science (IJES), vol. 7, issue 4, 2018, pp. 53-58.

6. B. A. Mohammed, **I. M. Danjuma**, R. A. Abd-Alhameed, A. S. Hussaini, I.T. E. Elfergani and J. Rodriguez, "Design and Simulation of Balanced RF Power Amplifier over Adaptive Digital Pre-distortion for MISO WLAN-OFDM Applications," in Journal of Multidisciplinary Engineering Science and Technology (JMEST)*, vol. 4, issue 9, 2017, pp. 8217-8221.

7. B. A. Mohammed, A. S. Hussaini, **I. M. Danjuma**, Y. I. Abdulraheem, R. A. Abd-Alhameed, G. Oguntala, N. N. Eya and F. El-Negri, "Distortion level approximation of Linear and Nonlinear RF Power Amplifier over OFDM System," in International Journal of Engineering and Science (IJES)*, vol. 7, issue 11, 2018, pp. 58-69.

8. B. A. Mohammed, A. S. Hussaini, R. A. Abd-Alhameed, **I. M. Danjuma**, A. S. Asharaa, I. T. E. Elfergani and J. Rodriguez, "Towards A 15.5W Si- LDMOS Energy Efficient Balanced RF Power Amplifier for 5G-LTE Multi-carrier Applications," in EAI Endorsed Transactions on Creative Technologies (EAI-EU)*, vol. 5, issue 15, 2018.

9. G. A. Oguntala**, I. M. Danjuma**, Gbeminiyi Sobamowo, Raed Abd-Alhameed and Jim Noras, " Nonlinear thermal analysis of a convective-radiative longitudinal porous fin of functionally graded material for efficient cooling of consumer electronics " in International Journal of Ambient Energy(IJAE), vol. 5, issue 7, 2019, pp. 1-15.

INTERNATIONAL CONFERENCES

1. **I.M.Danjuma**, F.M. Abdussalam. Eya, M.O Akinsolu, R.A. Abd-Alhameed, J.M. Noras "Design and Optimisation of a bowtie dipole adjacent to dielectric material for through the wall imaging using hybrid electromagnetic computational analysis techniques" in IEEE, International Conference on Internet Technologies & Applications (ITA), Wrexham,2017, pp.254-258.

2. **I. M. Danjuma**, M.O. Akinsolu, G. Oguntala, Abdalfettah Ashraaf, Raed Abd Alhameed., " A T Slot Monopole antenna for UWB microwave imaging applications, "IEEE International Conference on Antenna and Propagation, Loughborough, 2018, pp. 1-5.

3. **I.M.Danjuma**, M.O Akinsolu, B. Muhammad, E. Eya, R.A Abd-Alhameed, J.M. Noras, "A Compact size and low profile rectangular slot monopole antenna for UWB Body centric applications," IEEE International Conference on Antenna and Propagation and USNC-URSI Radio Science Meeting, Georgia, USA,7-12 July 2019, pp.91-92.

4. **I.M. Danjuma** et al. '' Design and Optimisation of a Compact Rectangular Monopole Antenna for UWB Human Body Wireless Application.'' URSI Festival of Radio Science, UK Panel, International Conference, Teddington, Middlesex, London, 2019.

5. **I.M.Danjuma** et al., "Compact UWB Antenna Array for Breast Cancer Imaging Applications Using Optimisation Algorithm," International Multi-Disciplinary Conference, Iraq, 28-30 June 2020, (Accepted).

6. **I. M. Danjuma,** F. M. Abdussalam, Ammar Ali, Abd-Alhameed, "Advanced Image Reconstruction Algorithm for Breast Cancer Detection," URSI Festival of Radio Science, UK Panel, Internationale Conference, Bradford, West Yorkshire, 2017.

7. **I.M.Danjuma,** F.M. Abdussalam, Ammar Ali, Abd-Alhameed, "Reconfigurable Design Model of Bow-tie Dipole Adjacent to Lossy Dielectric Material Using Optimisation Method in Hybrid Electromagnetic Techniques," URSI Festival of Radio Science, UK Panel, International Conference, York,2016.

8. **I. M. Danjuma**, B.A. Mohammed and Raed Abd-Alhameed, "Implantable Antenna for in-body ultrawideband imaging applications URSI Festival of Radio Science, UK Panel, Internationale Conference, Manchester, 2019.

9. M.A.G. Al-Sadoon, **I.M.Danjuma,** F.M. Abdussalam, I.T.E.Elfergani, J. Rodriguez RA Abd-Alhameed, S.M.R.Jones, "Dual-band compact size antenna array for the angle of arrival estimation," IEEE International Conference on Antenna and Propagation, Loughborough, 2017, pp.1-5

10. B.A.Mohammed, R. A. Abd-Alhameed, N.A.Abduljabbar, **I.M.Danjuma**, T.E.Elfergani, A.S Hussain, Rodriguez, " A CAD-Oriented technique to design an optimum load impedance with the multi-coupler network for the class-F power amplifier," IEEE International Conference on Antenna and Propagation, Loughborough,2017.

11. M.O Akinsolu, **I.M.Danjuma**, R. A. Abd-Alhameed, et al., "Efficient AI-Driven Design of Microwave Antennas Using PSADEA," IEEE 2nd the Middle East and North Africa Communications Conference, Kingdom of Bahrain, 2019, pp. 1-5.

Author's Awards

1. Best paper award in "URSI Festival of Radio Science, UK Panel, Internationale Conference, held in the University of Manchester, Oxford Road, Manchester,2019, '' Implantable Antenna for in-body Ultra wideband Imaging Applications''.

2. Best paper award in "URSI Festival of Radio Science, UK Panel, International Conference, held in the University of Bradford, Bradford, West Yorkshire,2018, '' Advanced Image Reconstruction Algorithm for Breast Cancer Detection''.

3. Second overall paper award in the First Annual Innovative Engineering Research Conference, conducted at the University of Bradford, Bradford, West Yorkshire,2017, '' Design of a Taper Slot Low Profile Vivaldi Antenna for Ultra-Wideband Microwave Breast Imaging Applications''.
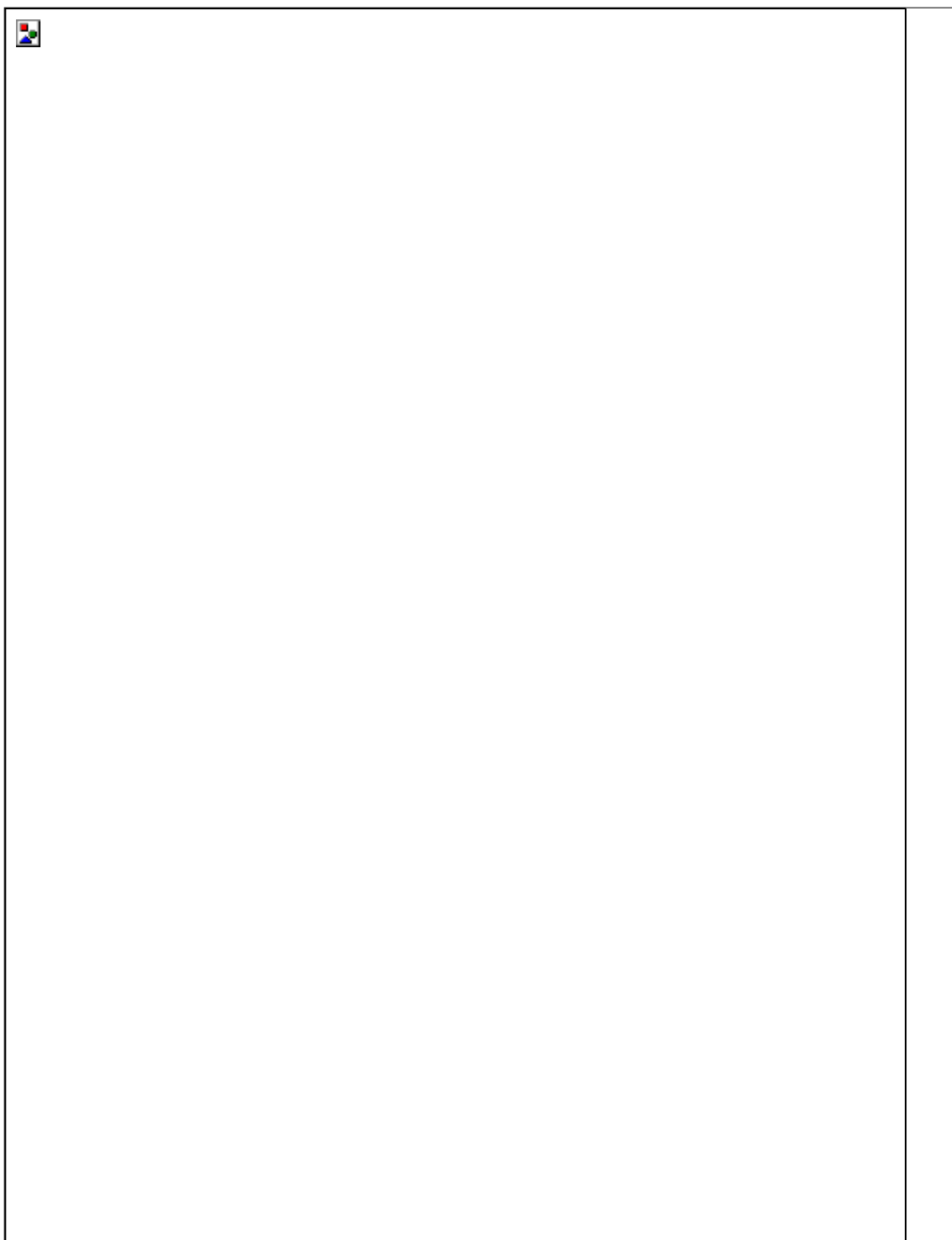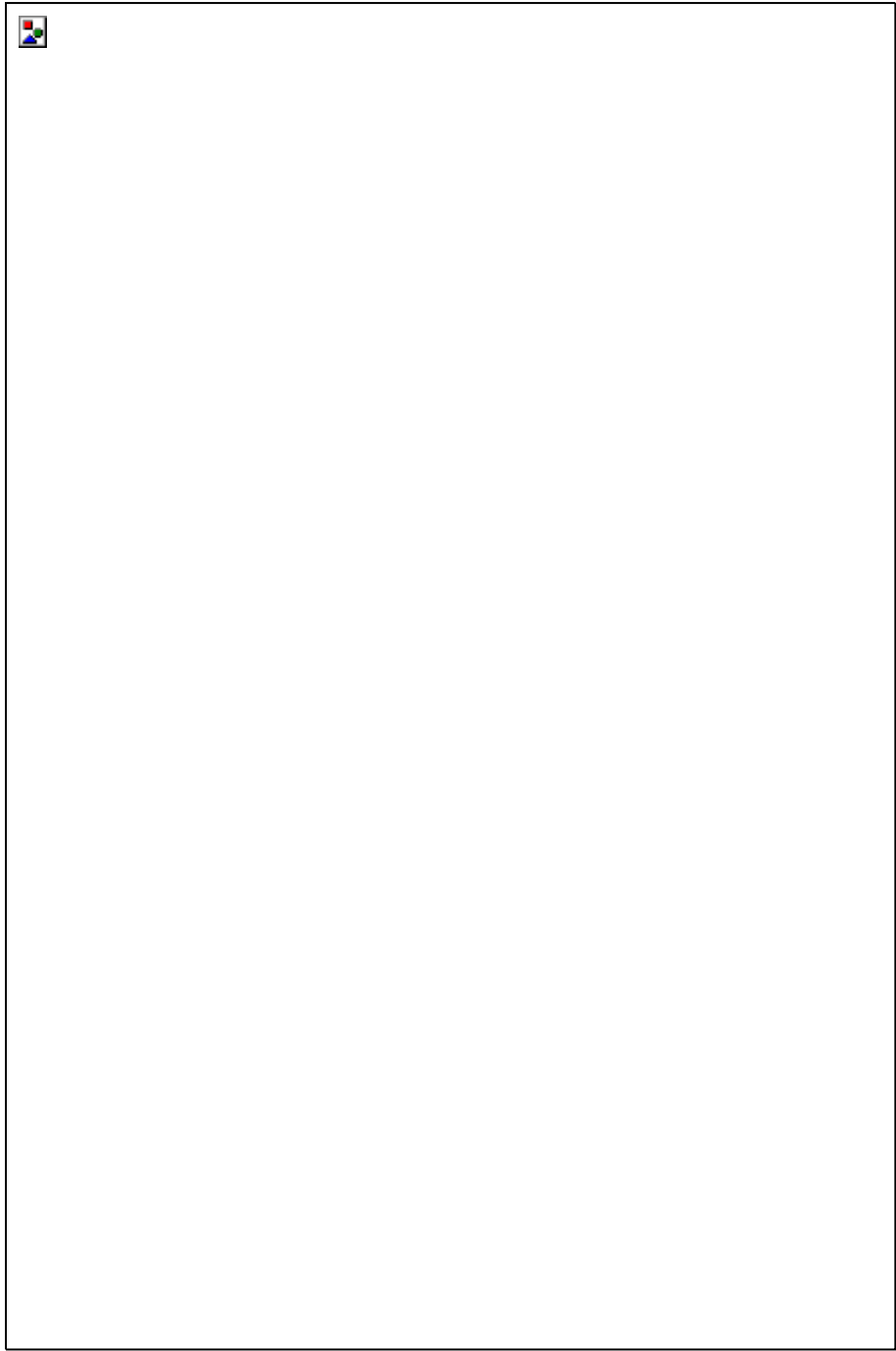
Authors Selected Publications
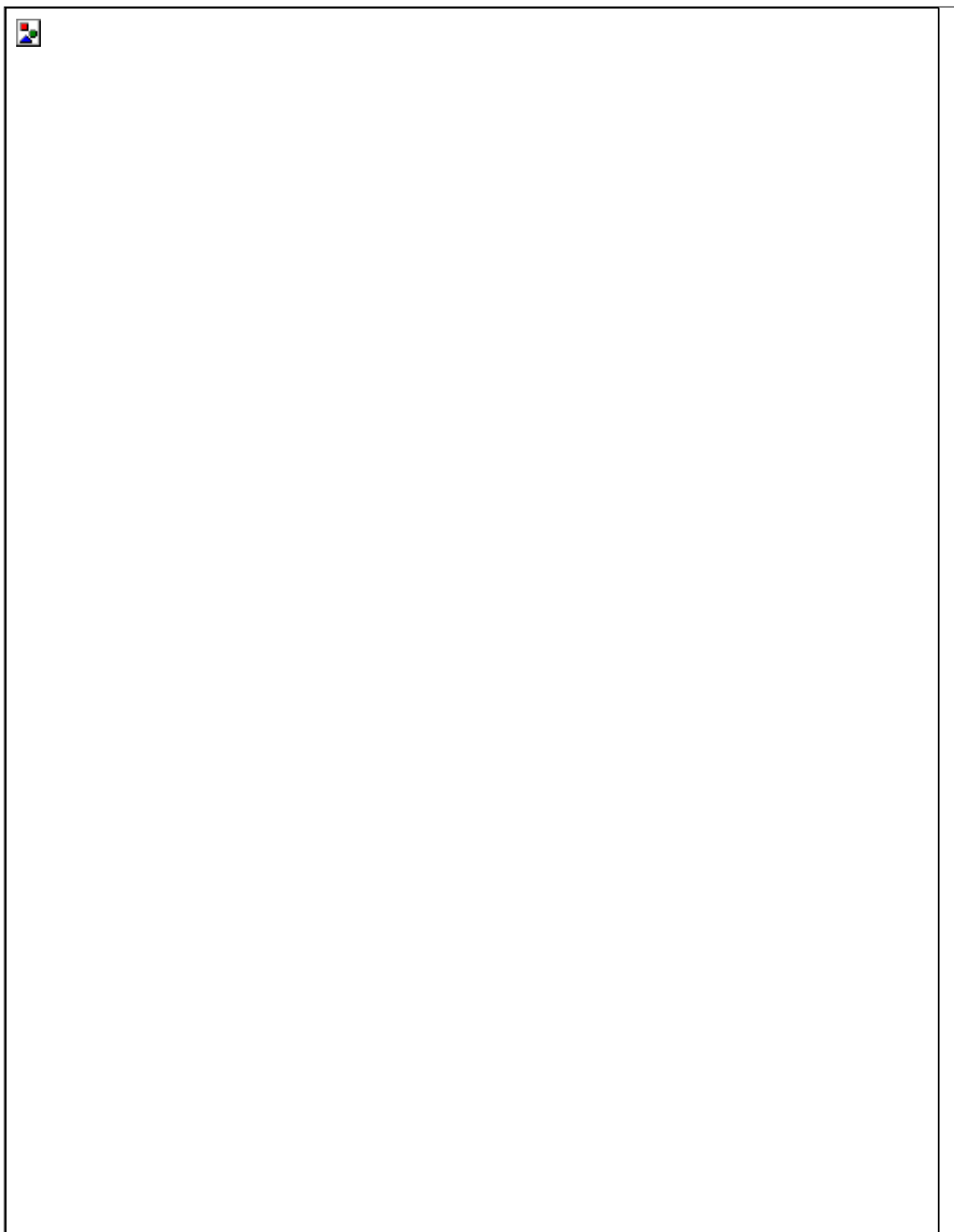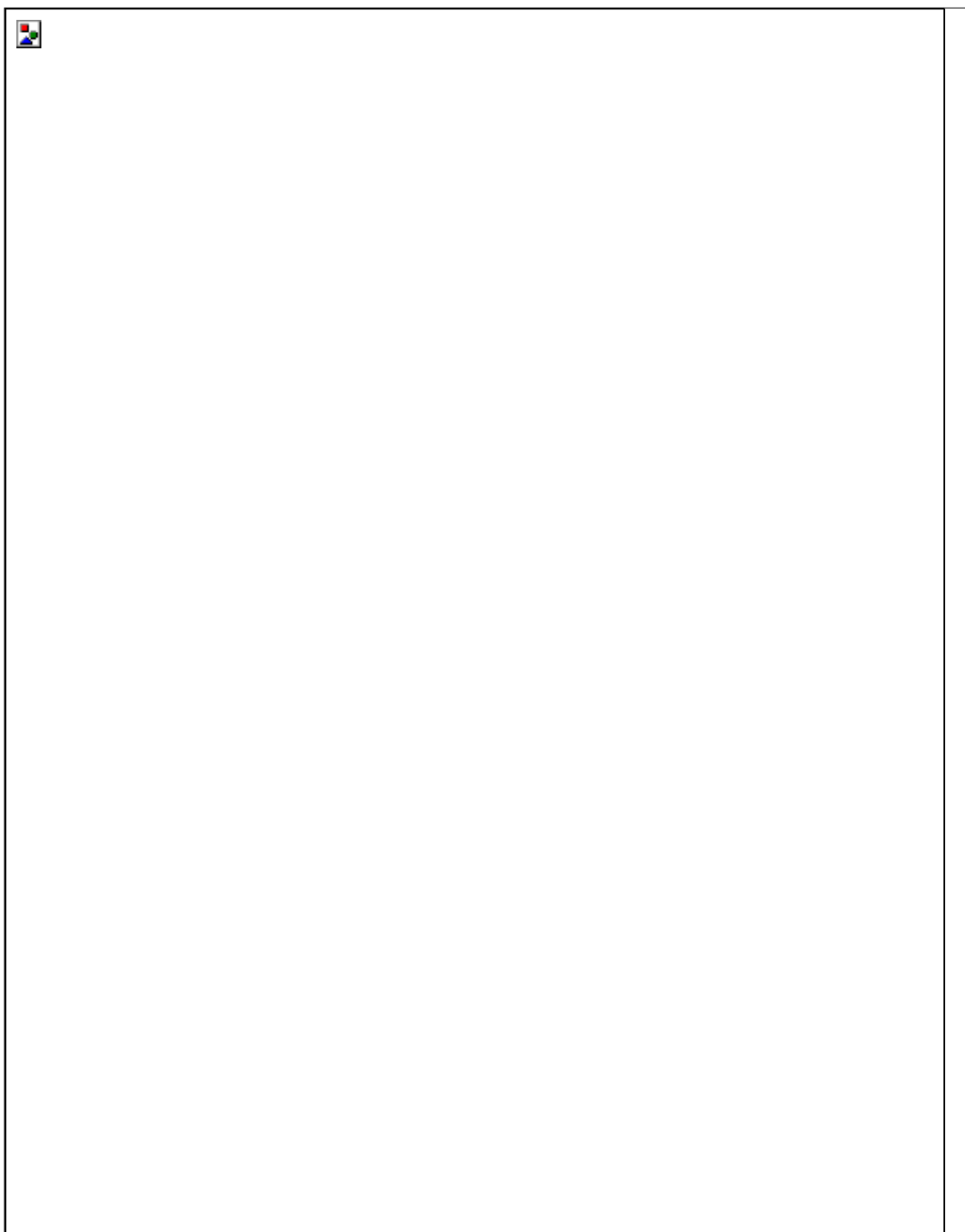
Step 5: Use the newest solution from the data base and their corresponding function values to build the GP model.

Step 6: Prescreen the λ child result generated in step 4 by using the GP model in step 5 with the LCB prescreening.

Step 7: Finally evaluate the prescreened best child result from step 6, add this evaluated solution and its corresponding functions value to the data base. Proceeds to step 2.

III ANTENNA ANALYSIS

Figures 2 and 3 shows the basic and the design parametrized geometry of the isosceles triangle Bowtie antenna with total length of $0.2385\,\lambda$ and width of $0.1073\,\lambda$. The dielectric has lengths of 1.66λ, width of $1.25\,\lambda$ and thickness of $0.833\,\lambda$ all wavelength measured as a function of the center frequency with ε_r of 5, $\sigma = 0.1$ which corresponds to the electrical properties of a typical concrete inserted into the hybrid domain of the total far field region. The separation gap between the antenna and the dielectric were varied at 10mm, 20mm and 30mm respectively. Figure 4 is the hybrid MoM/FDTD model used for the research. Figure 5 depicts the parametrized return loss at the input port for different value of k ranging from 0mm-14mm. The reflection coefficient for various lengths of the antenna arm was shown for case 1- 3. It can be seen that a bandwidth of around 300 MHz could be obtained for the few arm lengths before the optimization.

The optimization was carried out using SADEA algorithm [14]. Figure 6 shows the improved bandwidth of 618MHz.The details were shown in Table 1. Using the Huygens principle which states that each point on a wave acts as secondary source of the outgoing waves[22], the Huygens surface encloses the dielectric material was modelled using number of cubical cell of 58x42x74 (a cell size equivalent to $0.025\,\lambda$). The flare angle were set at $30^0, 45^0$ and 60^0 respectively which are used to optimize the bow tie arm length for the 3 gaps chosen away from the dielectric.
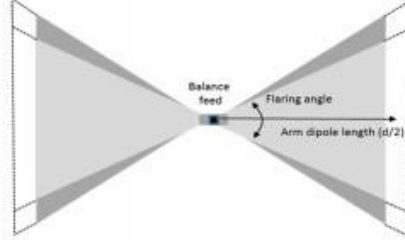

Figure 2: Basic geometry of the Bowtie antenna.

The motive is to achieve matching over a wide band width of the center frequency range (1-4) GHz. Therefore the best function for the SADEA algorithm was covered by few frequencies components which will satisfy the best matching over the desired bandwidth of 3.25 GHz. The optimum value is at the convergence rate of 450 as shown in Figure 8.
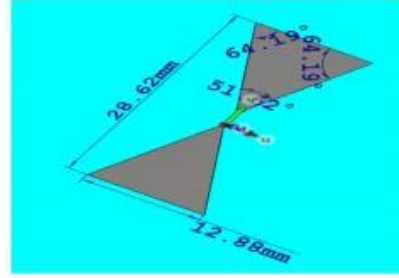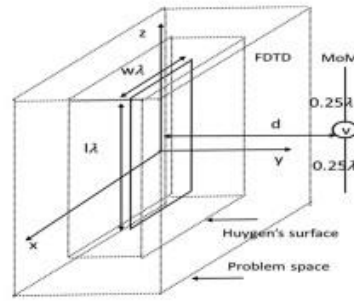

Figure 3: The design Bowtie antenna geometry

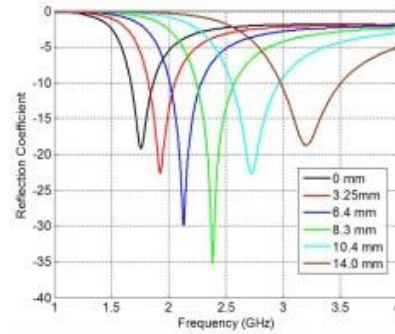Figure 4: Hybrid FDTD/MoM of the model

Figure 5: Return loss after parametrization at the input port for different value of K from the antenna edge.